MICROSTRUCTURAL VISCOPLASTIC CONTINUUM MODEL FOR ASPHALT CONCRETE

A Dissertation

by

LAITH TASHMAN

Submitted to the Office of Graduate Studies of
Texas A&M University
in partial fulfillment of the requirements for the degree of

DOCTOR OF PHILOSOPHY

December 2003

Major Subject: Civil Engineering

MICROSTRUCTURAL VISCOPLASTIC CONTINUUM MODEL FOR ASPHALT CONCRETE

A Dissertation

by

LAITH TASHMAN

Submitted to Texas A&M University
in partial fulfillment of the requirements
for the degree of

DOCTOR OF PHILOSOPHY

Approved as to style and content by:

Eyad Masad (Chair of Committee)	Dallas Little (Member)
Robert Lytton (Member)	Amy Epps Martin (Member)
Charles Glover (Member)	Paul Roschke (Head of Department)

December 2003

Major Subject: Civil Engineering

ABSTRACT

Microstructural Viscoplastic Continuum Model for Asphalt Concrete. (December 2003)

Laith Tashman, B.S., University of Jordan;

M.S., Washington State University

Chair of Advisory Committee: Dr. Eyad Masad

This dissertation presents the development of an anisotropic viscoplastic continuum damage model to describe the permanent deformation of asphalt pavements. The model is developed to account for several phenomena that influence the permanent deformation of Asphalt Concrete (AC) at high temperatures. These phenomena include strain rate dependency, confining pressure dependency, dilation, aggregate friction, anisotropy, and damage. The model is based on Perzyna's theory of viscoplasticity with Drucker-Prager yield function modified to account for the microstructure anisotropy and damage.

A parametric study was conducted to study the effect of key factors such as inherent anisotropy and damage on the model response. A preliminary investigation was conducted to demonstrate the capabilities of the model and its sensitivity to changes in the microstructure distribution and loading conditions. The model was used to describe laboratory experimental measurements obtained from the Federal Highway Administration (FHWA) Accelerated Loading Facility (ALF). The model had a good match with these experimental measurements. In particular, using the damage parameter, the model was able to capture the point at which AC experienced tertiary creep in a static creep test.

A comprehensive experiment was conducted to systematically determine the model parameters and the evolution laws that describe AC hardening, anisotropy, and damage. The experiment consisted of a set of compressive triaxial strength tests conducted at three confining pressures and five strain rates. Based on these experimental measurements, the model was modified to include a nonassociated flow rule. The model was shown to capture the experimental measurements very well.

Furthermore, an experiment was conducted to capture and characterize damage evolution in AC due to permanent deformation. AC specimens were loaded using a triaxial compression setup to four predefined strain levels at three confining pressures. X-Ray computed tomography and image analysis techniques were used to capture and characterize the evolution of cracks and air voids in the deformed specimens. Damage was found to be a localized phenomenon in the sense that there exists a critical section in an AC specimen that is mainly responsible for failure. The results of the damage experiment supported the damage evolution function proposed in the viscoplastic model.

DEDICATION

This dissertation is dedicated to my family for providing me with the necessary help and support that I needed to finish this work.

ACKNOWLEDGMENTS

I would like to take this opportunity to thank Dr. Masad for being a responsible advisor, a mentor, and most important of all, a friend. Dr. Masad has always provided me with the guidance, knowledge, encouragement, and support that I needed throughout my graduate studies. His advise has been extremely valuable, and I learned so much from him. I consider myself fortunate to have had him as my advisor.

I also would like to thank the Federal Highway Administration and the International Center for Aggregates Research for funding this project.

Special thanks are due to Dr. Dallas Little, Dr. Robert Lytton, Dr. Amy Epps Martin, and Dr. Charles Glover for serving as committee members and for their valuable input to this work.

Special thanks to Lois Peters from the Department of Civil Engineering at Texas A&M University and Cathy Bryan from the Texas Transportation Institute for their tireless help. Special thanks are also due to the staff of the Department of Civil and Environmental Engineering at Washington State University.

TABLE OF CONTENTS

CHAPTER Page

CHAPTER Page

LIST OF FIGURES

FIGURE Page

FIGURE Page

LIST OF TABLES

CHAPTER I

INTRODUCTION

PROBLEM STATEMENT

Asphalt Concrete (AC) is considered one of the most complicated materials engineers have ever dealt with. Its complexity stems from the fact that it is a composite material that possesses a wide spectrum of characteristics engineered by its individual constituents. These characteristics include rate dependency, pressure dependency, temperature dependency, dilation under shear loading, damage in terms of cracking, and anisotropy due to the microstructure distribution.

It becomes inevitable that constitutive modeling of AC is quite a challenge as one has to account for all the aforementioned characteristics. Moreover, the implementation of constitutive models in pavement engineering has been hampered until recently by the limitations of computational capabilities. Now that the computational capabilities and computer technology along with testing equipment have tremendously improved, doors are opened for a new era of accurate modeling of AC.

Kim et al. (1997) stated that the development of a valid and fundamental constitutive model serves two important purposes. First, it provides accurate information on the performance of the AC under realistic conditions, leading to better prediction of the life span of a newly constructed pavement or the remaining life of an existing one.

This dissertation follows the style and format of the *Journal of Engineering Mechanics* (ASCE).

Second, a valid constitutive model provides the link between material properties and model parameters, which can be used for better selection of the materials to improve performance.

There are three major distresses in AC pavements, namely, rutting, fatigue cracking, and low temperature cracking. The rutting phenomenon is probably considered the most important distress that contributes to the failure of a pavement. It is caused by the permanent deformation that develops gradually in the longitudinal direction under the wheel paths due to high traffic loads associated with high field temperatures. This permanent deformation is a combination of densification and shear deformation, the latter being the primary rutting mechanism (Highway Research Board 1962, Hosfra and Klomp 1972, Eisenmann and Hilmer 1987).

Researchers have adopted two main approaches in modeling permanent deformation of AC: the continuum modeling approach and the micro-mechanistic modeling approach. Continuum models are powerful as they lend themselves to Finite Element (FE) implementation to predict AC performance under boundary conditions that simulate the field conditions. However, they generally do not account for the effect of the microstructure on the macroscopic behavior of the material. In contrast, micro-mechanistic models directly account for the microstructure in modeling complex geometry as in AC. This approach, however, has been limited by the accuracy to model the actual geometry of the microstructure in FE or discrete element models. In addition, micro-mechanistic models are computationally intensive and limited in their applicability to be used as performance prediction models. Another approach that has been used in modeling geomaterials is to

include parameters that account for the material microstructure in a continuum model (e.g. Oda and Nakayama 1989). This approach has the advantages of a continuum model and at the same time it accounts for the effect of the microstructure.

Damage and anisotropy are important microstructural factors that influence the macroscopic behavior of granular materials (e.g. Oda and Nakayama 1989, Scarpas et al. 1997a). Recent studies on aggregate distribution in AC have shown that aggregate orientation in AC exhibit transverse anisotropy with respect to the horizontal direction (e.g. Tashman et al. 2001). Unlike their isotropic counterparts, anisotropic materials exhibit directionally dependent mechanical properties and thus the isotropic theories are inapplicable for them (Arramon et al. 2000). Defects in the form of cracks and air voids exist initially in most engineering materials, particularly in granular materials. These concentric discontinuities grow and propagate as the material is subjected to loading. The growth and interlinkage of these cracks and air voids within the microstructure control the deformation up to failure in many materials (e.g. Khaleel et al. 2001). The term "voids" will be used throughout this dissertation to refer to air voids and cracks combined.

However, most of the available continuum models for AC permanent deformation are developed based on the macroscopic response of AC, assume isotropic material properties, and do not account for all the mechanisms that are in play at the microscopic level. Although there is overwhelming evidence in the literature on the significant influence of damage and its evolution on AC permanent deformation (Lytton 2000), most of the available continuum models for AC do not include parameters based

on direct experimental measurements of damage. Damage has been generally assumed to be any deviation from the theory of elasticity or viscoelasticity. This situation limits the applicability of continuum damage mechanics (CDM) in solving boundary value problems in pavement engineering.

There is a profound need to develop a microstructure-based continuum model for AC permanent deformation that can account for the effect of the microstructure in terms of the anisotropy of aggregate distribution and damage in terms of voids. By doing so, the model will have the advantages of a continuum model and simultaneously accounts for the effect of the microstructure distribution. There is also a disparate need to experimentally characterize the evolution of damage in order to comprehend the actual damage mechanism. It is the remarkable improvement in computer and imaging technology that has made this possible now. X-Ray Computed Tomography (CT) and Image Analysis Techniques (IAT) are fast becoming the sate-of-the-art in accurately and nondestructively characterizing the microstructure of many engineering materials. This new imaging technology is becoming a turning point in the era of material microstructure characterization.

OBJECTIVE

The overall objective of this study is to develop a fundamental microstructure-based viscoplastic continuum model for AC that links the microstructural properties in terms of anisotropy and damage to the permanent deformation of the material. The model is still considered a continuum model and, thus, has all the advantages in terms of

numerical implementation to solve boundary value problems. At the same time it includes the effect of the microstructure in terms of the anisotropy and damage. The objective is achieved through the following phases:

Phase I

- *Task I-1*: Conduct a subjective study on the mechanism of permanent deformation in AC. This is necessary to lay out the fundamentals underlying the development of a constitutive model.
- *Task I-2*: Based on task (I-1), develop a continuum model for AC that accounts for the different phenomena influencing permanent deformation of AC. These phenomena include the aggregate friction, aggregate dilation, confining pressure dependency, strain rate dependency, anisotropy, and damage.
- *Task I-3*: Conduct a parametric study of the developed model to investigate the effect of key internal parameters on the permanent deformation of AC.
- *Task I-4*: Conduct a preliminary evaluation of the model capabilities and sensitivity to changes in the loading conditions by analyzing available experimental data.

Phase II

- *Task II-1*: Based on the preliminary results in task (I-4), design and conduct a complete set of experimental tests to determine the model parameters and their relationships to material properties using systematic experimental and analytical

procedures.

- *Task II-2*: Refine the model based on the experimental data generated in task (II-1).

Phase III

- *Task III-1*: Conduct an experiment to capture and characterize the evolution of damage in AC due to permanent deformation using X-Ray CT and IAT.
- *Task III-2*: Based on the results from task (III-1), verify the validity of the assumptions made in the model developed in task (II-1).

OUTLINE OF THE DISSERTATION

This dissertation is written according to Texas A&M University Thesis Manual standards for combining several papers into a dissertation. The dissertation follows the style and format of the *Journal of Engineering Mechanics* (ASCE). The dissertation consists of six chapters organized as follows:

Chapter I is an introduction. The problem statement is presented followed by the objective and the outline of the dissertation.

Chapter II presents a literature review pertinent to constitutive modeling of AC, anisotropy, and damage characterization of engineering materials using imaging technology.

The research activities conducted in Phase I are documented in Chapter III. The model development is discussed in detail. The capabilities of the model are illustrated by

examining the influence of different loading conditions and microstructure distribution on the model response. In addition, the model is preliminarily evaluated by comparing its predictions to the laboratory experimental data from the Accelerated Loading Facility (ALF) of the Federal Highway Administration (FHWA). Chapter III was submitted for publication as a journal paper in the *Journal of Engineering Mechanics* (ASCE). The authors of this paper are: Laith Tashman, Eyad Masad, Hussein Zbib, Dallas Little, and Kamil Kaloush.

Phase II of the objective is discussed in Chapter IV. Triaxial compressive strength tests are conducted at five strain rates and three confining pressures. The model is further refined based on the data from the experimental measurements. A systematic procedure is developed in this chapter to determine the model parameters. Chapter IV was submitted for presentation at the *Transportation Research Board* 2004 annual meeting, National Research Council. The authors of this paper are: Laith Tashman, Eyad Masad, Dallas Little, and Hussein Zbib.

Phase III of the objective is accomplished in Chapter V. X-Ray CT and IAT are utilized to capture and characterize the evolution of damage in AC microstructure at different stages of permanent deformation. In addition, implications of the damage measurements on modeling AC permanent deformation are also discussed in this chapter. Chapter V was submitted as a paper for publication and presentation through the *Association of Asphalt Paving Technologists* 2004 annual meeting. The authors of this paper are: Laith Tashman, Eyad Masad, Dallas Little, and Robert Lytton.

Chapter VI presents an overall summary of the dissertation. Future

implementations of the developed model and recommendations for further studies are also presented in this chapter.

CHAPTER II

LITERATURE REVIEW

STRAIN DECOMPOSITION FOR ELASTO-VISCO-PLASTIC MATERIALS

The experimental observations made by Perl et al. (1983) and Sides et al. (1985), and later by other researchers, suggest that the total strain for an elasto-visco-plastic material has recoverable and irrecoverable elements, some of which are time-dependent and some are time-independent. The total strain is separated into four components as shown in Fig. 2.1 for the first cycle of a creep test as follows:

$$\varepsilon = \varepsilon^{e} + \varepsilon^{ve} + \varepsilon^{p} + \varepsilon^{vp} \tag{2-1}$$

where ε is the total strain; ε^{e} is the elastic strain, which is recoverable and time-independent; ε^{ve} is the viscoelastic strain, which is recoverable and time-dependent; ε^{p} is the plastic strain, which is irrecoverable and time-independent; and ε^{vp} is the viscoplastic strain, which is irrecoverable and time-dependent. The instantaneous response is time independent and includes both elastic and plastic component. The time dependent response includes the viscoelastic and viscoplastic component. Upon removal of the load, the instantaneous response includes only the elastic response and the time dependent response after unloading is due to viscoelasticity only. After a very long time, the response of the material tends to be asymptotic to the sum of the plastic and viscoplastic, which are irrecoverable components (Lytton et al. 1993). It is noteworthy that Fig. 2.1 and Eq. (2-1) form the basis of modeling the response of Asphalt Concrete (AC) in most of the studies available in the literature.

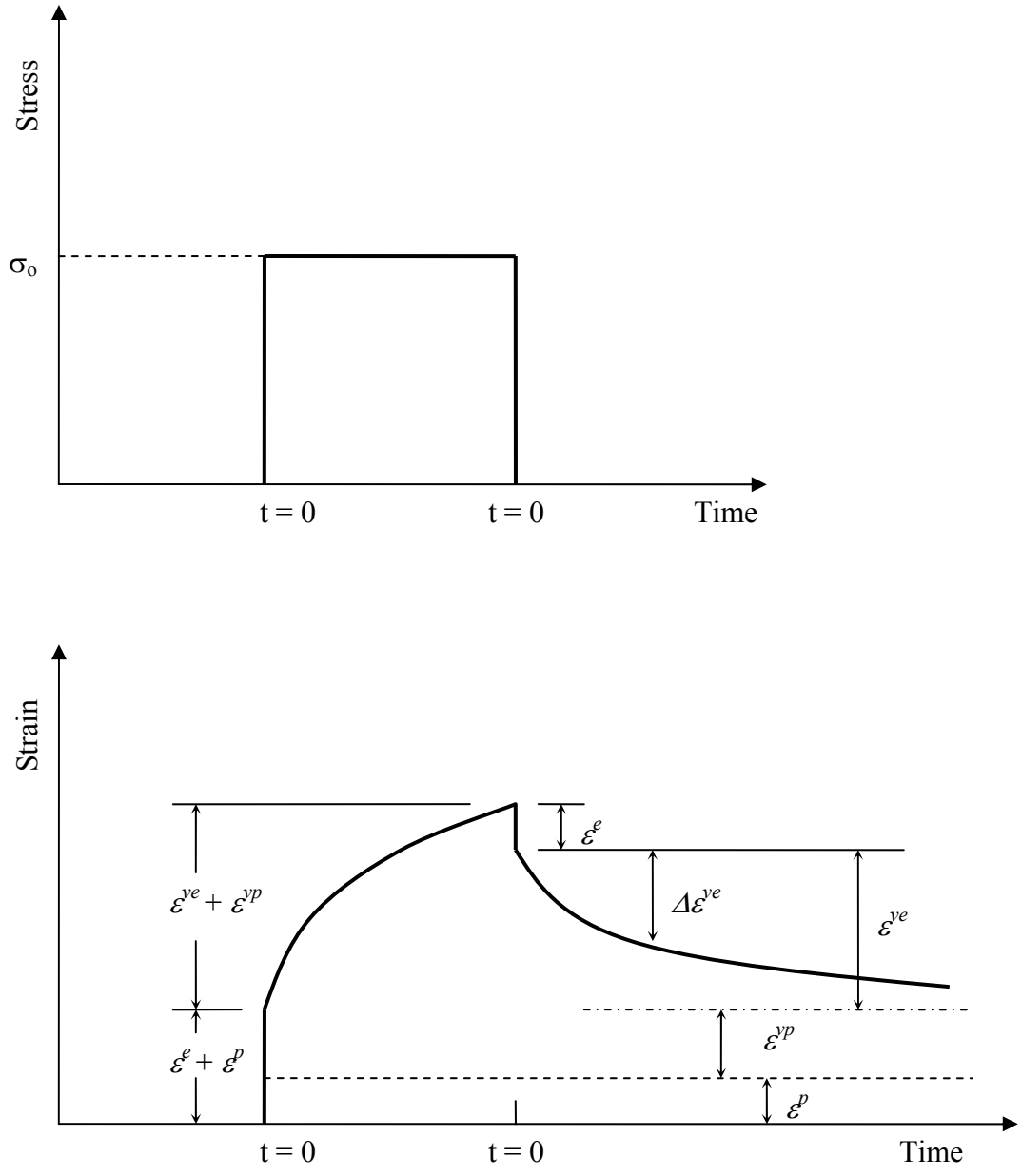

Fig. 2.1 Schematic Representation of the Various Strain Components in an Elasto-Visco-Plastic Material

For the sake of simplicity, some of the strain components are sometimes lumped into one component, particularly the irrecoverable components. For example, Abdulshafi and Majidzadeh (1984) and Bonnier (1993) lumped the irrecoverable components into one and the recoverable components into another, namely, a viscoplastic and a viscoelastic component, respectively. The relative contribution of each component is a function of temperature and strain rate as illustrated in Fig. 2.2 by Chehab et al. (2003). At relatively high temperatures/low strain rates, the viscoplastic component is the major contributor to the overall strain, whereas it is the opposite at low temperatures/high strain rates. Uzan (1996) showed that the irrecoverable components make up most of the axial and residual strain for AC at relatively high temperatures as shown in Fig. 2.3. Therefore, it is anticipated that rutting, which usually occurs during a very hot summer combined with heavy traffic loads, is mainly due to the viscoplastic (including plastic) deformation, whereas the viscoelastic component contributes very little to such a phenomenon. These findings were also supported by Sides et al. (1985) for sand-asphalt mixtures.

PLASTICITY-VISCOPLASTICITY

A complete account of the theory and application of plasticity must deal with the development of stress-strain relationships for elastic-plastic materials with work hardening as well as strain softening (Chen and Han 1988). The origin of plasticity dates back to a series of papers from 1864 to 1872 by Tresca on the extrusion of metals

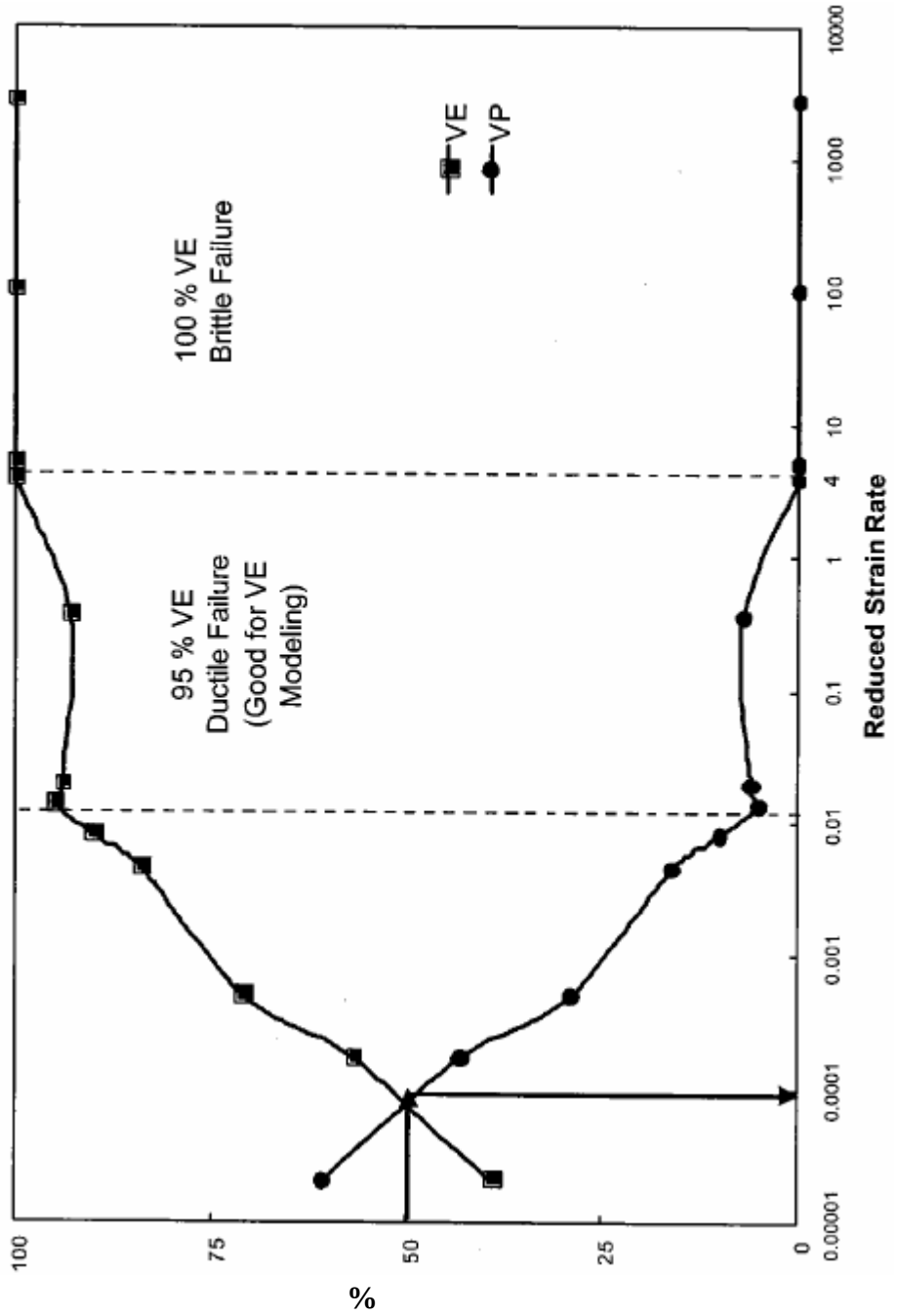

Fig. 2.2 Percent Viscoelastic and Viscoplastic Strains as a Function of Reduced Strain Rate at 77 ^{o}F (After Chehab et al. 2003)

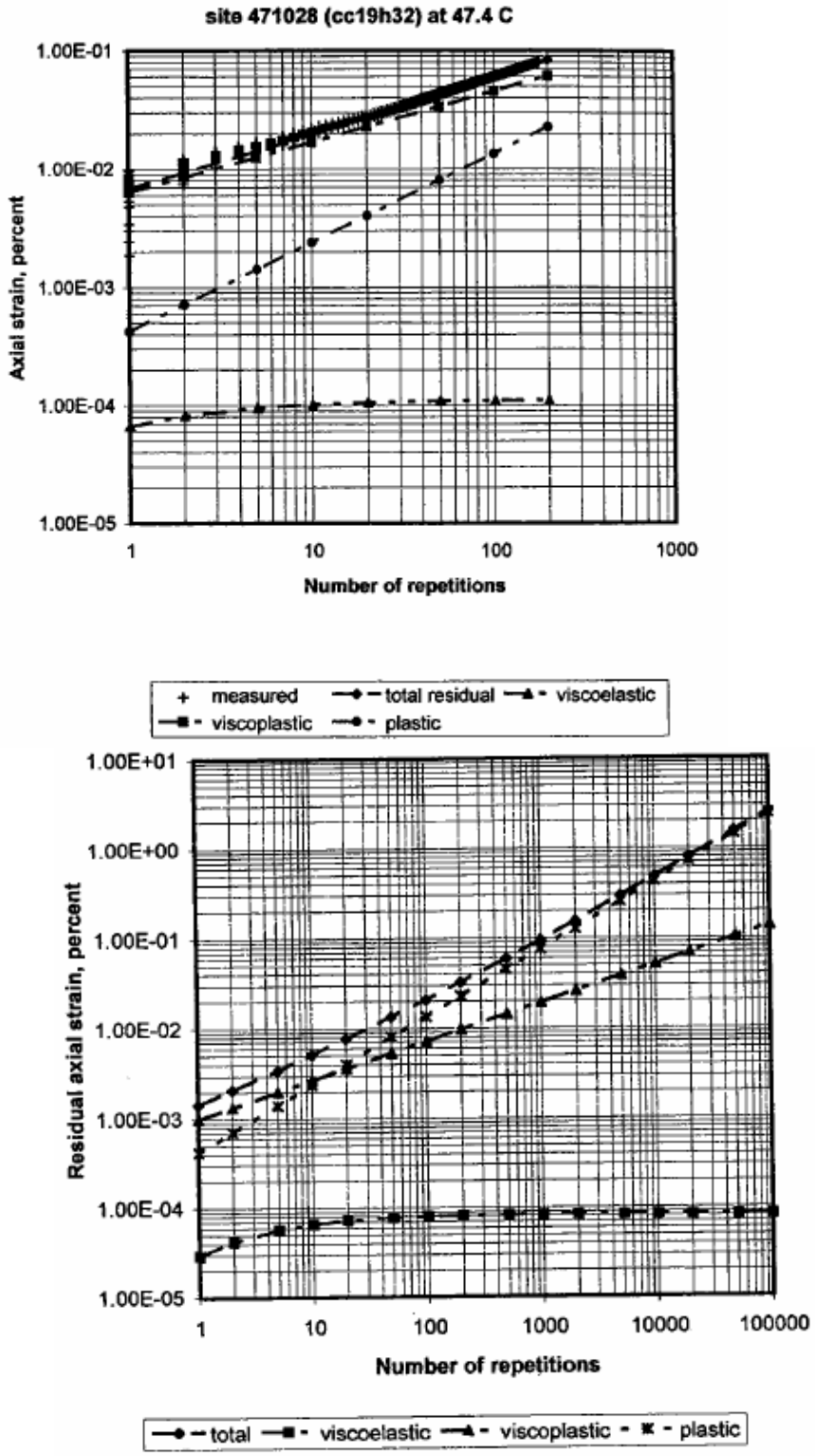

Fig. 2.3 Components of Axial and Residual Strain Versus Number of Repetitions at 105 ^{o}F (After Uzan 1996)

followed by a generalization by von Mises in a landmark paper in 1913 accompanied by his well known J_2-theory (Chen and Han 1988).

The theory of plasticity has been originally developed for metals. Deformational rules for metals have been firmly established and successfully used in engineering applications. Recently, the methods of plasticity have been extended and applied to study the deformational behavior of geological materials, such as rocks, soils and AC. The extension of plasticity theory to nonmetallic materials is probably one of the most active research subjects in the field of mechanics of materials at present, and various material models have been developed (Chen and Han 1988).

The flow rule is the necessary kinematic assumption postulated for plastic deformation or plastic flow. It gives the ratio or the relative magnitudes of the components of the plastic strain increment tensor $d\varepsilon_{ij}^{p}$. In 1928, von Mises proposed, similar to the elastic potential function, the concept of the plastic potential function, which is a scalar function of the stresses, $g(\sigma_{ij})$. The plastic flow rule equation can then be written as follows:

$$d\varepsilon_{ij}^{p} = d\lambda \frac{\partial g}{\partial \sigma_{ij}} \tag{2-2}$$

where $d\lambda$ is a positive scalar factor of proportionality, which is nonzero only when plastic deformation occurs. Eq. (2-2) implies that the plastic flow vector $d\varepsilon_{ij}^{p}$, if plotted as a free vector in stress space, is directed along the normal to the surface of plastic potential as shown in Fig. 2.4.

Of great importance is the simplest case when the yield function and the plastic

potential function coincide, i.e., $f = g$. Then:

$$d\varepsilon_{ij}^{p} = d\lambda \frac{\partial f}{\partial \sigma_{ij}} \tag{2-3}$$

and plastic flow develops along the normal to the yield surface $\frac{\partial f}{\partial \sigma_{ij}}$. Eq. (2-3) is called the associated flow rule because the plastic flow is connected or associated with the yield criterion, while Eq. (2-2) with $f \neq g$ is called the nonassociated flow rule.

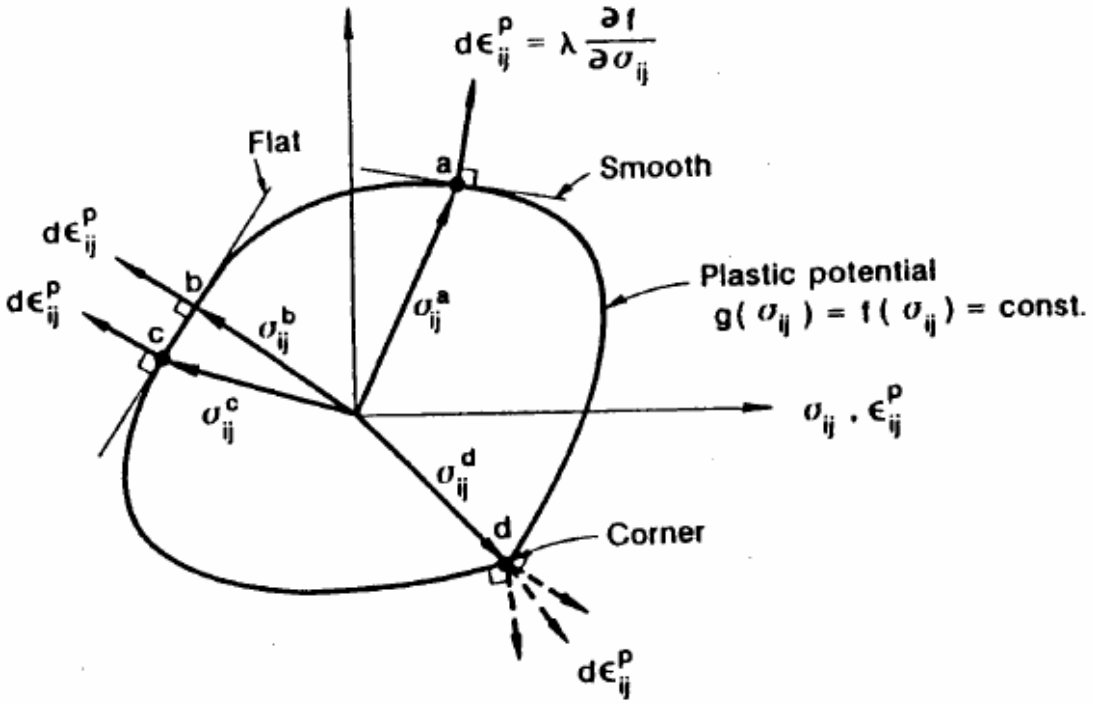

Fig. 2.4 Geometric Illustration of Associated Flow Rule (After Chen and Han 1988)

There are many studies in the literature on modeling the permanent deformation of AC. However, the theory of viscoplasticity is considered as the most suitable framework for modeling the time dependent response of AC. The theory has emerged as an attempt to provide a realistic, unified, phenomenological approach for materials exhibiting both plastic and creep deformations (Scarpas et al. 1997a). By retaining the classical plasticity notions of yield surface, decomposition of strains, and hardening, Perzyna (1966) proposed the following elegant formulation of the theory which is particularly suited for Finite Element (FE) implementation (Scarpas et al. 1997a):

$$\varepsilon = \varepsilon^{e} + \varepsilon^{vp} \tag{2-4}$$

$$\dot{\varepsilon} = \dot{\varepsilon}^{e} + \dot{\varepsilon}^{vp} \tag{2-5}$$

in which the dot denotes time derivative.

Perzyna's theory replaces the classical plastic flow rule with a time rate flow rule, which relates the rate of viscoplastic strain to the current stresses and loading history (Lu and Wright 1998). Analogous to the classical theory of incremental plasticity, the viscoplastic strain rate is computed by means of a postulated flow rule as follows:

$$\dot{\varepsilon}_{ij}^{vp} = \Gamma \cdot < \phi(f) > \cdot \frac{\partial g}{\partial \sigma_{ij}} \tag{2-6}$$

where, Γ is the fluidity parameter, which establishes the relative rate of viscoplastic strain; $\phi(f)$ is a scalar function of the argument f, which is the viscoplastic yield function; $\frac{\partial g}{\partial \sigma_{ij}}$ is a measure of the direction of the viscoplastic strain in which g is the viscoplastic

potential function and σ_{ij} is the stress tensor; and < > are the Macauley brackets to ensure that non-positive values of $\phi(f)$ lead to no viscoplastic deformation ($\dot{\varepsilon}_{ij}^{vp} = 0$). In case the viscoplastic yield surface coincides with the viscoplastic potential surface, the associated flow rule applies and *f* becomes equal to *g*.

There have been several mathematical expressions proposed in the literature for $\phi(f)$. Common to most of those is the dependency of the viscoplastic yield function on the state of stress and a hardening parameter (κ) as follows:

$$\phi(f) = fn(\sigma_{ij}, \kappa) \tag{2-7}$$

Scarpas et al. (1997a) stated that in a given stress increment, when as a result of hardening, the condition $\phi(f) \leq 0$ is fulfilled, the viscoplastic flow ceases and κ stops growing. It is only after the application of the next load increment that the overstress becomes positive ($\phi(f) > 0$), and hence viscoplastic flow occurs again as shown in Fig. 2.5. The exact form of $\phi(f)$ needs to be determined experimentally (Scarpas et al. 1997a).

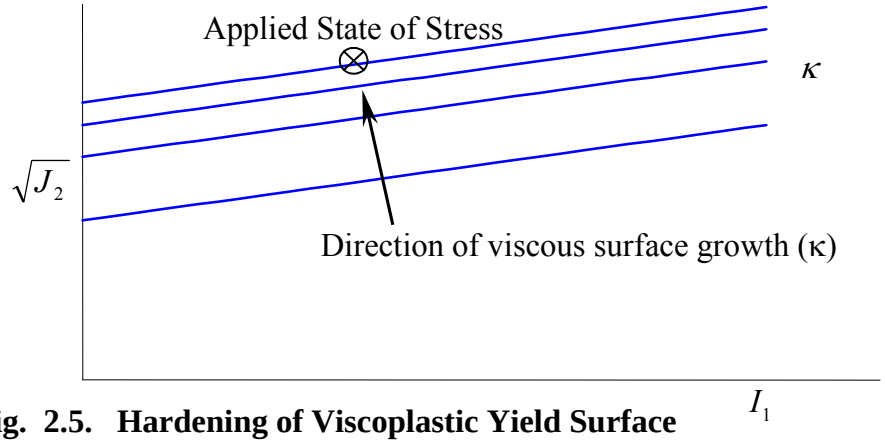

Fig. 2.5. Hardening of Viscoplastic Yield Surface

CONTINUUM MODELS FOR AC PERMANENT DEFORMATION

This section is a review of the continuum models that have been developed for AC throughout the literature in a chronological order.

Abdulshafi and Majidzadeh (1984)

Abdulshafi and Majidzadeh (1984) developed a one-dimensional combo visco-elastic-plastic constitutive model composed of Burger-type mechanical elements connected in series with a friction slider. The friction slider was used to represent the plastic deformation with Drucker-Prager yield function. The model was solved under creep phase loading conditions, and the solution was used to develop a rutting model that incorporated a densification phase represented by a relaxing spring. The developed model was supplemented by experimental tests to identify and numerically evaluate the model parameters.

The total strain was decomposed into a time-dependent and time-independent component, namely, a viscous and elasto-plastic component, respectively. The classical theory of elasticity and the theory of plasticity with the associated flow rule and Drucker-Prager yield criterion were used to model the elasto-plastic part. A Burger-type mechanical element was used to model the viscous part.

The experiment consisted of several tests to determine the model parameters, namely, diametral modulus of resilience, indirect tensile strength, unconfined compressive strength, incremental static compression, and incremental static indirect tension tests.

Sides et al. (1985)

Sides et al. (1985) developed a constitutive law for sand-asphalt mixtures subjected to compressive and tensile cyclic loading. The residual strain was decomposed into viscoelastic, plastic, and viscoplastic components that were incorporated into the model. The plastic component was modeled using a power law function of stress and number of load repetitions. The viscoelastic component was represented by a product of a power law function of time and stress. The viscoplastic strain, which was found to occur even for small stresses, was modeled with the same form used for the viscoelastic component, but with different parameters. The model parameters were determined from a series of repeated uniaxial creep and creep-recovery experiments performed under either compressive or tensile constant stress. Sides et al. (1985) showed that at a temperature of 77 ^{o}F, the residual strain mainly consists of the irrecoverable components (plastic and viscoplastic).

Desai and Zhang (1987)

Desai and Zhang (1987) developed a constitutive model for geological materials using Perzyna's theory of viscoplasticity in the context of the generalized hierarchical rate-independent associated plasticity approach. Although this model was originally developed for geological materials, particularly sand and rock salt, it has been modified and used by many researchers to model AC.

Desai and Zhang (1987) used a yield function in their model that has the following mathematical form:

$$f = J_2 - (\gamma I_1^2 - \frac{\alpha}{\alpha_o^{n-2}} I_1^n)[\exp(\beta_1 I_1) - \beta \frac{\sqrt[3]{J_3}}{\sqrt{J_2}}]^m \quad (2\text{-}8)$$

where α, n, γ, β, β_1, and m are response functions; α_o = 1 unit of stress; I_1 is the first invariant of the stress tensor, σ_{ij}; and J_2 and J_3 are the second and third invariants of the deviatoric stress tensor, S_{ij}, respectively. The yield function involved a single continuous yield surface for the hardening behavior, and hence avoided the use of two or multiple surfaces with the associated discontinuity. It permitted hierarchical development to incorporate progressive complexities such as associated and non-associated responses, anisotropic hardening, strain softening, and fluid pressure. The material parameters had physical meanings and were determined from laboratory multi-axial and triaxial tests under quasi-static conditions and creep tests.

The model was verified with stress-strain-time response of a sand and rock salt. It was then implemented in a nonlinear FE procedure which was used to solve a realistic problem involving time-dependent response of a cavity in the rock salt.

Sousa et al. (1993)

Sousa et al. (1993) developed a nonlinear elastic viscous with damage model to predict the permanent deformation of AC. The developed model was intended to capture important phenomena that influence the permanent deformation of AC including the dilatancy under shear loading, the effect of confining pressure on the shear modulus, the temperature and rate of loading dependency, and the residual accumulation of permanent deformation under repetitive loading. Sousa et al. (1993) emphasized that a valid

constitutive model for AC can't assume the material as isotropic and linear elastic. In addition, it is important to develop standardized test procedures to determine the material parameters for a constitutive model.

The model consisted of a number of three-dimensional Maxwell elements in parallel. Each Maxwell element was composed of a nonlinear spring and dashpot. The dilatancy effect and the increase in effective shear modulus under confining pressure are due to the aggregate skeleton, whereas temperature and rate dependency are associated with the asphalt binder (Sousa et al. 1993). The hardening was associated with the spring, and temperature and rate dependency were associated with the dashpot. Damage was accounted for by including a damage parameter in the equilibrium equation for the dashpot.

Simple shear at constant height, uniaxial strain, and volumetric tests were used to determine the nonlinear elastic material parameters. The viscous parameters were determined from the simple shear frequency sweep test, and the damage parameters were determined from the simple shear strain sweep test at constant height. Damage was found to follow an S-curve shape ranging between no damage at very low shear strain and almost complete failure at relatively high values of shear strain as shown in Fig. 2.6. Adding a damage component in their model significantly improved the ability to simulate test measurements.

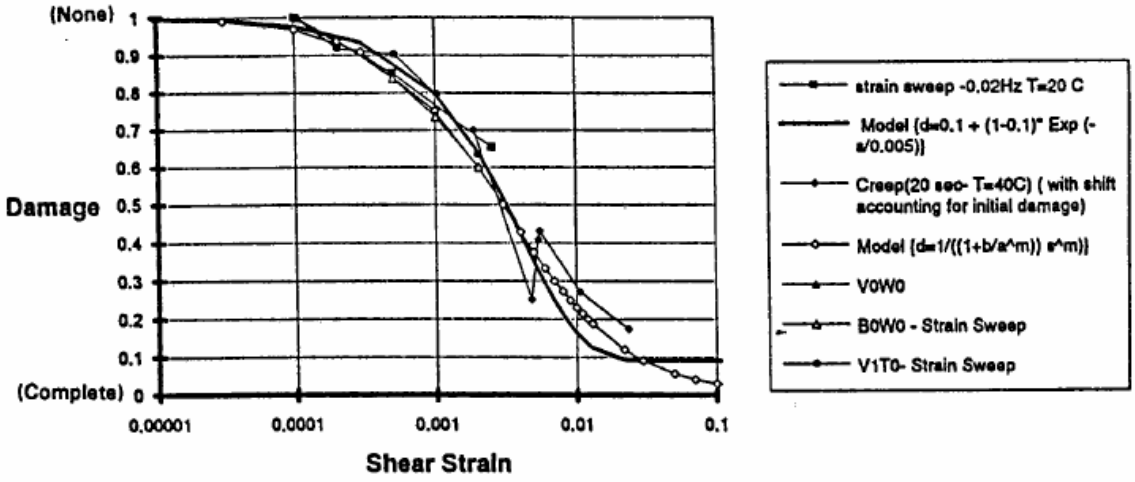

Fig. 2.6 Shape of the Damage Function Obtained from Shear Strain Sweeps and Shear Creep Tests (After Sousa et al. 1993)

Strategic Highway Research Program (SHRP) Report A-357 (Lytton et al. 1993)

Lytton et al. 1993 published a SHRP report on the development and validation of performance prediction models and specifications for asphalt binders and paving mixes. In their report, they developed a rutting model as part of a performance prediction model. The model used the stresses computed under one wheel of the dual wheel along a vertical line at the center of a FE mesh, Vermeer model (Vermeer 1984) to compute the permanent strain in the first load application, and the slope of the log ε^p - log N curve to compute the permanent strain at any number of load repetitions (N). It should be noted that the Vermeer model assumes the material to be isotropic, isotropic hardening, and the decomposition of the total strain into elastic, plastic due to shear, and plastic due to isotropic consolidation. The Vermeer model uses the Matsuoka and Nakai type yield function in calculating the plastic strain as follows:

$$f = -3pI_2 + AI_3 \tag{2-9}$$

where p is the hydrostatic pressure; I_2 and I_3 are the second and third invariants of the stress tensor; and A is a parameter that is a function of the plastic shear strain, shear modulus, mobilized angle of friction, and peak friction angle.

Florea (1994a, 1994b)

Florea (1994a) developed an associated elastic-viscoplastic model for bituminous concrete. The model was developed to describe mechanical characteristics specific to bituminous materials including dilatancy and compressibility of the volume, the null yield limit, and the time-effect phenomena. The model was developed based on the assumption that bituminous concrete is homogenous and isotropic, and that the deformations and rotations may be considered small. The total strain rate was decomposed into an elastic and irrecoverable component. The theory of elasticity was used to model the elastic component and Perzyna's theory of viscoplasticity was used to model the irrecoverable component with an associated flow rule. The model was found to describe well the mechanical characteristics of bituminous materials from a qualitative point of view, but not from a quantitative point of view.

Florea (1994b) improved the model developed by Florea (1994a) by using a plastic potential function different than the yield function, i.e., non-associated flow rule. Using the non-associated flow rule enabled the developed model to describe both from a qualitative and from a quantitative point of view the mechanical characteristics of bituminous concrete.

Sousa and Weissman (1994)

Sousa and Weissman (1994) provided a better insight into the rutting phenomena and laid down fundamentals for a better prediction of rutting in AC pavements. Sousa and Weissman (1994) stated that a constitutive model for AC rutting should account for several phenomena that are in play during the deformation including: rate and temperature dependency; dilatancy; the material response to compression is different than that in tension; cyclic loading leads to crack development; residual deformations are observed at the end of loading cycles; material behavior is strongly dependent on air void contents; aging can play an important role in the development of permanent deformation; and in some mixes, moisture damage plays an important role in the development of permanent deformation.

The nonlinear viscoelastic model developed by Sousa et al. (1993) failed to provide a good representation of the AC behavior under cyclic loading. Sousa and Weissman (1994) enhanced the developed nonlinear viscoelastic model by including an elastoplastic component using the associated J_2-plasticity (von Mises yield surface) with isotropic and kinematic hardening. The yield function, flow rule, and hardening laws were given as follows:

$$f(\sigma, q) = \|\eta\| - \sqrt{\frac{2}{3}K(\alpha)} \tag{2-10}$$

$$\dot{\varepsilon}^p = \dot{\gamma}\frac{\eta}{\|\eta\|} \tag{2-11}$$

$$\dot{q} = \dot{\gamma}\frac{2}{3}H(\alpha)\frac{\eta}{\|\eta\|} \tag{2-12}$$

$$\dot{\alpha} = \dot{\gamma}\sqrt{\frac{2}{3}} \tag{2-13}$$

where α defines the isotropic hardening and q defines the kinematic hardening of the von Mises yield surface; $\dot{\gamma}$ is the proportionality constant; $K(\alpha)$ and $H(\alpha)$ are the isotropic and kinematic hardening moduli, respectively; and η was defined as follows:

$$\eta = dev[\sigma] - q, tr[q] = 0 \tag{2-14}$$

The material parameters were determined from several tests that consisted of constant height shear creep, shear frequency sweeps at constant height, uniaxial strain, hydrostatic, and repetitive simple shear at constant height. Although the model could not address all the aforementioned phenomena affecting the behavior of AC, the developed model captured some of them and was implemented in a FE simulation of a full depth pavement section to predict rut depth.

Scarpas et al. (1997a)

Scarpas et al. (1997a) presented a profound article on the constitutive modeling of AC and its implementation in FE simulation to predict its response. Their model utilized Perzyna's theory of viscoplasticity with Desai's yield surface (Desai et al. 1986, Desai and Zhang 1987, Desai 1990) to model the viscoplastic deformation of AC as follows:

$$f = \frac{J_2}{P_a^2} - F_a \cdot F_b \tag{2-15}$$

in which,

$$F_a = \gamma\left(\frac{I_1 + R}{P_a}\right)^2 - \alpha\left(\frac{I_1 + R}{P_a}\right)^n \tag{2-16}$$

$$F_b = \left(1 - \beta \cdot \cos 3\theta\right)^{-1/2} \tag{2-17}$$

$$\cos 3\theta = \frac{3\sqrt{3}}{2} \cdot \frac{J_3}{J_2^{3/2}} \tag{2-18}$$

where I_1, J_2, and J_3 are the first invariant of the stress tensor, the second invariant of the deviatoric stress tensor, and the third invariant of the deviatoric stress tensor, respectively; P_a is the atmospheric pressure; R is the triaxial tensile strength; and α, β, γ, and n are material parameters defining the yield surface.

Scarpas et al. (1997a) also included an additional strain component, ε_{cr}, to account for damage due to crack formation as follows:

$$w = l_c \cdot \varepsilon_{cr} \tag{2-19}$$

where w is the crack opening and l_c is a characteristic length scale.

Monotonic triaxial compression and tension tests were used to determine material parameters related to path and rate dependency, and incremental creep tests were used to determine material parameters related to hardening and viscosity. The model was implemented in a dynamic nonlinear FE system to simulate flexible pavement response. The FE simulation showed that all elements in the vicinity of the load were subjected to intense shearing deformation and that the shear stresses (compression and tension) comprised the major domain of the pavement top layer response. Scarpas et al. (1997a) noted that shear-compression can be applied by a standard triaxial testing apparatus whereas shear-tension is less easy to apply. In addition

to the shearing deformation, some elements were subjected to compression in the horizontal direction and some in tension. Those horizontal stress components (confining pressure) should not be neglected.

Lu and Wright (1998)

Lu and Wright (1998) developed a visco-elastoplastic model to describe AC behavior. The total strain was decomposed into elastic, viscoelastic, and viscoplastic components. Hooke's law was used to model the elastic component; a power law function of stress and time was used to model the viscoelastic component; and Perzyna's theory of viscoplasticity was utilized to model the viscoplastic component, which was considered to include the plastic component as well. The yield surface was expressed in terms of the first invariant of the stress tensor, the second and third invariants of the deviatoric stress tensor, and a hardening parameter. The model was implemented in a FE system to investigate the development of rutting in flexible pavement structures.

Seibi et al. (2001)

Seibi et al. (2001) developed a model for AC characteristics related to pavement behavior. AC behavior was experimentally studied under high rates of loading using uniaxial, triaxial, and pavement simulation tests. The total strain was decomposed into elastic and viscoplastic components. The viscoplastic component was modeled using Perzyna's theory of viscoplasticity with Drucker-Prager yield criterion as follows:

$$f = \sqrt{J_2} - \frac{1}{3}\tan\beta \cdot I_1 + (1 - \frac{1}{3}\tan\beta)\sigma_c^o \qquad (2\text{-}20)$$

where β is the friction angle; σ_c^o is the static uniaxial compression yield stress; and I_1 and J_2 are the first and second invariant of the stress and deviatoric stress tensors, respectively.

Seibi et al. (2001) developed an optimization technique in the FE results in order to effectively identify the material parameters to generalize the multiaxial stress-strain relations.

Huang et al. (2002)

Huang et al. (2002) developed a thermo-visco-plastic model for AC that incorporated the temperature and loading rate into the Hierarchical Single Surface (HiSS) plasticity model developed by Desai et al. (Desai et al. 1986, Desai and Zhang 1987, Desai 1990). According to Huang et al. (2002), HiSS models are elasto-plastic constitutive models that share the same yield surface. The hierarchical approach allowed for progressive development of models with higher grades corresponding to different levels of complexities. Initially an isotropic material with isotropic hardening and associated plasticity was treated as the basic model that involved no deviation from normality to the yield surface. Models of higher grades such as isotropic hardening with non-associative response due to friction or induced anisotropy can be obtained by superimposing modifications or corrections to the basic model. Huang et al. (2002) used the same yield surface developed by Desai and used by Scarpas et al. (1997a) in Eqs. (2-15, 2-16, 2-17, 2-18).

A series of triaxial and creep tests at three temperatures were performed to

determine the material parameters. A back-predicting algorithm for the triaxial test strains based on loading stress path was developed, and the model was compared to the experimental results based on this algorithm.

Modeling AC

There is a common trend in the literature on constitutive modeling of AC to decompose the strain into different components and model each one individually. Researchers have used different techniques to model the individual strain components including mechanical elements such as Burger-type and Maxwell-type elements; power law functions of stress, time, and number of load repetitions; and Perzyna's theory of viscoplasticity, which has been successfully utilized to model the permanent deformation of AC. The main challenge in Perzyna's theory is contained in selecting or developing an appropriate yield function that can account for the several phenomena influencing AC behavior.

Parallel to the importance of developing a valid constitutive model, many researchers have emphasized the importance of developing standardized test procedures to determine the model parameters (Sousa and Weissman 1994, Cela 2002). Lytton (2000) and Cela (2002) have shown that the triaxial strength test is one of the most suitable testing apparatuses for its relative simplicity and accuracy compared to other tests and for inducing a state of shear action, which is believed to be the main state of stress that causes rutting in asphalt pavements (Scarpas et al. 1997a).

Many researchers have addressed the importance of damage and its evolution in properly modeling AC (e.g. Schapery 1982, Schapery 1987, Sousa et al. 1993, Schapery 1994, Park et al. 1996, Kim et al. 1997, Scarpas 1997a, Lee et al. 2000, Sadd et al. 2003, Collop et al. 2003). Park et al. (1996) stated that any mathematical model that duly describes the constitutive behavior of AC must account for the effect of damage growth. Sousa et al. (1993) noted that adding a damage component to a permanent deformation model significantly improves its ability to predict experimental measurements. However, almost all the available continuum damage models were developed without any experimental measurements or verification of the evolution laws of damage.

In addition, the majority of the available continuum models for AC do not account for the effect of the microstructural anisotropy on the material response. Tashman et al. (2001) showed that AC exhibits transverse anisotropic microstructure distribution due to the preferred aggregate orientation towards the horizontal direction. This anisotropic nature of AC makes the induced strain noncoaxial with the applied stress, and consequently, the associated flow rule is inapplicable to AC, and granular materials in general (Zeinkiewicz et al. 1975, Oda and Nakayama 1989, Florea 1994a, Florea 1994b).

The following sections will capitalize on the anisotropy and how to include it in a continuum model, and on damage and how to experimentally characterize its evolution.

ANISOTROPY

Anisotropy is caused by a preferred orientation of the nonspherical particles

within the material's microstructure. As a result, the nonspherical particles are not completely randomly distributed and the material's behavior is anisotropic. Anisotropy causes a coupling between the volumetric response and deviatoric action. Also, the principal directions for the incremental stress and strain tensors do not coincide (Chen and Han 1988). This non-coaxiality is believed to be one of the fundamental aspects of granular soils (Gutierrez et al., 1991). Chen and Han (1988) stated that the anisotropy and coupling effects are important features in modeling the behavior of many materials, such as: concrete; soil; and AC, for which inelastic dilation or compaction are dominant effects. Yasufuku (1990), on the basis of his experiments on sand, has pointed out that the plastic potential function is similar in shape to the yield function. However, the principal axes of plastic strain increment do not coincide, in general, with the principal axes of stress, which leads to the so-called non-coaxiality. Thus, anisotropic granular materials generally do not follow the associated flow rule.

Isotropic failure theories have been available for over a century. Though none of these theories have been generalized, engineers have succeeded in matching many common materials with an applicable failure theory (Arramon et al. 2000). However, unlike their isotropic counterparts, anisotropic materials exhibit directionally dependent mechanical properties and thus the isotropic theories are inapplicable for them (Arramon et al. 2000). Plasticity theory dealing with anisotropic materials is not new. In fact, many plasticity models have been published over the past two decades especially for soil (e.g. Mroz et al. 1979, Baker and Desai 1984, Liang and Shaw 1991). Yield functions dealing with anisotropic materials are obtained by generalizing any yield function proposed for

isotropic ones, where the stress invariants are substituted by the corresponding joint invariants including a microstructure tensor.

Microstructure Tensor

In relation to material anisotropy, Casagrande and Carillo (1944) first discriminated between the inherent anisotropy and the induced anisotropy. The former is produced through the sedimentation of particles, while the latter is induced afterward during the process of nonelastic deformation. Oda and Nakayama (1989) stated that there are three sources of anisotropy: (1) the anisotropic distribution of contact normals which is indicative of the mutual relation among particles; (2) the preferred orientation of nonspherical air voids; and (3) the preferred orientation of nonspherical particles. In biaxial compression tests on two-dimensional assemblies of rods, Oda and Nakayama (1989) observed that the inherent anisotropy by (1) and (2) tends to be completely altered during the relatively early stage of nonelastic deformation, while the inherent anisotropy by (3) still remains at the later stage of deformation.

Oda and Nakayama (1989) introduced a microstructure tensor $\overline{F}_{ij}$ which gives a measure of the two-dimensional anisotropy produced by the preferred orientation of nonspherical particles as shown in Fig. 2.7, i.e.,

$$\overline{F}_{ij} = \int_{\Omega} m_i m_j E(m) d\Omega \qquad (i, j = 1, 2) \tag{2-21}$$

where m_i (i = 1, 2) are components of a unit vector m projected on the orthogonal reference axes x_i (i = 1, 2); Ω is a solid angle corresponding to the two-dimensional plane

($\Omega = 2\pi$); and *E(m)* is a probability density function that describes the spatial distribution of the vector *m*. Fig. 2.8 shows a vertical section of a granular material where θ^k is the inclination angle of a unit vector m^k corresponding to a k^{th} particle on a two-dimensional section of the material and ranges between –90° and +90°. Since m_1^k and m_2^k are $sin\theta^k$ and $cos\theta^k$, respectively, the components of $\overline{F}_{ij}$ are calculated as follows:

$$\overline{F}_{11} = \frac{1}{M}\sum_{k=1}^{M} \sin^2 \theta^k \tag{2-22}$$

$$\overline{F}_{12} = \frac{1}{M}\sum_{k=1}^{M} \sin\theta^k \cos\theta^k \tag{2-23}$$

$$\overline{F}_{22} = \frac{1}{M}\sum_{k=1}^{M} \cos^2 \theta^k \tag{2-24}$$

where *M* is the total number of measurements. Since $\overline{F}_{ij}$ is a symmetric second order tensor, the components can always be converted into two principal values $\overline{F}_1$ and $\overline{F}_2$ in the corresponding principal directions θ_1 and θ_2 of the material anisotropy as follows:

$$\begin{Bmatrix} \overline{F}_1 \\ \overline{F}_2 \end{Bmatrix} = \begin{Bmatrix} \frac{1}{2}(\overline{F}_{11}+\overline{F}_{22}) - \left[\frac{1}{4}(\overline{F}_{11}-\overline{F}_{22})^2 + \overline{F}_{12}^{\,2}\right]^{\frac{1}{2}} \\ \frac{1}{2}(\overline{F}_{11}+\overline{F}_{22}) + \left[\frac{1}{4}(\overline{F}_{11}-\overline{F}_{22})^2 + \overline{F}_{12}^{\,2}\right]^{\frac{1}{2}} \end{Bmatrix} = \begin{Bmatrix} \frac{1}{2}(1-\Delta) \\ \frac{1}{2}(1+\Delta) \end{Bmatrix} \tag{2-25}$$

where Δ is the vector magnitude, which was introduced by Curray (1956) as follows:

$$\Delta = \frac{1}{M}\left[\sum_{k=1}^{M}(\cos 2\theta^k)^2 + \sum_{k=1}^{M}(\sin 2\theta^k)^2\right]^{\frac{1}{2}} \tag{2-26}$$

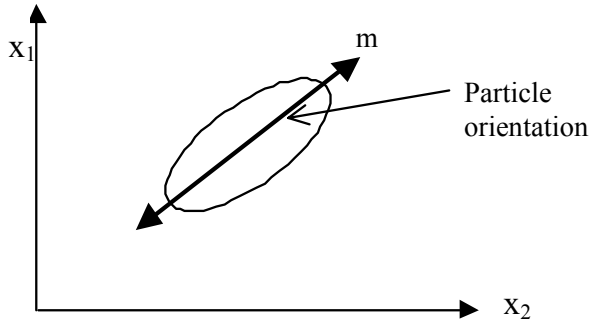

Fig. 2.7. Preferred Orientation on Nonspherical Particles

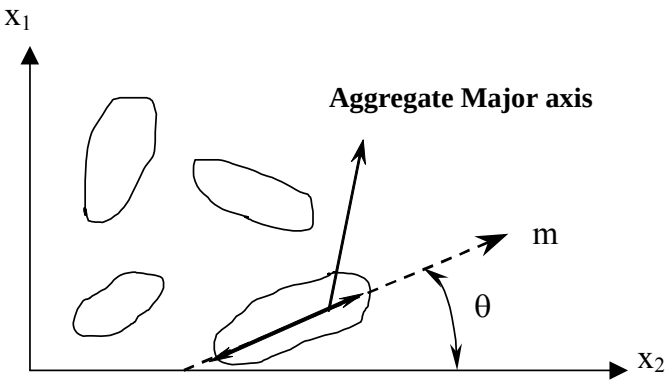

Fig. 2.8. Two-Dimensional Particles Orientation in a Vertical Section

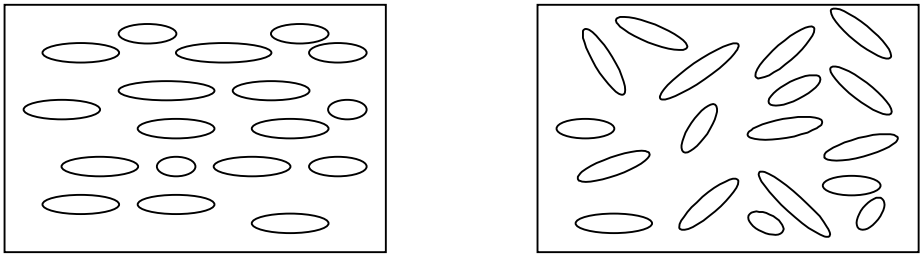

Uniform Distribution
Δ=1.00
Transverse Anisotropic Material

NonUniform Distribution
Δ=0.00
Isotropic Material

Fig. 2.9. Effect of Aggregate Distribution on the Material Properties

The vector magnitude describes the aggregate preferred orientation measured on two-dimensional images and is a function of aggregate shape properties and distribution. In order to formulate the two-dimensional microstructure tensor $\overline{F}_{ij}$ in three-dimension, it was assumed that the inherent anisotropy exhibits axial symmetry with an axis of symmetry parallel to the direction of the applied load. The second assumption made was that:

$$\frac{F_1}{F_2} = \frac{\overline{F}_1}{\overline{F}_2} \tag{2-27}$$

indicating that the principal values $\overline{F}_1$ and $\overline{F}_2$ in two-dimension were assumed to be proportional to the principal values F_1 and F_2 in three-dimension. These assumptions lead to the three-dimensional microstructure tensor F_{ij} as follows:

$$\mathrm{F_{ij}} = \begin{pmatrix} (1-\Delta)/(3+\Delta) & 0 & 0 \\ 0 & (1+\Delta)/(3+\Delta) & 0 \\ 0 & 0 & (1+\Delta)/(3+\Delta) \end{pmatrix} \tag{2-28}$$

Theoretically, the value of Δ ranges between zero and unity. A zero value indicates the aggregates are completely randomly distributed, which is analogous to isotropic materials, and a unity value indicates the aggregates are all oriented in one direction as illustrated in Fig. 2.9.

The stress invariants can now be substituted by the corresponding joint invariants with the microstructure tensor in Eq. (2-28) to account for anisotropy.

Image Analysis Techniques

One of the main blocks in accounting for the effect of the anisotropy in a continuum model for AC has always been the difficulty associated with capturing the microstructure and quantifying the anisotropy. Recently, there have been several successful attempts to capture and quantify the microstructure of AC mixtures using imaging technology. Yue et al. (1995) used image processing techniques to obtain quantitative information about the distribution and shape of the aggregate particles. Masad et al. (1998, 1999a, 1999b) and Tashman et al. (2001) developed Image Analysis Techniques (IAT) to quantify the microstructure of AC based on aggregate orientation, aggregate gradation, aggregates contacts, aggregate segregation, and air void distribution. These techniques can be easily implemented to quantify the anisotropy of the aggregate orientation in two-dimensional cut sections of AC.

DAMAGE

A new discipline has been developed recently to investigate the growth of microcracks and the mechanical behavior of damaged materials by representing the effect of distributed cracks in terms of certain mechanical variables (Murakami 1983). This method is called continuum damage mechanics (CDM), in which damage is defined as a microstructural change that induces some deterioration in the material. Kachanov (1958) introduced the concept of the effective stress theory which has been successfully implemented to describe damage in terms of crack nucleation and growth within the framework of CDM (e.g. Murakami 1983, Lemaitre 1985, Zbib and Aifantis 1986,

Chaboche 1988, Kattan and Voyiadjis 1990, Voyiadjis and Kattan 1990, Voyiadjis and Kattan 1992).

The effective stress theory postulates that the material damage can be characterized mainly by the decrease of the load-carrying effective area caused by the development of microscopic cracks and cavities (Murakami 1988). The theory postulates that a damaged material subjected to a state of stress can be represented by a perfect material subjected to a fictitious stress. The fictitious stress is equal to the stress applied to the damaged material magnified by the decrease in the load-carrying effective area as shown in Fig. 2.10. This magnification factor is referred to as the damage parameter and is an indication of the material's state of damage.

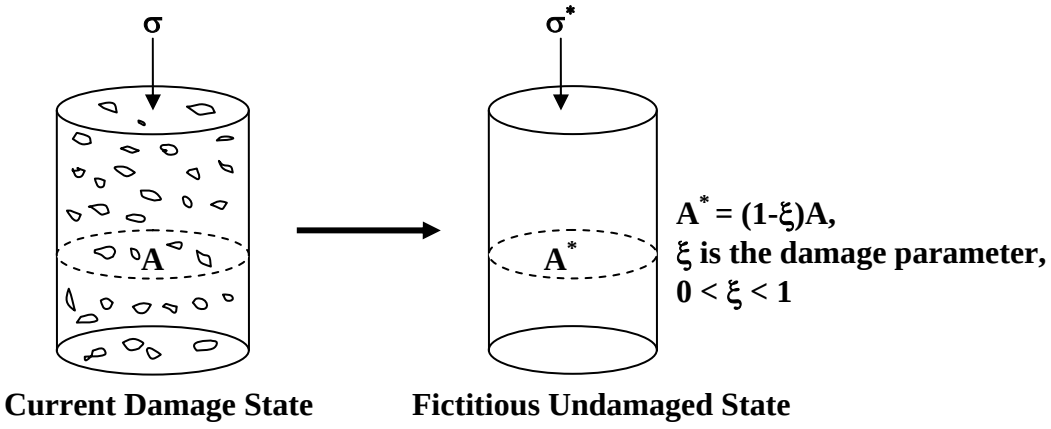

Fig. 2.10. Damage-Effective Stress Theory

Characterizing Damage Using X-Ray Computed Tomography

X-Ray Computed Tomography (CT) is fast becoming a powerful nondestructive tool in characterizing the microstructure of many engineering materials such as concrete, soil, rocks, metals, and AC. Although some of these materials vary significantly in their microstructural composition and distribution, the motivation behind using this new technology has been the same, and that is the nondestructiveness nature of X-Ray CT, its accuracy, and the complexity of the material microstructure.

Mummery et al. (1993) used X-Ray microtomography to characterize the damage occurring on plastic straining of silicon carbide particle-reinforced aluminum alloys. Their characterization was based on density measurements as a function of strain in addition to imaging of the internal structure. Imaging allowed for a more accurate determination of microstructural damage in terms of air void growth than is available from measurement of density using buoyancy methods or from decreasing elastic modulus.

Synolakis et al. (1996) presented a new method for computing the microscopic internal displacement fields associated with permanent deformations of three-dimensional AC cores while satisfying the small gradient approximation of continuum mechanics. They computed the displacement field associated with diametral loading of a cylindrical asphalt core using X-Ray CT to collect three-dimensional images from sequences of two-dimensional images scanned before and after loading. The pair of three-dimensional images were then used to compute the displacement field by comparing their three-dimensional representation before and after the deformation.

Shi et al. (1999) used X-Ray CT to monitor the evolution of internal failure in different soils, particularly the formation of shear bands. They used an apparatus that can be fitted into the chamber of a medical CT. CT images were then taken on different cross-sections inside the specimens at different loading stages to monitor soil deformation continuously. They showed that X-Ray CT is a powerful non-destructive tool for studying the deformation patterns and capturing the formation of cracks and shear bands in soils.

Landis and Keane (1999) used a high resolution X-Ray microtomography to measure internal damage and crack growth in small mortar cylinders loaded in uniaxial compression. In their experiment, small mortar cylinders were inserted into a small loading frame that could be mounted directly on the X-Ray rotation table. This was done in order to scan the specimens at varying strain values so that internal damage could be quantified and correlated with load deformation information. Aluminum was chosen for the loading frame because of its relatively low X-Ray absorption, leading to better X-Ray absorption resolution in the specimens. Multiple tomographic scans were made of the same specimen at different levels of deformation applied through a custom built loading frame, and image analysis of the scanned images was used to measure the internal crack growth during each deformation increment.

Landis and Keane (1999) showed that under monotonic loading of concrete, there was elastic deformation up to 30% of peak load. Beyond this point, cracking occurred at the cement-aggregate interface. At about 70% of the peak load, these distributed cracks started to localize, and matrix cracking occurred which macroscopically became large-scale axial

splitting. Post-peak response was characterized by additional matrix cracking and frictional mechanisms in a relatively narrow band. However, measured post-peak behavior was found to be highly dependent on the testing set up and specimen geometry.

Maire et al. (2001) conducted a study to three-dimensionally characterize the microstructure and damage in structural light metals using X-Ray CT. They were able to detect cracks with an opening of 0.5-μm which was below their voxel size. In their experiment, a first scan was performed without any applied load, in order to characterize the initial non deformed state. Thereafter, the load was applied and another scan was performed while the crosshead position was maintained constant. Five scans with increasing strain levels were performed on the same sample. Their analysis gave valuable information about the internal structure and its evolution during the deformation of the samples studied.

Hu et al. (2001) studied the internal structure damage evolution in Bi-2223/Ag HTS tapes under tensile loading using synchrotron radiation X-Ray projection imaging. They found that damage exists originally in the tape; and with increasing applied load, initiation and growth of microcracks was observed until the end of the linear elastic region. Thereafter, the material began to lose its superconducting capability as the material started to plastically flow and the microcracks became penetrable ones. This point was referred to as the critical density after which the density of the material decreased rapidly and drastically.

Statistical Analysis of Air Void Distribution in AC

Wang et al. (2001) stated that a statistical study of the air void size and spatial distribution would present valuable information leading to a better understanding of the rutting and fatigue mechanisms of AC. In their work, Wang et al. (2001) studied the spatial and size distribution of the air voids in different WesTrack mixes (fine, fine plus, and coarse), including the quantification of damage in terms of specific air void surface area and the average distance between damage surfaces (air voids). They used X-Ray CT imaging and a virtual cutting technique to conveniently obtain the cross-sections in different orientations. The damage distribution was related to the performance of the three mixes. They found that the coarse-graded mix was more severely inherently damaged and that the mean solid path (average distance between air void surfaces) was a comprehensive parameter for measuring the damage effects: the smaller the mean solid path, the larger the interaction among damage surfaces and therefore the lower the resistance to fatigue and rutting. On the other hand, the specific damage surface area could not rank the mixes according to their performance.

Masad et al. (2002a) used X-Ray CT along with IAT to characterize the statistical distribution of air void sizes at different depths in AC specimens. They found that air voids follow a Weibull distribution which was used to quantify the effect of compaction effort, method of compaction, and aggregate size distribution on air voids. They also found that air void size distribution in Superpave gyratory compacted specimens exhibit a “bath-tub” shape where larger air voids were present at the top and bottom parts of a specimen. This shape was more pronounced at higher compaction efforts. Specimens prepared with

different aggregate sizes were found to have noticeably different air void sizes. Specifically, larger air voids were present in specimens that consisted of smaller aggregate particles.

Damage Characterization

The literature on damage characterization showed that X-Ray CT is a powerful tool to characterize and capture the damage within a material microstructure. Its power stems from the fact that it is non-destructive; hence the tested specimen is still intact for further mechanical testing where the captured microstructure can then be related to the material's macro behavior. In addition, it provides accurate information in which no assumptions are made about the microstructure.

Although some researchers were able to utilize X-Ray CT to characterize the evolution of damage in some engineering materials and relate it to the measured strain, this has not yet been applied to AC in which the focus of the research was mainly on characterizing air void distribution but not damage evolution as the material undergoes deformation. This is vital to continuum damage modeling where there is always a need for a damage evolution law.

Damage distribution has been shown to be non-uniform, thus it is not sufficient to quantify the damage visually and relate it to the overall deformation of the material. Rather a statistical analysis of damage distribution and its evolution needs to be conducted to properly characterize the damage within the AC microstructure.

CHAPTER III

MICROSTRUCTURAL VISCOPLASTIC CONTINUUM MODEL FOR ASPHALT CONCRETE

OVERVIEW

Permanent deformation is one of the most significant distresses that causes severe damage in Asphalt Concrete (AC) pavements. It is caused by high traffic loads associated with high field temperatures. An anisotropic viscoplastic continuum damage model is developed to describe the permanent deformation of asphalt pavements. The model is based on Perzyna's formulation with Drucker-Prager yield function modified to account for the material anisotropy and microstructure damage. The material anisotropy is captured through microstructural analysis of two-dimensional sections of AC in terms of aggregate distribution. Furthermore, a damage parameter is included in the model in order to quantify the nucleation of cracks and growth of air voids and cracks (voids).

A parametric study is conducted to study the effect of the model parameters on its response. This study demonstrates the sensitivity of the model to strain rate, aggregate distribution, and microstructure damage. Triaxial strength and static creep tests data obtained from the Federal Highway Administration (FHWA) Accelerated Loading Facility (ALF) are used to determine the model parameters. The model is shown to match the experimental data well.

INTRODUCTION

It is well known that AC has a complex microstructure resulting from the nonuniform distribution of its constituents, namely, aggregates, asphalt binder and the associated air voids. Each one of these individual constituents forms a complex material in itself. Aggregates vary in shape (form, angularity, and texture), size, as well as mechanical properties. Asphalt binder is an elasto-visco-plastic material that binds the aggregates together, and consequently formulates the microstructure of the AC along with the bound aggregates and associated air voids. Though the air voids do not possess any appreciable mechanical strength, their distribution is important in determining the overall response of the material (Krishna and Rajagopal 2002).

One of the most important failures in asphalt pavements is caused by permanent deformation under high service temperatures, traditionally referred to as the rutting phenomenon. Researchers have adopted two main approaches in modeling permanent deformation: the continuum modeling approach and the micro-mechanistic modeling approach. In the continuum modeling area, Sides et al. (1985) developed a viscoelasto-plastic constitutive model for sand-asphalt mixtures. In their model, the total strain was separated into plastic, viscoelastic, and viscoplastic components, where the strain components were generally power law functions of the stress level, time, and number of repetitions. The research team of the Strategic Highway Research Program (SHRP) developed a rutting model for AC using the stresses computed under one wheel of the dual wheel and the Vermeer model to compute the permanent strain in the first load application (Lytton et al. 1993). The model related the total accumulated permanent

strain under the wheel load to that occurred in the first load application. The model was chosen for its simplicity (using Mohr-Coulomb failure criteria) and its ability to fit real material behavior, but it created mathematical problems in the Finite Element (FE) analysis when the frictional angle was large (Lytton et al. 1993).

Sousa et al. (1993) developed a nonlinear viscoelastic with damage model to predict permanent deformation that focused on capturing: a) dilatancy due to shear; b) increase of effective shear modulus under increased hydrostatic pressure; c) significant effect of temperature and rate of loading; and d) residual accumulation of permanent deformation under repetitive loading. Sousa and Weissman (1994) also developed an elastoviscoplastic model for the permanent deformation of AC by including a simple elastoplastic component (associative J_2-plasticity with both isotropic and kinematic hardening) into a nonlinear viscoelastic constitutive law.

Florea (1994a, b) presented isotropic associated and non-associated viscoplastic models for AC to describe its mechanical characteristics. Florea (1994a) stated that a constitutive model for bituminous concretes should account for the dilatancy and compressibility of the volume, the null yield limit, and the time effect phenomena. Scarpas et al. (1997a) presented a viscoplastic damage model based on Perzyna's formulation and Desai's yield surface to capture the macroscopic response of AC under different loading conditions. Lu and Wright (1998) used the associated viscoplastic flow rule with Perzyna's theory to develop a FE code for visco-elastoplastic analysis of AC. Huang et al. (2002) presented a thermo-visco-plastic constitutive model that incorporated the temperature and loading rate into the Hierarchical Single Surface

(HiSS) plasticity based on a constitutive model developed by Desai and Zhang (1987).

Continuum models are powerful as they lend themselves to FE implementation to predict AC performance under boundary conditions that represent the laboratory and/or the field. However, they generally do not account for the effect of the initial distribution of the microstructure and its evolution on the macroscopic behavior of the material. There is a progressive change in the microstructure of AC during its lifetime. This is due to the influence of different micro-mechanical activities that are in play during the deformation process (Krishna and Rajagopal 2002). The microstructure evolution reflects itself in aggregate and void distribution. Recent studies on aggregate distribution in AC have shown that aggregate orientation in AC exhibit transverse anisotropy with respect to the horizontal direction (Tashman et al. 2001). Unlike their isotropic counterparts, anisotropic materials exhibit directionally dependent mechanical properties and thus the isotropic theories are inapplicable for them (Arramon et al. 2000). Therefore, anisotropy is considered to have important influence on the development of a valid numerical and analytical model for AC and on the measured mechanical properties.

Defects in the form of voids exist initially in most engineering materials and grow and propagate as the material undergoes permanent deformation. Park et al. (1996) stated that AC experiences a significant amount of microcracking under service loading, which is assumed to be the source of nonlinear behavior. Scarpas et al. (1997b) stated that with the exception of very highly confined triaxial states of compressive loading, response degradation in aggregate materials is caused predominantly by the nucleation,

localization, and eventual propagation of splitting cracks along planes perpendicular to the maximum principal tensile strain.

The ability to model the evolution of the microstructure (air voids, aggregates, as well as microcracks) within the AC mixture is critical for better prediction of performance. Recently, there have been several successful attempts to quantify the microstructure of AC mixtures in terms of aggregate distribution using imaging technology and X-Ray Computed Tomography (CT) (e.g. Masad et al. 1999a, Tashman et al. 2001). Furthermore, X-Ray CT has been used to characterize the air void distribution in AC (e.g. Masad et al. 1999a, Braz et al. 1999, Tashman et al. 2002).

The overall objective of this chapter is to develop an anisotropic viscoplastic continuum damage model for AC that links some microstructural properties to the viscoplastic deformation of the material. The model developed is still considered a continuum model and, thus, has all the advantages of such a type. At the same time it includes the effect of the microstructure in terms of the anisotropy and damage, which is usually a property of a micro-mechanistic discrete model.

THE MECHANISM OF PERMANENT DEFORMATION (RUTTING)

It is important in developing a valid constitutive model for AC rutting to have a thorough understanding of the process through which the material undergoes gradual permanent deformation that eventually leads to failure (rutting phenomenon). This understanding is necessary to develop a model that accounts for the state of stress and the mechanisms that are associated with permanent deformation.

Experimental measurements as well as numerical simulations have shown that rutting in AC takes place very close to the surface where the stress path is dominated mainly by shear stresses (Sousa and Weissman 1994). These shear stresses induce energy that is dissipated in three different mechanisms leading to permanent deformation. The first one is overcoming friction between the aggregates coated with binder. The frictional resistance in these aggregates like other granular materials is a function of the aggregate's mineralogy and roughness (e.g. Rowe 1962), and is also a function of the binder properties.

The second mechanism is overcoming interlocking between the aggregates, which is responsible for the material dilation. The increase in the mix percent air voids is a result of this dilative behavior. The amount of dilation is dependent on the confinement level, aggregate gradation, angularity, and form (flat-elongation) (e.g. Lytton et al. 1993, Sousa and Weissman 1994, Kaloush 2001). Based on laboratory and field measurements, Sousa and Weissman (1994) have pointed out that this mechanism is one of the most important aspects that should be considered in the development of a valid constitutive model for AC.

The third mechanism is the energy dissipation in overcoming the bonding between the binder elements (cohesion), and between the binder and aggregates (adhesion). This energy leads to the development of microcracks that cause the material to soften under repeated loading, leading to accelerated permanent deformation (macrocracks). Lytton (2000) has documented this phenomenon by stating: "If an AC work-hardens under repeated loads with accumulating plastic strain but does not have

microcracks arresters and does not heal rapidly, it will reach a point at which it is stiff enough for microcracks to initiate and grow. This energy that is used up with each load is then parceled out to the growth of microcracks which soften the mix, and to increasing the rate of plastic strain." The resistance of the AC to the development of microcracks depends on the binder rheological properties and aggregate chemical properties.

The interaction among the aforementioned phenomena manifests itself in work hardening and work softening. Work hardening takes place when the applied energy is sufficient to overcome the frictional and interlocking of aggregate causing the material to become stiffer due to the newly formulated microstructure trying to resist the applied load. During this process, the aggregates rotate and slip relative to each other to formulate a stiffer microstructure, causing the binder to go through some deformation, but this deformation is not high enough to overcome the cohesive and adhesive bonding. On the other hand, work softening occurs when the aggregate rotation and sliding become high enough to cause cohesive and/or adhesive failure within the microstructure resulting in microcracks. These microcracks occur in conjunction with dilation causing an increase in the material volume, and consequently, an increase in the effective stress applied at the remaining intact part of the material. This results in a decrease in the load-carrying capacity of the material.

The complexity of AC microstructure makes it difficult to fully separate the energy dissipation mechanisms. For example, it is difficult if not impossible to attribute relative aggregate sliding to either frictional properties of the aggregates, the rheological properties of the binder, or the adhesion between the aggregate and the binder. The role

of each of these mechanisms is expected to depend on the mix design (including the material characteristics) and the film thickness distribution. For a thin asphalt film, the aggregate-to-aggregate friction and interlocking can be the main mechanism in resisting permanent deformation. As the film thickness increases, the aggregate frictional and interlocking (dilation) characteristics contribution decreases, and the binder rheological properties are relied more upon to resist cohesive and adhesive failure.

The constitutive model presented in this chapter is part of an effort to relate these mechanisms or their manifestations to permanent deformation. The model is developed to account for the following phenomena:

- Shear being the dominant state of stress causing rutting;
- Viscoplastic work hardening;
- Dilation of the material;
- Pressure and strain rate dependency;
- Aggregates distribution in the microstructure;
- Damage in terms of crack initiation and nucleation and growth of voids.

For the purpose of the viscoplastic behavior, Perzyna's viscoplastic model is adopted. Drucker-Prager yield function *f* is selected in order to account for the dilative behavior of the material as well as the effect of confining pressure. The vector magnitude (Δ) is used for the purpose of describing the aggregate distribution within the microstructure, and the effective stress theory is used to capture the effect of damage. Consequently, the yield surface *f* is postulated to be a function of the following:

$$f = f(I_1, J_2, \Delta, \xi) - \kappa = 0 \tag{3-1}$$

where I_1 is first invariant of the stress tensor σ_{ij}, which accounts for the effect of confinement on the material response; J_2 is the second invariant of the deviatoric stress tensor S_{ij}, which accounts for the effect of shearing; ξ, referred to as the damage parameter, is an internal structure variable that accounts for the effect of crack initiation and nucleation and growth of voids; κ is a hardening parameter that describes the growth of the viscoplastic yield surface as the material undergoes viscoplastic deformation; and Δ, referred to as the vector magnitude, is an internal structure parameter that accounts for the effect of anisotropy of the aggregate distribution.

MICROSTRUCTURE-BASED VISCOPLASTIC MODEL FOR AC

In Perzyna's elastic/viscoplastic model, the total strain rate tensor $\dot{\varepsilon}$ is decomposed as follows:

$$\dot{\varepsilon} = \dot{\varepsilon}_e + \dot{\varepsilon}_{vp} \tag{3-2}$$

where $\dot{\varepsilon}_e$ and $\dot{\varepsilon}_{vp}$ are the elastic strain rate tensor and viscoplastic strain rate tensor, respectively, and the "dot" indicates the time derivative. The elastic strain rate follows Hooke's law and can be expressed as follows:

$$\dot{\boldsymbol{\varepsilon}}_e = \frac{1}{2G}\left[\overset{\nabla}{\boldsymbol{\sigma}} - \frac{\nu}{1+\nu} tr \overset{\nabla}{\boldsymbol{\sigma}} I\right] \tag{3-3}$$

where $\overset{\nabla}{\sigma}$ is the symmetric Zaremba-Jaumann rate of change of the Cauchy stress tensor σ; G is the shear modulus; ν is the Poisson's ratio; and I is the identity matrix.

It is assumed that the deformation of AC at relatively high temperatures is mainly viscoplastic. Thus, the elastic contribution is assumed relatively small, and only the

viscoplastic deformation is considered in this study. The viscoplastic strain rate is defined using the flow rule as follows:

$$\dot{\varepsilon}_{vp} = \Gamma \cdot < \phi(f) > \cdot \frac{\partial g}{\partial \sigma} \tag{3-4}$$

where, Γ is the fluidity parameter, which establishes the relative rate of viscoplastic strain and is experimentally determined; and $\frac{\partial g}{\partial \sigma}$ is a measure of the direction of viscoplastic strain. If $g = f$, then the associated flow rule applies, and Eq. (3-4) becomes:

$$\dot{\varepsilon}_{vp} = \Gamma \cdot < \phi(f) > \cdot \frac{\partial f}{\partial \sigma} \tag{3-5}$$

with $\phi(f)$ being the viscoplastic yield function and < > the Macauley brackets to ensure that nonpositive values of $\phi(f)$ lead to $\dot{\varepsilon}_{vp} = 0$.

A modified version of Drucker-Prager yield surface is adopted here to develop the relationship in Eq. (3-5). The conventional Drucker-Prager yield surface has the following form:

$$f = \sqrt{J_2} - \alpha I_1 - \kappa = 0 \tag{3-6}$$

Where,

$$I_1 = \sigma_{ii} \tag{3-7a}$$

$$J_2 = \frac{1}{2} S_{ij} S_{ji} \tag{3-7b}$$

σ_{ij} and S_{ij} are the stress tensor and the corresponding deviatoric tensor, respectively,

$$S_{ij} = \sigma_{ij} - \frac{1}{3} \sigma_{kk} \delta_{ij} \tag{3-8}$$

and α is a parameter that reflects the material frictional and dilation potential of the material. Thus, α influences the proportions of the volumetric and deviatoric strains. κ is a parameter that reflects the combined effect of the cohesion and frictional properties of the material.

Oda and Nakayama (1989) modified Drucker-Prager yield surface to include the effect of aggregate anisotropy. This was done by introducing a microstructure tensor $\overline{F}_{ij}$ which gives a measure of the two-dimensional anisotropy produced by the preferred orientation of nonspherical particles. In order to formulate the two-dimensional microstructure tensor $\overline{F}_{ij}$ in three-dimension, it was assumed that the inherent anisotropy exhibits axial symmetry with an axis of symmetry parallel to the direction of the applied load. The second assumption made was that the principal values in two-dimensions are assumed to be proportional to the principal values in three-dimensions. These assumptions lead to the three-dimensional microstructure tensor F_{ij} as follows:

$$\mathrm{F_{ij}} = \begin{pmatrix} (1-\Delta)/(3+\Delta) & 0 & 0 \\ 0 & (1+\Delta)/(3+\Delta) & 0 \\ 0 & 0 & (1+\Delta)/(3+\Delta) \end{pmatrix} \tag{3-9}$$

where Δ is the vector magnitude that describes the aggregate orientation distribution measured on two-dimensional images and is a function of aggregate shape properties and distribution,

$$\Delta = \frac{1}{M}\left[\sum_{k=1}^{M}(\cos 2\theta^k)^2 + \sum_{k=1}^{M}(\sin 2\theta^k)^2\right]^{\frac{1}{2}} \tag{3-10}$$

where θ^k is the inclination angle of a unit vector m^k corresponding to a k^{th} particle on a two-dimensional section of the material and ranges between –90° and +90° as shown in Fig. 3.1, and M is the total number of measurements. Theoretically, the value of Δ ranges between zero and unity. A zero value indicates the aggregates are completely randomly distributed, which is analogous to isotropic materials, and a unity value indicates the aggregates are all oriented in one direction.

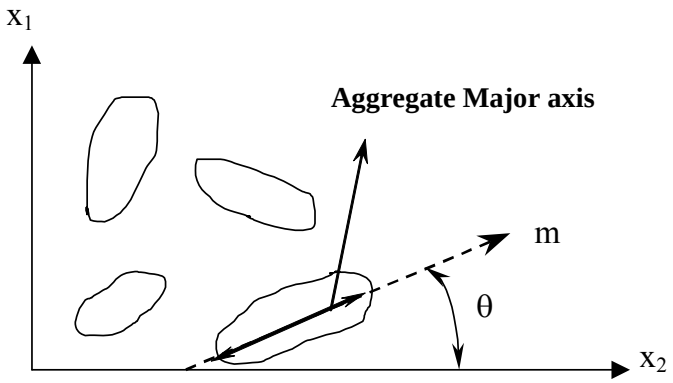

Fig. 3.1. Two-Dimensional Particles Orientation in a Vertical Section

Oda and Nakayama (1989) incorporated the microstructure tensor F_{ij} in Drucker-Prager yield function by modifying I_1 and J_2 to become $\bar{I}_1$ and $\bar{J}_2$, respectively, such that:

$$\bar{I}_1 = \left(a_1\delta_{ij} + a_2 F_{ij}\right)\sigma_{ij} \tag{3-11a}$$

$$\bar{J}_2 = \left(2b_6\delta_{ik}\delta_{jl} + 4b_7 F_{ik}\delta_{lj}\right)S_{ij}S_{kl} \tag{3-11b}$$

where,

$$a_1 = 1 - \lambda(2D_2)^{1/2} \tag{3-12a}$$

$$a_2 = 3\lambda(2D_2)^{1/2} \tag{3-12b}$$

$$b_6 = \frac{1}{4} - \frac{\mu}{2}(2D_2)^{1/2} \tag{3-13a}$$

$$b_7 = \frac{3}{4}\mu(2D_2)^{1/2} \tag{3-13b}$$

$$D_2 = \frac{4\Delta^2}{3(3+\Delta)^2} \tag{3-14}$$

where μ and λ are anisotropy material constants that are experimentally determined; and D_2 is the second invariant of the deviatoric microstructure tensor F'_{ij} defined as follows:

$$F'_{ij} = F_{ij} - \frac{1}{3}F_{kk}\delta_{ij} \tag{3-15}$$

where δ is the Kronecker δ.

The effective stress theory introduced by Kachanov (1958) is used to capture the effect of damage in terms of crack initiation and nucleation and growth of voids (e.g. Murakami 1983, Zbib and Aifantis 1986, Chaboche 1988). The damage parameter ξ is expressed in terms of the ratio of area of voids A_v to the total cross sectional area S, thus:

$$\xi = \frac{A_v}{S} \tag{3-16a}$$

$$S = A_v + A_s \tag{3-16b}$$

$$\sigma_e = \frac{Load}{A_s} = \frac{P}{S}\cdot\frac{S}{A_s} = \sigma\cdot\frac{S}{(S-A_v)} = \frac{\sigma}{1-\xi} \quad , \text{ where } 0 \le \xi \le 1 \tag{3-17}$$

where A_s is the solid phase area, which includes the aggregate and asphalt binder; σ_e is the effective stress that causes the deformation in the specimen; and P is the applied axial load. Substituting σ_e and S_e for σ and S in Eq. (3-11), the modified $\bar{I}_1$ and $\bar{J}_2$ become the modified effective ones, namely, $\bar{I}_1^e$ and $\bar{J}_2^e$, respectively, where,

$$\bar{I}_1^e = \frac{\bar{I}_1}{1-\xi} \tag{3-18a}$$

$$\bar{J}_2^e = \frac{\bar{J}_2}{(1-\xi)^2} \tag{3-18b}$$

and the yield function in Eq. (3-6) is now modified to become:

$$f = \sqrt{\bar{J}_2^e} - \alpha \bar{I}_1^e - \kappa = 0 \tag{3-19}$$

Upon substituting Eq. (3-19) into $<\phi(f)>$, and assuming a power law function for the viscoplastic yield function, we get:

$$<\phi(f)> = \begin{Bmatrix} 0, \textit{No Viscoplastic Strain} & \sqrt{\bar{J}_2^e} - \alpha \bar{I}_1^e - \kappa \le 0 \\ \left[\sqrt{\bar{J}_2^e} - \alpha \bar{I}_1^e - \kappa\right]^N, \textit{Viscoplastic Strain Occurs} & \sqrt{\bar{J}_2^e} - \alpha \bar{I}_1^e - \kappa > 0 \end{Bmatrix} \tag{3-20}$$

where the exponent N is a constant to be determined experimentally and κ is, as defined earlier, the hardening parameter which describes the growth of the yield surface. In a given stress increment, when as a result of hardening, the condition $\phi(f) \le 0$ is fulfilled, the viscoplastic flow ceases and κ stops growing. It is only after the application of the next load increment that the overstress becomes positive ($\phi(f) > 0$), and hence viscoplastic flow occurs again. The interaction among all the model parameters in Eq. (3-20) should exceed the hardening parameter for viscoplastic deformation to take place.

The derivative of the yield function with respect to stress gives the direction of the strain increment, which is normal to the yield surface for the associated flow rule, as follows:

$$\frac{\partial f}{\partial \sigma_{ij}} = \frac{1}{1-\xi}\left[\frac{S_{ij}}{2\sqrt{\bar{J}_2}} + \frac{2b_7}{\sqrt{\bar{J}_2}}\left(F'_{im}S_{mj} + F'_{ik}S_{kj} - \frac{2}{3}F'_{km}S_{mk}\delta_{ij}\right) - \alpha\left(\delta_{ij} + a_2 F'_{ij}\right)\right] \qquad (3\text{-}21)$$

where α, κ, Δ, and ξ are assumed to be independent of the stress. Eq. (3-21) shows that the direction of the viscoplastic strain rate is dependent on the microstructure parameters, namely, the anisotropy parameters (Δ, λ, μ) and the damage parameter (ξ). Substituting Eqs. (3-20, 3-21) into Eq. (3-5), the viscoplastic strain rate can now be calculated.

EFFECTIVE STRESS AND EFFECTIVE STRAIN

For the work hardening theory of viscoplasticity to be of any practical use, the hardening parameters in the loading function should be related to the experimental uniaxial stress-strain curve. Therefore, the so-called effective stress and the effective strain are used (Chen and Han 1988). The single effective stress-effective strain curve should preferably be reduced to a uniaxial stress-strain curve; the uniaxial compression test in this study.

Effective Stress

Since the loading function, $f(\sigma_{ij}, \varepsilon_{ij}^{vp}, \kappa) = 0$ by definition, determines whether additional viscoplastic flow takes place or not and is also a positively increasing function, it can be used as a stress variable to define the effective stress (Chen and Han 1988).

In the case of isotropic hardening, the loading function takes the following form:

$$f(\sigma_{ij},\kappa) = F(\sigma_{ij}) - \kappa(\varepsilon_{vp}) = 0 \tag{3-22}$$

The function $F(\sigma_{ij})$ is used to define the effective stress, which should reduce to the stress σ_{11} in the uniaxial compression test. It follows that the loading function $F(\sigma_{ij})$ must be some constant C times the effective stress σ_{eff} to some power n,

$$F(\sigma_{ij}) = C\sigma_{eff}^{n} \tag{3-23}$$

Thus,

$$\sqrt{\bar{J}_2^e} - \alpha\bar{I}_1^e = \kappa = C\sigma_{eff}^{n} \tag{3-24}$$

In the uniaxial compression test, $\bar{I}_1^e$ and $\bar{J}_2^e$ reduce to the following:

$$\bar{I}_1^e = \frac{\sigma_{eff}}{1-\xi}(1-Y) \tag{3-25a}$$

$$\sqrt{\bar{J}_2^e} = \frac{\sigma_{eff}}{1-\xi}\sqrt{X} \tag{3-25b}$$

where,

$$X = \frac{1}{3} - \frac{4}{9}\sqrt{24}\mu\left(\frac{\Delta}{3+\Delta}\right)^2 \tag{3-26a}$$

$$Y = \frac{4}{3}\sqrt{24}\lambda\left(\frac{\Delta}{3+\Delta}\right)^2 \tag{3-26b}$$

substituting Eq. (3-25) in Eq. (3-24) gives:

$$C = \frac{\sqrt{X} - \alpha(1-Y)}{1-\xi} \tag{3-27a}$$

$$n = 1 \tag{3-27b}$$

and therefore,

$$\sigma_{eff} = \frac{(1-\xi)\left(\sqrt{\bar{J}_2^e} - \alpha \bar{I}_1^e\right)}{\sqrt{X} - \alpha(1-Y)} = \frac{\left(\sqrt{\bar{J}_2} - \alpha \bar{I}_1\right)}{\sqrt{X} - \alpha(1-Y)} \tag{3-28}$$

Effective Strain

Two methods are generally used in defining the effective viscoplastic strain. One defines the effective viscoplastic strain increment intuitively as some simple combination of viscoplastic strain increments, which is always positive and increasing (Chen and Han 1988). The simplest combination of this type takes the form $d\bar{\varepsilon}_{vp} = C\sqrt{d\varepsilon_{ij}^{vp} d\varepsilon_{ij}^{vp}}$. The second method, which is adopted in this study, defines the effective viscoplastic strain increment in terms of the viscoplastic work per unit volume in the form (Chen and Han 1988):

$$dW_{vp} = \sigma_{eff} d\bar{\varepsilon}_{vp} \tag{3-29}$$

From Eq. (3-5),

$$\dot{W}_{vp} = \sigma_{ij} \dot{\varepsilon}_{ij}^{vp} = \Gamma < \phi(f) > \sigma_{ij} \frac{\partial f}{\partial \sigma_{ij}} = \Gamma < \phi(f) > \sigma_{ij} \frac{\partial F}{\partial \sigma_{ij}} = \sigma_{eff} \dot{\bar{\varepsilon}}_{vp} \tag{3-30}$$

If F is homogenous of degree n in the stress, then,

$$\dot{W}_{vp} = \Gamma < \phi(f) > nF \tag{3-31}$$

Also from Eq. (3-5), one gets,

$$\Gamma < \phi(f) >= \frac{\sqrt{\dot{\varepsilon}_{ij}^{vp} \dot{\varepsilon}_{ij}^{vp}}}{\sqrt{\frac{\partial f}{\partial \sigma_{ij}} \frac{\partial f}{\partial \sigma_{ij}}}} \tag{3-32}$$

Substituting Eqs. (3-27, 3-28, 3-31, 3-32) into Eq. (3-30) gives:

$$\dot{\bar{\varepsilon}}_{vp} = \frac{\left[\sqrt{X} - \alpha(1-Y)\right]\sqrt{\dot{\varepsilon}_{ij}^{vp}\dot{\varepsilon}_{ij}^{vp}}}{(1-\xi)\sqrt{\frac{\partial f}{\partial \sigma_{ij}}\frac{\partial f}{\partial \sigma_{ij}}}} \tag{3-33}$$

For the case of uniaxial compression, substituting Eqs. (3-12, 3-13, 3-14, 3-15, 3-18, 3-25, 3-26) into Eq. (3-21) yields:

$$\frac{\partial f}{\partial \sigma_{11}} = \frac{\sqrt{X} - \alpha(1-Y)}{(1-\xi)} \tag{3-34a}$$

$$\frac{\partial f}{\partial \sigma_{22}} = \frac{\partial f}{\partial \sigma_{33}} = \frac{1}{(1-\xi)}\left[\frac{-\sqrt{X}}{2} - \alpha\left(1+\frac{Y}{2}\right)\right] \tag{3-34b}$$

0: otherwise (3-34c)

Therefore, to match the uniaxial compression test, Eq. (3-33) becomes,

$$\dot{\bar{\varepsilon}}_{vp} = \frac{\left[\sqrt{X} - \alpha(1-Y)\right]}{\sqrt{\frac{3}{2}X + 3\alpha Y\sqrt{X} + 3\alpha^2 + \frac{3}{2}\alpha^2 Y^2}}\sqrt{\dot{\varepsilon}_{ij}^{vp}\dot{\varepsilon}_{ij}^{vp}} \tag{3-35}$$

For a triaxial loading setup, the effective viscoplastic strain rate in Eq. (3-35) reduces to the following form:

$$\dot{\bar{\varepsilon}}_{vp} = \Gamma\left[\sqrt{\bar{J}_2^e} - \alpha\bar{I}_1^e - \kappa\right]^N \cdot \frac{\sqrt{X} - \alpha(1-Y)}{1-\xi} = \dot{\varepsilon}_{11}^{vp} \tag{3-36}$$

and the effective viscoplastic strain would be the integration of Eq. (3-36) over time.

EVOLUTION LAWS FOR MODEL PARAMETERS

Hardening Parameter (κ)

The material hardening during loading can be captured by the evolution of α, κ, or both. The evolution of α is the result of changes in the aggregate structure associated with friction and dilation. Thus a change in α is manifested by a change in the anisotropy parameters (Δ, λ, and μ). The evolution of κ is associated with hardening due to the deformation in the binder that causes changes in the mobilized cohesion and adhesion to aggregates and the change in the frictional properties of the aggregate structure. Tan et al. (1994) used a plasticity model based on Drucker-Prager yield criterion and concluded that the friction angle for a well compacted AC is primarily a function of aggregate contact friction and interlocking which are insensitive to test temperature and strain rates. On the other hand, the cohesion of the material was shown to be a function of the test temperatures and strain rates, being dependent on the binder and fines mixture properties. The following evolution law for the isotropic hardening parameter κ is proposed in this chapter:

$$\dot{\kappa} = H\dot{\bar{\varepsilon}}_{vp} \tag{3-37}$$

where, H is the isotropic hardening coefficient. H is also postulated to be a power function of the effective viscoplastic strain:

$$H = h\left(\bar{\varepsilon}_{vp}\right)^{\beta} \tag{3-38}$$

Solving the differential equation (3-37), the hardening parameter κ can be written as follows:

$$\kappa = \kappa_o + \frac{h}{\beta + 1}\left[\left(\bar{\varepsilon}_{vp}\right)^{\beta+1} - \left(\bar{\varepsilon}_{vp}^{o}\right)^{\beta+1}\right] \tag{3-39}$$

where $\bar{\varepsilon}_{vp}^{o}$ is initial effective viscoplastic strain (zero in a monotonic triaxial strength and creep test) and κ_o defines the initial yield surface. κ_o, h, and β are material constants to be determined experimentally. The evolution function in Eq. (3-39) is determined from triaxial creep and/or strength testing of AC.

Aggregate Anisotropy Parameter (Δ)

The anisotropy parameter, vector magnitude (Δ), describes the distribution of the aggregate orientation in the mix. The initial value of the vector magnitude (inherent anisotropy) depends on the aggregate characteristics, aggregate gradation, and the compaction method used to prepare the specimen (Masad et al. 1999a, Masad et al. 1999b, Tashman et al. 2001). Dessouky et al. (2003) presented experimental results showing that the initial value and the evolution of the vector magnitude are functions of aggregate shape and gradation. Since the mix compaction is conducted at a temperature that achieves a specified binder viscosity, the binder type does not significantly affect the value of the vector magnitude during compaction. The induced anisotropy caused by the applied stress is reflected in the changes of the vector magnitude. The effect of the initial value of Δ and its evolution on the behavior of asphalt is discussed in this chapter. However, due to lack of data available at this point relating Δ to permanent strain, the induced anisotropy is not considered when the model is compared to experimental data. The vector magnitude is

measured using Image Analysis Techniques (IAT) of AC cut sections (Tashman et al. 2001).

Damage Parameter (ξ)

One of the most recognized evolution laws for damage was recommended by Perzyna (1984) based on experimental measurements and analytical solutions of void growth in a plastic medium. Perzyna (1984) proposed three mechanisms that drive damage in ductile materials, namely, nucleation of voids, growth of voids, and transport due to vacancy diffusion. Physical considerations suggest that the rate of nucleation of voids is connected with the inelastic energy and with the first invariant of the stress tensor. Similarly, the growth rate of voids during the inelastic flow process is mainly associated with the inelastic strain rate. The growth term proposed by Perzyna (1984) can be obtained analytically by deriving the rate of growth of a void in a plastic medium.

In this chapter, it was decided to adopt the notion, similar to Perzyna's analysis of damage, that the rate of damage is a function of the rate of viscoplastic energy, confining pressure, and effective viscoplastic strain as follows:

$$\dot{\xi} = f(\dot{W}_{vp}, \dot{I}_1, \dot{\bar{\varepsilon}}_{vp}) \tag{3-40}$$

where $\dot{W}_{vp}$ is the rate of viscoplastic energy; $\dot{I}_1$ is the rate of change in the first stress invariant; and $\dot{\bar{\varepsilon}}_{vp}$ is, as defined previously, the effective viscoplastic strain rate. However, the form of the above relationship is not expected to follow that proposed by Perzyna who showed that damage in metals grows at a small rate at the beginning of the deformation

process until it reaches a critical value, which corresponds to a sudden loss in the material yield strength. Damage in AC, represented by the increase in voids, is due to dilation and due to the cohesive and adhesive failure in the binder and binder-aggregate interface. As such, it is expected that confinement, which affects dilation, will play a major role in controlling void nucleation. Also, void growth in an AC is expected to be quite different than that in metals. The void growth in the asphalt binder is controlled by the surrounding medium of aggregates, which act as elastic walls against void growth. This makes the growth mechanism far from being described by a void in a plastic medium. Based on this discussion, an empirical power law function is proposed at this point to represent the relationship in Eq. (3-40) as follows:

$$\xi = \xi(W_{vp}, I_1, \bar{\varepsilon}_{vp}) = \xi_o + Hc\left(W_{vp}\right)^{Hp} + Lc\left(I_1\right)^{Lp} + Ec\left(\bar{\varepsilon}_{vp}\right)^{Ep} \tag{3-41}$$

where, ξ_o is the initial damage value; W_{vp} is the viscoplastic energy; I_1 is the first invariant of the stress tensor; $\bar{\varepsilon}_{vp}$ is the effective viscoplastic strain; and *Hc*, *Hp*, *Lc*, *Lp*, *Ec*, and *Ep* are fitting coefficients. Conceptually, it is expected that both W_{vp} and $\bar{\varepsilon}_{vp}$ cause an increase in the damage within the microstructure of the material, while I_1 has the opposite effect. In equation (3-41), the second and third terms on the right-hand-side of the equation can be interpreted as the nucleation function, and the last term is the growth function.

PARAMETRIC EVALUATION OF THE MODEL RESPONSE

A parametric evaluation was conducted to investigate the effect of some parameters on the model's response. Fig. 3.2 shows the effect of the initial state of anisotropy captured

by the vector magnitude (Δ) on the viscoplastic deformation of AC. Fig. 3.2 clearly shows that Δ, which represents the aggregate orientation distribution, affects the material response. Fig. 3.2(a) shows that the material state of stress changes as Δ changes although the same stress is applied in the three cases. A higher value of Δ, i.e., a more preferred orientation of aggregates towards the horizontal (higher anisotropy), produces a stiffer material. This is noticed for the case of Δ=0.35 which yielded higher $\bar{I}_1$ and lower $\sqrt{\bar{J}_2}$ values. In other words, a higher value of Δ seems to act as an additional confining pressure that makes the material stronger. This is reflected in Fig. 3.2(b), where a higher Δ produces less viscoplastic strain. Fig. 3.3 shows the effect of the anisotropy on the predicted strength value of ALF test section number 5. The axial strength increased with an increase in the material anisotropy.

A possible explanation for this behavior is that when the axial load is applied to the specimen, the stress is transmitted throughout the specimen, which tends to resist it. Part of the resistance comes from the contact between the aggregates, which would be in different directions depending on the orientation of the aggregates. In a static condition, the summation of forces in the axial direction is zero. Consequently, the summation of the axial components of the normal to contacts between the aggregate should be equal to the applied axial load. As the vector magnitude increases, the aggregates tend to orient themselves horizontally and by doing so, the direction of the normal to contacts between the aggregates tends to come closer to the axial direction resulting in an increase in the resistance of the material.

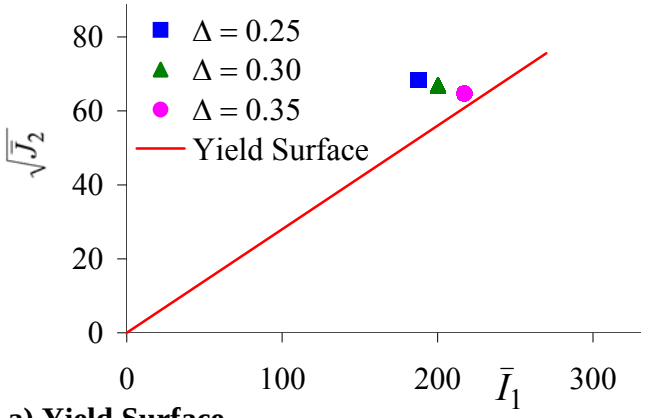

a) Yield Surface

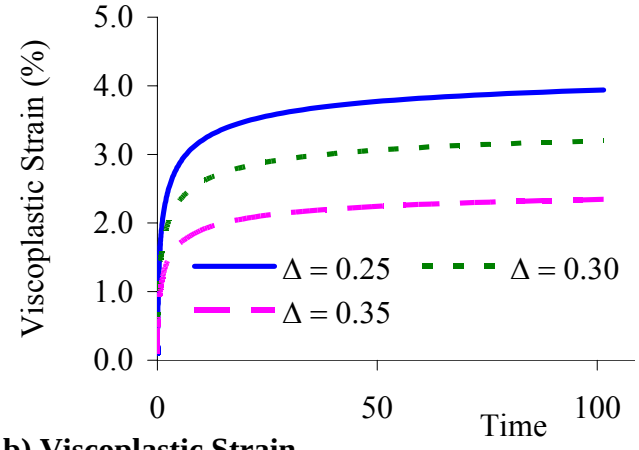

b) Viscoplastic Strain

Fig. 3.2. Model Prediction of the Effect of Anisotropy (Δ) on the Viscoplastic Deformation of AC for ALF Test Section Number 5

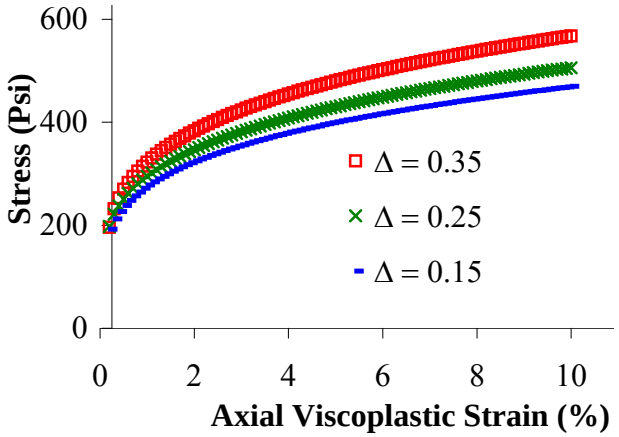

Fig. 3.3. Effect of Anisotropy on the Strength of AC for ALF Test Section Number 5 (σ_3 = 60-psi)

Fig. 3.4 shows the effect of the strain rate on the predicted strength values of AC for ALF test section number 5. As expected from a strain rate dependent material like AC, the higher the strain rate, the stiffer the material.

Fig. 3.5 shows how the damage parameter is predicted to evolve as the material plastically deforms. As previously mentioned, it is been assumed that there is less damage at higher confining pressure at the same strain value. This is illustrated in Fig. 3.5 where the higher the confining pressure, the lower the damage value. It is noteworthy that damage in AC as postulated by Eq. (3-41) evolves in a different pattern than postulated by Perzyna for metals. Perzyna (1984) has shown that damage in metals takes an exponential pattern where the damage rate increases rapidly with deformation resulting in a sudden failure in the specimen. Fig. 3.5, on the other hand, suggests that damage in AC increases at a milder rate resulting in a gradual loss in the material strength. However, the curve for the unconfined specimen takes a different pattern, as it shows rapid increase in damage compared with the confined tests.

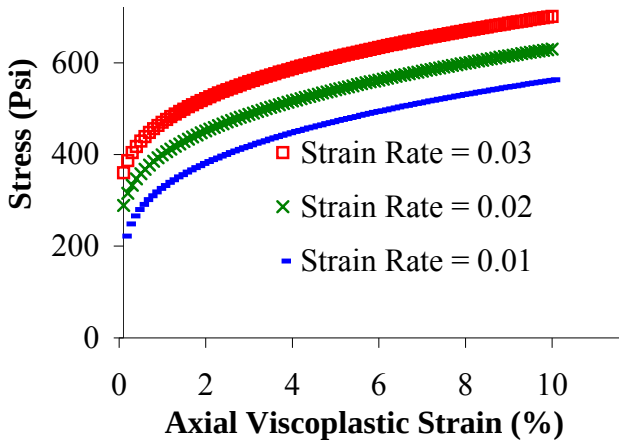

Fig. 3.4. Effect of Strain Rate on the Strength of AC for Test Section Number 5 (σ_3 = 60-psi)

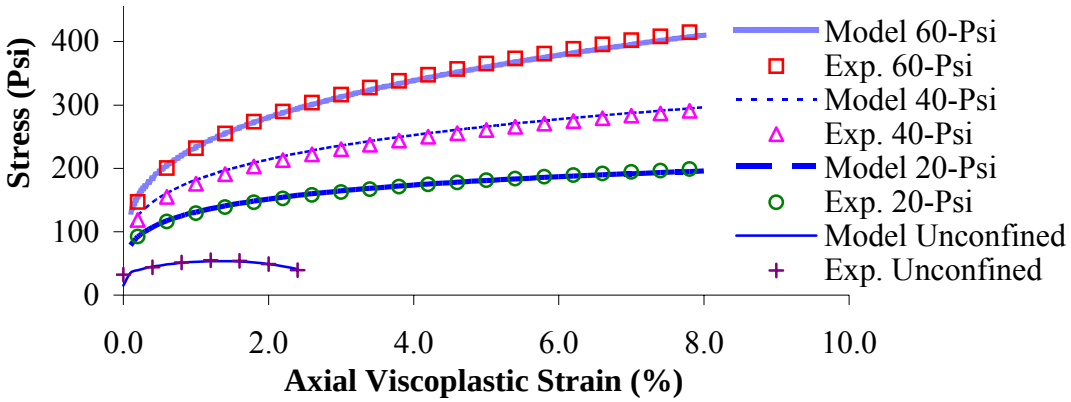

a) Triaxial strength tests

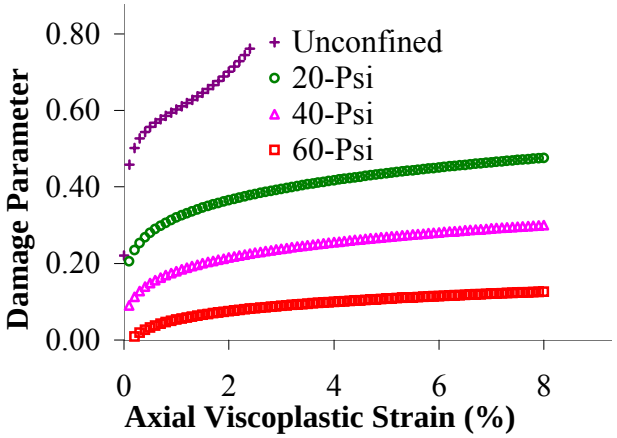

b) Damage parameter as a function of axial strain

Fig. 3.5. Evolution of Damage Parameter for ALF Test Section Number 9

Table 3.1. Average Section AC Mixture Properties for ALF Test Sections

ALF Lane	Binder Type	Nominal Size (mm)	Asphalt Content (%)	Air Void Content (%)
5	AC-10	19.0	4.80	8.6
9	AC-5	19.0	4.90	7.7
10	AC-20	19.0	4.90	9.3

EXPERIMENTAL MEASUREMENTS

Experimental measurements were used to obtain some of the model parameters and demonstrate the potential of the model in capturing the behavior of AC under different loading conditions. The details of these experimental measurements can be found in Kaloush (2001). A brief description of the materials and tests is given in this section. The mixes were obtained from a large-scale experiment conducted at the FHWA ALF. This experiment included laboratory and large scale testing of the rutting and fatigue potential of mixes with the same aggregate gradation, but different binder types. The laboratory experimental data from test section numbers 5, 9, and 10 were used for the purpose of this chapter. The other test sections were not included due to the lack of enough experimental data to determine the model parameters.

Three triaxial strength tests at different confining pressure and one triaxial confined static creep test were used in determining the model parameters and the fitting coefficients. Both strength and creep tests were conducted at a temperature of 130 ^{o}F. The test specimens were gyratory compacted to duplicate the measured original in-situ material compositions for each test section. Table 3.1 shows the average in situ properties for each lane section. All mixtures were designed using the SHRP Level 1 (Volumetric) mix design method. All specimens were prepared according to the Test Protocol UMD 9808, "Method for Preparation of Triaxial Specimens" – prepared by the Superpave Models Team. Test specimens were cylindrical specimens, 100-mm (4-inches) in diameter and 150-mm (6-inches) in height, cored from the center of the Gyratory compacted specimen. Approximately 5-mm were sawed from each test

specimen end.

Three confining pressures were used in the triaxial strength tests: 20, 40, and 60-psi. The specimens were loaded axially to failure at the selected constant confining pressure and at a displacement rate of 0.81%/min. In addition, one static creep test was conducted at an axial stress of 140-psi with a 20-psi confining pressure. A static constant load was applied until tertiary flow occurred.

Initial attempts were made to determine the model parameters based on analyzing the unconfined and confined tests. However, it was found that the unconfined test exhibits very low strength and strain values at failure significantly different from any of the confined tests. Therefore, it was decided to adopt the confined tests. This decision was also motivated by experimental observation on the high variability and low reliability of the unconfined test results (Kaloush 2001).

The vector magnitude was measured using IAT developed by Tashman et al. (2001). In this method, gyratory specimens were cut into three sections using a diamond saw and images of the cut sections were captured using a digital camera. The digital images were processed using the developed IAT that determined the vector magnitude of the AC cut sections.

Saadeh (2002) reported the vector magnitude value of the ALF mixes to be 0.362. This value is consistent with values measured on other mixes. Tashman et al. (2001) reported that typical values of vector magnitude (Δ) in AC range between 0.3 and 0.5 in vertical cut sections (parallel to the applied load) and less than 0.1 on horizontal sections (perpendicular to the applied load). This is in agreement with the assumption made by Oda

and Nakayama (1989) to formulate the three-dimensional microstructure tensor from the two-dimensional one.

Fig. 3.6 shows the volumetric change in the AC specimens under creep testing as a function of the axial strain. The volumetric change is defined as the summation of the principal strains where a negative sign indicates dilation. It is clearly shown that AC experiences dilative behavior.

Both triaxial strength and static creep tests were used for the purpose of determining the model parameters and the fitting coefficients. The vector magnitude was assumed to be 0.362 (Saadeh 2002). The remaining anisotropy parameters (λ and μ), in addition to α, Γ, N, and the corresponding hardening parameters in Eq. (3-39) were determined by curve fitting the static creep test up to the point of flow time, at which the material damage accelerates. Γ and N are material constants that need to be determined from tests in which the strain rate is varied. Since the strength tests were all conducted at one strain rate, it was decided to determine Γ and N from the creep test where the strain rate varies with time. The fitting was conducted under the restriction that the Plastic Strain Rate Ratio (PSRR) should be equal to the experimentally measured value:

$$Plastic\ Strain\ Rate\ Ratio = \frac{-\dot{\varepsilon}_{33}}{\dot{\varepsilon}_{11}} = \frac{-\left(\frac{\partial f}{\partial \sigma_{33}}\right)}{\left(\frac{\partial f}{\partial \sigma_{11}}\right)} = \frac{\left(\frac{\sqrt{X}}{2} + \alpha(1+\frac{Y}{2})\right)}{\left(\sqrt{X} - \alpha(1-Y)\right)} \tag{3-42}$$

Eq. (3-42) shows that the PSRR is a function of the anisotropy parameters namely, Δ, λ, and μ, as well as α. Both the axial and radial strain rates are needed, which were only available in the creep test. Fig. 3.7 shows that the PSRR for ALF test section number 10

increases from 0.6 to 0.8 on an average trend. In all the mixes studied, it was found that there exists a very high noise in the PSRR at relatively small strain values. For the sake of simplicity, the PSRR is assumed to be constant with any value ranging between 0.60 and 0.80. In other words, Eq. (3-36) is fitted to the creep test by the method of error minimization such that the PSRR has any constant value between 0.60 and 0.80. Fig. 3.8 shows the curve fitting for the creep test.

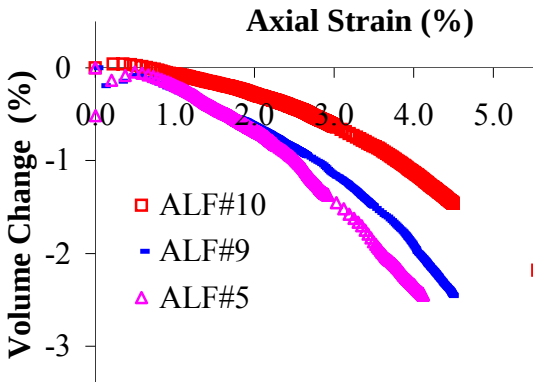

Fig. 3.6. Volume Change (Dilatancy) in ALF Test Section Numbers 5, 9, and 10. (Volume Change = $\varepsilon_{axial} + 2\times\varepsilon_{radial}$, where the Radial Strain Has a Negative Sign)

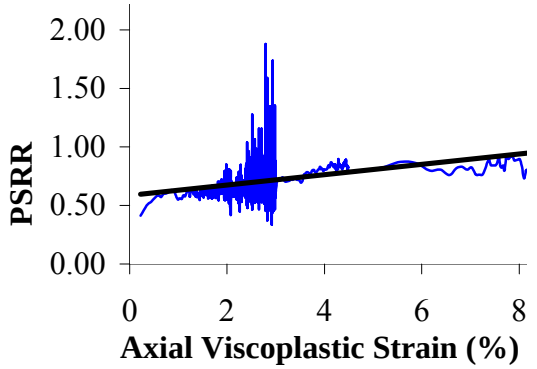

Fig. 3.7. Plastic Strain Rate Ratio as a Function of the Axial Strain for ALF Test Section Number 10 (140-psi Axial Stress, 20-psi Confinement)

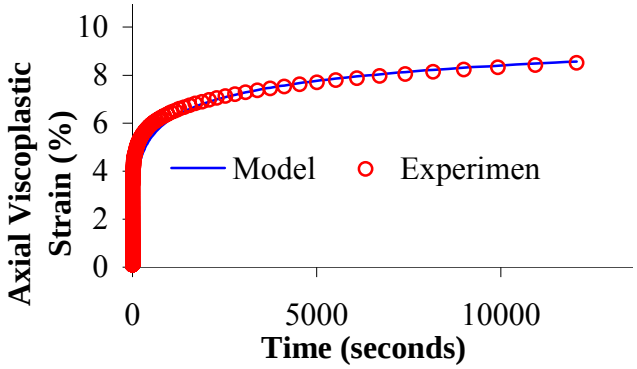

Fig. 3.8. Matching the Static Creep Test for ALF Text Section Number 10 to Determine λ, μ, α, Γ, N, κ_o, h, and β

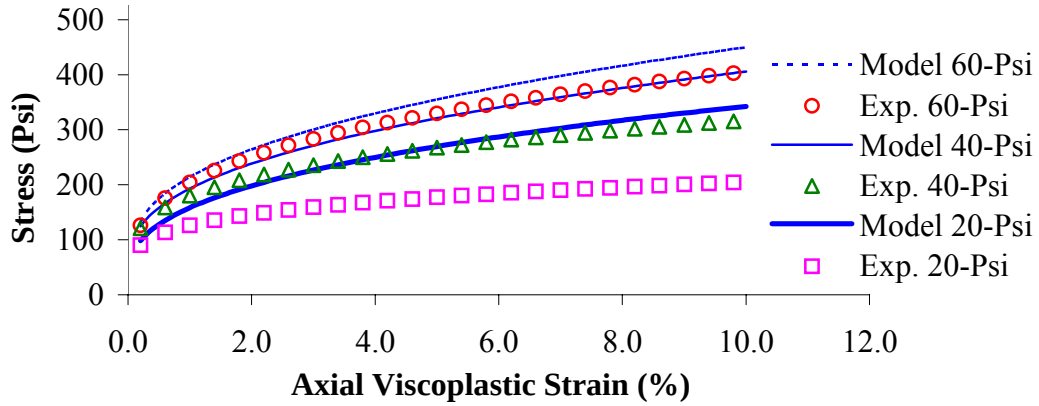

Fig. 3.9. Determining the Hardening Parameter Coefficients by Matching the 60-psi Curve between 0.2% and 2.2% for ALF Text Section Number 10

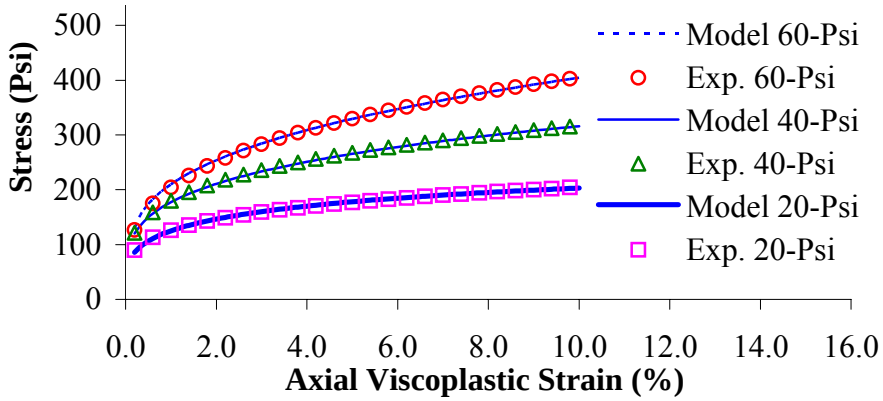

Fig. 3.10. Experimental and Model Stress-Strain Relations for ALF Text Section Number 10

The hardening parameter determined from fitting the model to the creep test was treated as an initial guess, since damage prior to the flow time was not included in the fit. Consequently, the triaxial strength tests were used to determine the corrected hardening parameter and the corresponding damage parameter. It is assumed that cracks do not significantly initiate and grow at the beginning of the viscoplastic deformation. In addition, it is assumed that the higher the confining pressure the less damage at the same strain value. This behavior is expected since the confining pressure is expected to reduce dilation and slow damage nucleation. Therefore, the 60-psi curve was fitted from 0.2% to 2.2% strain to determine the hardening parameter before the damage parameter had evolved as shown in Fig. 3.9. Eq. (3-36) is rearranged for the purpose of matching the triaxial strength test as follows:

$$\sigma_{11} = \frac{1}{\dfrac{\partial f}{\partial \sigma_{11}}} \cdot \left[\left(\frac{\dot{\varepsilon}_{11}^{vp}}{\Gamma \dfrac{\partial f}{\partial \sigma_{11}}} \right)^{1/N} + \kappa - 2\sigma_{33} \frac{\partial f}{\partial \sigma_{33}} \right] \tag{3-43}$$

where, κ, ξ, $\dfrac{\partial f}{\partial \sigma_{11}}$, and $\dfrac{\partial f}{\partial \sigma_{33}}$ are as defined in Eqs. (3-39, 3-41, 3-34a, 3-34b), respectively. It was decided not to fit the curve from 0% to 0.2% strain value because of the high variability in the experimental data at the beginning of the test. Using the corrected hardening parameter, the three triaxial strength tests were fitted simultaneously to determine the damage parameter coefficients. Fig. 3.10 shows that the model has a good match to the experimental data.

The final step was to go back to the creep test and use the hardening parameter coefficients determined from the strength tests as well as the damage parameter coefficients in order to simulate the creep test. However, the creep test is considered significantly different from the strength test because of the high strain rate values at the very beginning of the tests (higher than 50%/min). In addition the strain rate value decreases tremendously throughout the test (might reach a zero value toward the end of the test), whereas it is constant throughout the strength test (0.81%/min). Therefore, at this point, it was assumed that the damage mechanism in the creep test is different than in the strength test and different damage parameter coefficients need to be determined for the creep tests.

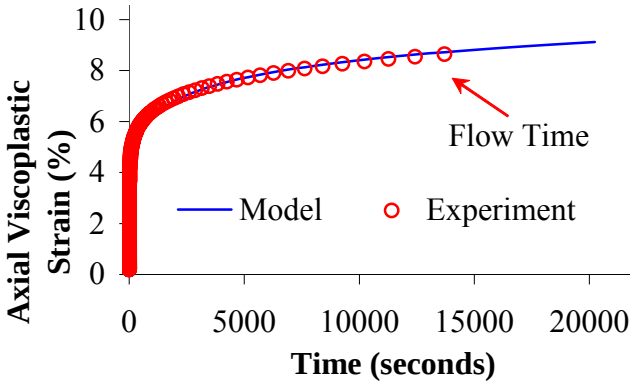

Fig. 3.11. Experimental and Model Strain-Time Relation for ALF Text Section Number 10

Fig. 3.11 shows the model has a fairly good match to the experimental creep test data using the newly determined damage coefficients. It should be noted that the flow time has been recorded to be 13590-seconds for the specimen in Fig. 3.11. There was no data recorded for the tertiary creep zone in order to avoid damaging the LVDTs (Linear Variable Differential Transformer); thus the experimental tertiary creep pattern is unknown for the ALF data. However, the model is predicting an increase in the strain rate after the flow time, which is consistent with many experimental observations. This was more obvious in ALF test section numbers 5 and 9 as will be shown subsequently.

Similarly, the model parameters and fitting coefficients for test section numbers 5 and 9 are determined and the results are plotted in Figs. 3.12 and 3.13. An example of the model parameters and the fitting coefficients is given in Table 3.2 for test section number 9. Figs. 3.10, 3.11, 3.12, and 3.13 show that the model has a good match to the experimental data. Figs. 3.11, 3.12(b), and 3.13(b) all show that the model is predicting an increase in the strain rate at the recorded axial flow time for the creep tests. This is in consistence with the experimental observation; however, because there was no data recording for the tertiary creep zone, the actual tertiary creep pattern is unknown. This is to be considered in future work, where the damage parameter can also be fitted to the tertiary creep zone in order to accurately determine its coefficients.

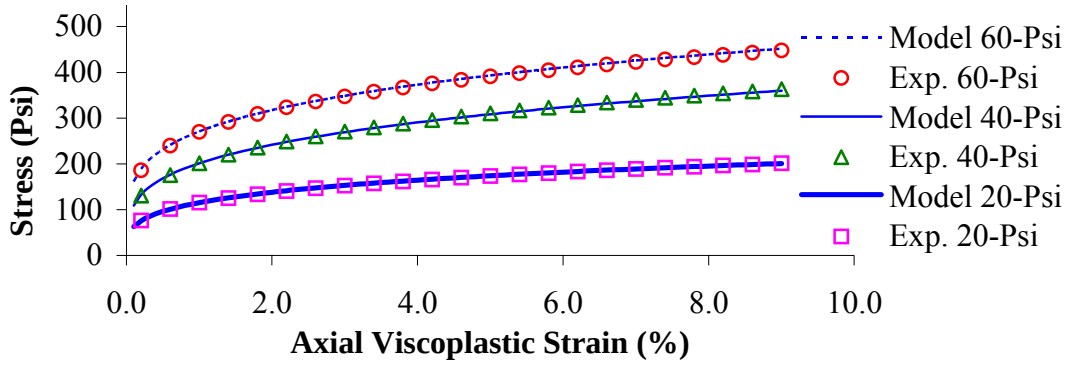

a) Triaxial strength test

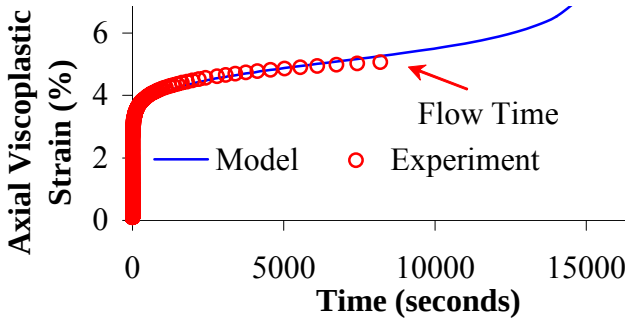

b) Triaxial static creep test

Fig. 3.12. Experimental and Model Comparison for ALF Test Section Number 5

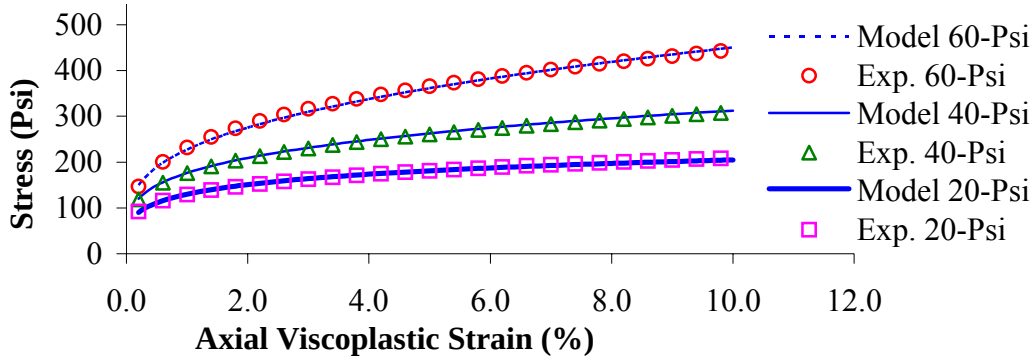

a) Triaxial strength test

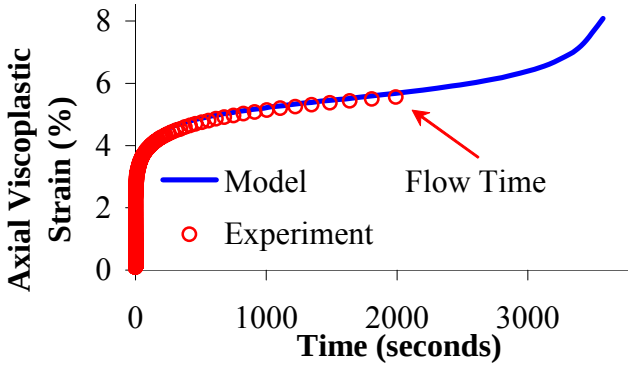

b) Triaxial static creep test

Fig. 3.13. Experimental and Model Comparison for ALF Test Section Number 9

Table 3.2. Summary of the Model Parameters and Fitting Coefficients Determined from the Static Creep and Triaxial Strength Tests for ALF Test Section Number 9

Material Constant	Value	Parameter	Determination Method	Remarks
Γ	8.593E-03	Viscoplasticity	Creep Test	Test need to capture strain rate effect
N	2.0		Creep Test	
Δ	0.362	Anisotropy	IAT	Plastic Ratio condition has to be satisfied. 0.60 <PR < 0.80 For this material, PR= 0.6015
μ	0.706		Creep Test	
λ	-3.501		Creep Test	
α	0.035	Drucker-Prager	Creep Test	
κ_o	-5.334E-03	Hardening	Strength Test	60-psi curve is fitted from 0.2%-2.2%
h	6.465		Strength Test	
β	-0.715		Strength Test	
	Strength/Creep			
ξo	0.00/0.0008	Damage	Strength/Creep Test	Damage mechanism in the strength test is assumed to be different than in the creep test
Hc	0.17/0.026		Strength/Creep Test	
Hp	-0.921/-0.021		Strength/Creep Test	
Lc	-3.174E-3/ -1.024		Strength/Creep Test	
Lp	0.865/0.118		Strength/Creep Test	
Ec	0.592/2.251		Strength/Creep Test	
Ep	0.165/0.049		Strength/Creep Test	

It should be noted that the model was unable to capture the tertiary creep without the damage parameter as shown in Fig. 3.8 for ALF test section number 10, in which the creep test is fitted with no damage. Including the damage parameter enabled capturing the tertiary creep pattern as shown in Figs. 3.11, 3.12(b), and 3.13(b). As previously discussed, the damage in the material is driven by the initiation of cracks and nucleation and growth of voids. Consequently, the damage parameter was postulated to be a power law function of the viscoplastic energy, the first invariant of the stress tensor, and the effective viscoplastic strain. The fitting results tabulated in Table 3.2 show that the viscoplastic energy and effective viscoplastic strain coefficients (*Hc* and *Ec*) are positive, whereas the I_1 coefficient (*Lc*) is negative suggesting that the inelastic energy and effective strain are proportionally correlated to damage whereas the confining pressure is inversely proportional.

The fitting method described previously was programmed using Microsoft Visual Basic 6.0 and Mathcad 2001 Professional. The Mathcad program was used to determine the model parameters by the method or error minimization. The determined parameters were then fed to the Visual Basic program to simulate the triaxial strength and creep tests. The Visual Basic program was developed such that it can perform any type of loading condition where the applied stresses were entered in their general tensorial format.

CONCLUSIONS AND RECOMMENDATIONS

This chapter presents an anisotropic viscoplastic continuum damage model that linked the microstructure properties in terms of the aggregate orientation distribution and

the nucleation and growth of voids to the viscoplastic deformation of the material. The model was developed with the understanding that permanent deformation is driven by the distortion energy induced by shear stresses. This energy is dissipated in three mechanisms. The first one is overcoming the friction between the aggregates coated with binder. The second mechanism is overcoming the interlocking between the aggregates, which is responsible for the material dilation. The third mechanism is the energy required to overcome the bonding between the binder elements (cohesion), and between the binder and aggregates (adhesion).

An isotropic hardening parameter that is a function of the effective viscoplastic strain was used in the yield function. The aggregate distribution was described by the vector magnitude (Δ), which quantifies the material anisotropy. The vector magnitude is a function of the aggregate properties and compaction method. IAT were used to measure the aggregate distribution and calculate the vector magnitude.

A damage parameter based on the effective stress theory was used in the model. The damage parameter was postulated to be a function of the viscoplastic energy, confining pressure, and effective viscoplastic strain. The damage parameter reflected the nucleation and growth of voids that cause a reduction in the material load-carrying capacity. Including the damage parameter enabled capturing the tertiary creep behavior.

A parametric study was conducted to investigate the effect of some key parameters on the model. The model showed sensitivity to the material anisotropy, captured by the vector magnitude, the strain rate, and void nucleation and growth, captured by the damage parameter. The increase in the vector magnitude caused an increase in the material stiffness

in the axial direction normal to the preferred orientation of aggregates. An increase in the strain rate caused an increase in the material stiffness. The damage parameter gave the model the capability of predicting the tertiary creep.

Laboratory triaxial strength and static creep tests of AC mixes from the ALF of the FHWA were used to obtain the model parameters. The results showed that the model had a good match with the experimental measurements. However, the damage coefficients predicted from the creep tests were different from those obtained from the strength tests. This was attributed mainly to the wide range of strain rates involved in the static creep tests which were significantly different than the one used in the strength tests.

CHAPTER IV

IDENTIFICATION OF ASPHALT CONCRETE PERMANENT DEFORMATION PARAMETERS USING TRIAXIAL STRENGTH TESTS AND A MICROSTRUCTURE-BASED VISCOPLASTIC CONTINUUM MODEL

OVERVIEW

Complex interactions take place within the microstructure of Asphalt Concrete (AC) due to the different length scales and material properties involved. One of the main challenges in modeling AC is the ability to capture the manifestations of these interactions using a reasonable experimental program, a systematic analysis procedure, and a continuum model that accounts for the phenomena influencing performance.

This chapter presents experimental and analytical methodologies to determine important material properties that influence AC permanent deformation at high temperatures. This is achieved by analyzing data from compressive triaxial tests conducted at different confining pressures and strain rates within the framework of a non-associated microstructure-based viscoplastic continuum model. The model is developed to account for several phenomena known to influence AC permanent deformation such as aggregate structure friction, aggregate structure dilation, confining pressure dependency, strain rate dependency, anisotropy, and microstructure damage following the mix hardening. The presented model is shown to account for these phenomena and match the experimental data fairly well.

INTRODUCTION

Advances in continuum modeling of permanent deformation of AC have been reported by a number of researchers (Abdulshafi and Majidzadeh 1984, Lytton et al. 1993, Sousa et al. 1993, Sousa and Weissman 1994, Florea 1994a, Florea 1994b, Scarpas et al. 1997a, Lu and Wright 1998, Seibi et al. 2001, Huang et al. 2002, Cela 2002). These efforts have contributed significantly to the understanding of the mechanisms and factors influencing the AC performance. Most of these models, however, have been developed based on macrostructure measurements only and assuming AC to be isotropic.

Damage and anisotropy are important microstructure properties that influence the behavior of granular materials (Oda and Nakayama 1989, Scarpas et al. 1997a). Defects in the form of air voids and cracks (voids) exist initially in most granular materials. The growth and interlinkage of voids within the microstructure control the deformation leading to failure (Khaleel et al. 2001).

One of the main limitations in applying classical plasticity theory to AC remains in the universal assumption, based on Drucker's postulates (Drucker and Prager 1952), that plastic behavior is associated (Zeinkiewicz et al. 1975). This means that the function that defines the onset of plastic deformation is the same one that determines the directions and proportions of the strain components. However, there seems to be strong evidence that plastic deformation of AC, and granular materials in general, is non-associated (Zeinkiewicz et al. 1975, Oda and Nakayama 1989, Florea 1994a, Florea 1994b). The anisotropic nature of granular materials' microstructure contributes to this non-associated behavior as the principal directions of stresses do not coincide with those

of strains. Unlike their isotropic counterparts, anisotropic materials exhibit directionally dependent mechanical properties and thus isotropic theories are inapplicable (Arramon et al. 2000).

An associated microstructure viscoplastic continuum model for AC permanent deformation was developed in Chapter III. The model included an anisotropy parameter to account for the effect of aggregate distribution and a damage parameter to account for voids. The model inherits the advantages of continuum theory such as numerical implementation, and at the same time includes microstructure properties that influence permanent deformation.

In this chapter, the model developed in Chapter III is improved to account for the non-associated behavior of AC. The model parameters are determined using an experimental program and analysis procedures that reflect the different factors influencing the permanent deformation of AC. It is expected that this model will contribute to bridging the link between AC microstructure properties and its macroscopic response. Consequently, design and construction methodologies can be developed to create AC with a microstructure that contributes to improved performance.

OBJECTIVES

1. Develop an improved non-associated microstructure-based viscoplastic model of AC permanent deformation based on the one developed in Chapter III with modification based on experimental observations.

2. Introduce parameters in the improved model that reflect the different phenomena influencing permanent deformation of AC. These phenomena include the aggregate structure friction, aggregate structure dilation, confining pressure dependency, strain rate dependency, anisotropy, and damage.
3. Develop consistent experimental and analytical methodologies to determine the model parameters based on data from triaxial compressive strength tests conducted at different confining pressures and strain rates.

VISCOPLASTIC CONTINUUM MODEL

The general response of AC to load can be described by an elasto-visco-plastic model, while the relative contribution of each component depends on temperature and rate of loading. Several studies have shown that the viscoplastic component (including the instantaneous plastic component) is the underlying mechanism of permanent deformation at relatively high temperatures, while the accumulated viscoelastic contribution to permanent deformation is relatively small (Uzan 1996, Chehab et al. 2003). This chapter focuses on AC response at high temperatures, and consequently the viscoplastic deformation. The viscoplastic strain rate is defined using the flow rule in Eq. (4-1):

$$\dot{\varepsilon}_{ij}^{vp} = \Gamma \cdot < \phi(f) > \cdot \frac{\partial g}{\partial \sigma_{ij}} \tag{4-1}$$

where $\dot{\varepsilon}_{ij}^{vp}$ is the viscoplastic strain rate tensor; Γ is the fluidity parameter, which establishes the relative rate of viscoplastic straining; g is the viscoplastic potential

function; $\frac{\partial g}{\partial \sigma_{ij}}$ is a measure of the direction of viscoplastic strain; $\phi(f)$ is the viscoplastic yield function; and < > are the Macauley brackets indicating the following:

$$< \phi(f) >= \begin{cases} 0, & \phi(f) \le 0 \\ \phi(f), & \phi(f) > 0 \end{cases} \tag{4-2}$$

The associated flow rule applies if $g = f$. However, a number of researchers have shown that granular materials generally exhibit anisotropic microstructural distribution, which makes the viscoplastic potential function different than the yield function (non-associated behavior) (e.g. Zeinkiewicz et al. 1975, Oda and Nakayama 1989, Florea 1994b).

The well known Ducker-Prager yield function was modified in the previous chapter to include the effect of the aggregate anisotropic distribution and crack evolution during deformation. This was done by including a damage parameter ξ, which was defined based on the effective stress theory as the ratio of the area of voids to the total cross sectional area of a specimen. The effective stress theory indicates that the actual stress driving deformation is the load divided by the intact area, and hence the macroscopic calculated stress should be magnified by a factor equal to $1/(1-\xi)$. The effect of aggregate anisotropy was captured by including a microstructure tensor F_{ij} quantifying the directional distribution of aggregates in AC. This tensor makes the influence of the stress on deformation directionally dependent, which should be the case for an anisotropic material. The modified yield function has the form:

$$f = \sqrt{\bar{J}_2^e} - \alpha \bar{I}_1^e - \kappa \tag{4-3}$$

where,

$$\bar{I}_1^e = \frac{(a_1 \delta_{ij} + a_2 F_{ij})\sigma_{ij}}{1 - \xi} \tag{4-4}$$

$$\bar{J}_2^e = \frac{(2b_1 \delta_{ik}\delta_{jl} + 4b_2 F_{ik}\delta_{lj})S_{ij}S_{kl}}{(1 - \xi)^2} \tag{4-5}$$

σ_{ij} and S_{ij} are the stress tensor and the corresponding deviatoric tensor, respectively, and they are related as $S_{ij} = \sigma_{ij} - \frac{1}{3}\sigma_{kk}\delta_{ij}$; α is a parameter that reflects the material internal frictional and aggregate interlocking properties; κ is a parameter that reflects the combined effect of cohesion and frictional properties; and a_1, a_2, b_1, and b_2 are anisotropy material coefficients as will be shown subsequently.

The yield function in Eq. (4-3) is expressed in terms of invariants that are simple polynomials of the stress tensor and aggregate microstructure tensor (F_{ij}). This tensor can be formulated using different directional quantities such as directions of the contacts or longest axes of particles as discussed by Masad et al. (2002b). However, experience has shown that the directions of the longest aggregate axes in AC are easier and more practical to measure than contacts (Tashman et al. 2001, Masad et al. 2002b). In general, the components of this tensor can be determined using three-dimensional measurements of particle distribution or by conducting measurements on two-dimensional sections of the material that are extended to the three-dimensional tensor using stereological techniques. This latter approach is used in this chapter to determine the components of the aggregate distribution tensor. Previous studies have presented experimental measurements proving

that AC exhibits transverse anisotropy and that the major and minor axes of the aggregate distribution correspond to the horizontal and vertical directions, respectively (Masad et al. 1998, Tashman et al. 2001). Consequently, the aggregate distribution tensor can be written as follows (Oda and Nakayama 1989):

$$F_{ij} = \begin{pmatrix} (1-\Delta)/(3+\Delta) & 0 & 0 \\ 0 & (1+\Delta)/(3+\Delta) & 0 \\ 0 & 0 & (1+\Delta)/(3+\Delta) \end{pmatrix} \tag{4-6}$$

where the vector magnitude (Δ) quantifies the level of anisotropy measured on two-dimensional vertical sections of AC as follows:

$$\Delta = \frac{1}{M}\left[\sum_{k=1}^{M}(\cos 2\theta^k)^2 + \sum_{k=1}^{M}(\sin 2\theta^k)^2\right]^{\frac{1}{2}} \tag{4-7}$$

where θ_k is the orientation of an individual aggregate on a two-dimensional image of an AC cut section ranging from -90^o to +90^o and M is the total number of aggregates analyzed in an image. Theoretically, the value of Δ ranges between zero (isotropic material) and unity (all aggregates are oriented in one direction). Finally, the a_1, a_2, b_1, and b_2 coefficients in Eqs. (4-4, 4-5) are functions of the second invariant (D_2) of the deviatoric microstructure tensor as follows (Oda and Nakayama 1989):

$$a_1 = 1 - \lambda(2D_2)^{1/2},\ a_2 = 3\lambda(2D_2)^{1/2},\ b_1 = \frac{1}{4} - \frac{\mu}{2}(2D_2)^{1/2},\ b_2 = \frac{3}{4}\mu(2D_2)^{1/2} \tag{4-8}$$

where λ and μ are material coefficients that factor the effect of anisotropy on the confining and shear stresses, respectively. Upon substituting Eq. (4-3) in Eq. (4-2), and assuming a power law for the viscoplastic yield function, Eq. (4-2) becomes:

$$< \phi(f) >= \begin{Bmatrix} 0, No\,Viscoplastic\,Strain & \sqrt{\bar{J}_2^e} - \alpha \bar{I}_1^e - \kappa \le 0 \\ \left[\sqrt{\bar{J}_2^e} - \alpha \bar{I}_1^e - \kappa\right]^N, Viscoplastic\,Strain\,Occurs & \sqrt{\bar{J}_2^e} - \alpha \bar{I}_1^e - \kappa > 0 \end{Bmatrix} \quad (4\text{-}9)$$

where N is a constant to be determined experimentally.

The viscoplastic potential function g is assumed to have a form similar to the corresponding yield function f:

$$g = \sqrt{\bar{J}_2^e} - \beta \bar{I}_1^e - c \quad (4\text{-}10)$$

where β is a parameter that reflects the dilative potential of the material. As a result, β influences the proportions of the volumetric and deviatoric strains. The associated flow rule applies only if β is equal to α. However, a number of researchers have shown that β is smaller than α for granular materials (Zeinkiewicz et al. 1975, Oda and Nakayama 1989) as illustrated in Fig. 4.1.

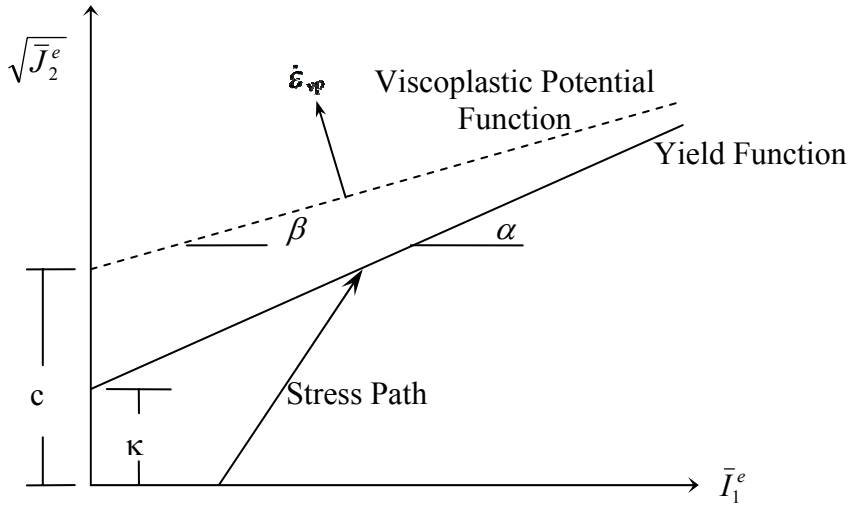

Fig. 4.1. Drucker-Prager Criterion (Non-Associated Flow)

The improved model discussed previously was developed to account for several important phenomena that are believed to be associated with permanent deformation of AC. They include the effect of the binder fluidity (Γ)*;* confinement and aggregate friction (α); aggregate interlocking and dilation (β); cohesion (κ); anisotropy (Δ); and damage (ξ). The model reduces to the classical Drucker-Prager isotropic hardening model for the special case of isotropic and intact (no damage) material.

EXPERIMENT

When determining the AC material parameters defining the constitutive behavior of AC at high temperatures, it is critical to use an experimental program that accounts for the factors that are known to influence these parameters. Triaxial strength tests have been well established in the field of granular materials and have been shown to be suitable for evaluating AC properties (Smith 1951, Tan et al. 1994, Seibi et al. 2001). The laboratory experiments conducted in this chapter included strain controlled triaxial compressive strength tests at five displacement rates and three confining pressures. The displacement rates were 0.1-mm/min, 0.5-mm/min, 2.5-mm/min, 12.5-mm/min, and 62-mm/min. The confining pressures were 0-psi, 15-psi, and 30-psi. All tests were conducted at a temperature of 130 ^{o}F. Recent studies have shown that AC is a thermorheologically simple material well into the large strain viscoplastic regime at elevated temperatures (Schwartz et al. 2002, Chehab et al. 2003). Therefore, the results of the experiment conducted in this chapter can be expanded using shift factors to cover the viscoplastic response at different temperatures and strain rates.

Test specimens were compacted using a ServoPac gyratory compactor to a size of approximately 101.6-mm (4-in) diameter and 157.5-mm (6.2-in) height. The applied load deformed the specimens at strain rates of 0.0660%/min, 0.318%/min, 1.60%/min, 8.03%/min, and 46.4%/min. The measured average air void content was approximately 6.7% with a standard deviation of 0.25%. The mixture was comprised of limestone aggregate and 4.85% PG 64-22 binder by weight of mixture. Fig. 4.2 shows the gradation of the limestone aggregates used in this chapter.

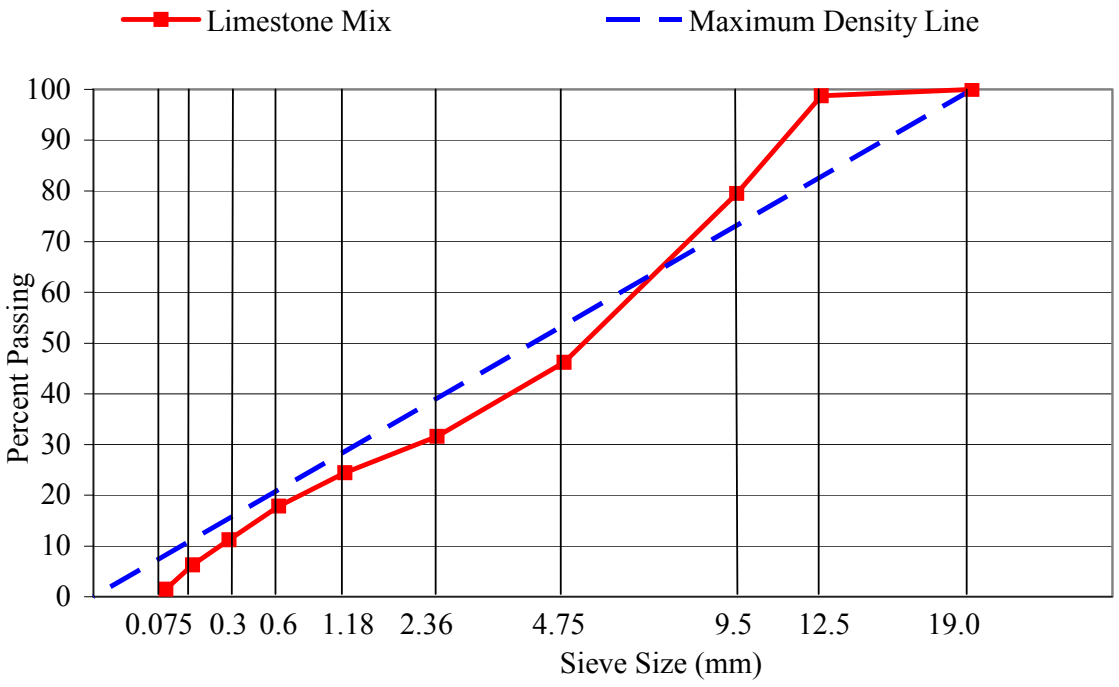

Fig. 4.2. 0.45 Power Gradation Chart of the Limestone Aggregates

All specimens were loaded to an axial strain of 8% or until failure, whichever occurred first. Two replicates were tested at each combination of strain rate and confining pressure for a total of 30 specimens. In addition, six more specimens were tested at three different combinations of strain rate and confining pressure for the purpose of measuring radial deformation. These three combinations were: (i) strain rate of 1.60%/min at a 0-psi confining pressure; (ii) strain rate of 1.60%/min at a 30-psi confining pressure; and (iii) strain rate of 46.4%/min at a 0-psi confining pressure. Radial deformation was measured using a Linear Variable Differential Transformer (LVDT) that was fixed around the specimen's circumference. The LVDT is capable of measuring deformations of up to 4-mm. This corresponded to an axial strain of about 1.5%, after which there was no experimental measurements of the radial deformation.

RESULTS AND ANALYSIS

A systematic procedure was developed in this chapter to determine the model parameters and their evolutions under loading. The first step was to determine a flow stress at which viscoplastic deformation starts. This was achieved with the aid of axial and radial strain measurements. Fig. 4.3 shows the plastic strain rate ratio (PSRR), which is defined as the ratio of the radial strain rate to the axial strain rate as follows:

$$PSRR = \frac{-\dot{\varepsilon}_{33}}{\dot{\varepsilon}_{11}} = \frac{-\left(\frac{\partial g}{\partial \sigma_{33}}\right)}{\left(\frac{\partial g}{\partial \sigma_{11}}\right)} = \frac{\left(\frac{\sqrt{X}}{2} + \beta(1+\frac{Y}{2})\right)}{\left(\sqrt{X} - \beta(1-Y)\right)} \tag{4-11}$$

where,

$$X = \frac{1}{3} - \frac{4}{9}\sqrt{24}\mu\left(\frac{\Delta}{3+\Delta}\right)^2 \tag{4-12}$$

$$Y = \frac{4}{3}\sqrt{24}\lambda\left(\frac{\Delta}{3+\Delta}\right)^2 \tag{4-13}$$

Fig. 4.3 shows that the confining pressure slightly reduces the PSRR. However, this seems to be a weak trend, and therefore, it was assumed that the PSRR was independent of the strain rate or confining pressure. It should be noted that the specimen with the label "1.60%/min, 0-psi, No2" did not deform uniformly during the test. Instead its deformation was non-uniform or skewed and hence was not included in the analysis. Thus, the "Avg." curve in Fig. 4.3 represents the average PSRR of the remaining five specimens.

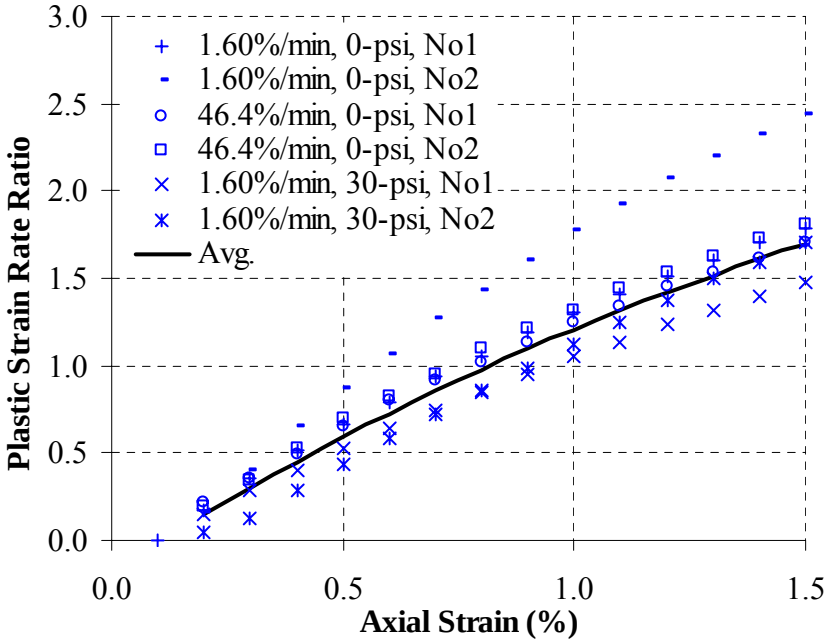

Fig. 4.3. Plastic Strain Rate Ratio (PSRR)

As depicted in Fig. 4.3, PSRR exceeded a value of 0.5 at an average axial strain of approximately 0.5%. At this point, the material started to dilate and the stress-strain curve deviated from a straight line. Therefore, this strain level was considered to mark the initiation of viscoplastic deformation (flow stress).

Fig. 4.4 shows the triaxial compressive strength test data. Each curve represents an average of two replicates. The figure shows the effect of the strain rate and confining pressure. As can be seen, higher strengths are associated with higher strain rates and/or confining pressures. To accommodate the analysis of the model parameters, Eq. (4-1) is rearranged as follows:

$$\sigma_{11} = \frac{(1-\xi)}{\sqrt{X} - \alpha(1-Y)} \cdot \left[\left(\frac{\dot{\varepsilon}_{11}^{vp}(1-\xi)}{\Gamma\left[\sqrt{X} - \beta(1-Y)\right]} \right)^{1/N} + \kappa - 2\sigma_{33} \frac{\left[\frac{-\sqrt{X}}{2} - \alpha\left(1+\frac{Y}{2}\right) \right]}{(1-\xi)} \right] \qquad (4\text{-}14)$$

By definition, no hardening or damage evolution takes place prior to the flow stress. Thus, the flow stress-strain rate curves at the three confining pressures were used to determine all material parameters except the hardening and damage parameters, i.e., Γ, N, α, β, κ_o, λ, and μ. In addition, these parameters were determined such that the PSRR value was satisfied at the flow stress. The value of the PSRR at the flow stress (0.5% axial strain) was determined from Fig. 4.3 and was found to be approximately 0.59. The initial values of the vector magnitude and damage are needed to solve Eq. (4-14). The vector magnitude was determined using Image Analysis Techniques (IAT) presented by (Tashman et al. 2001) on 8 images of cut sections of two AC specimens, which were selected randomly. The average vector magnitude was found to be 39% with a standard

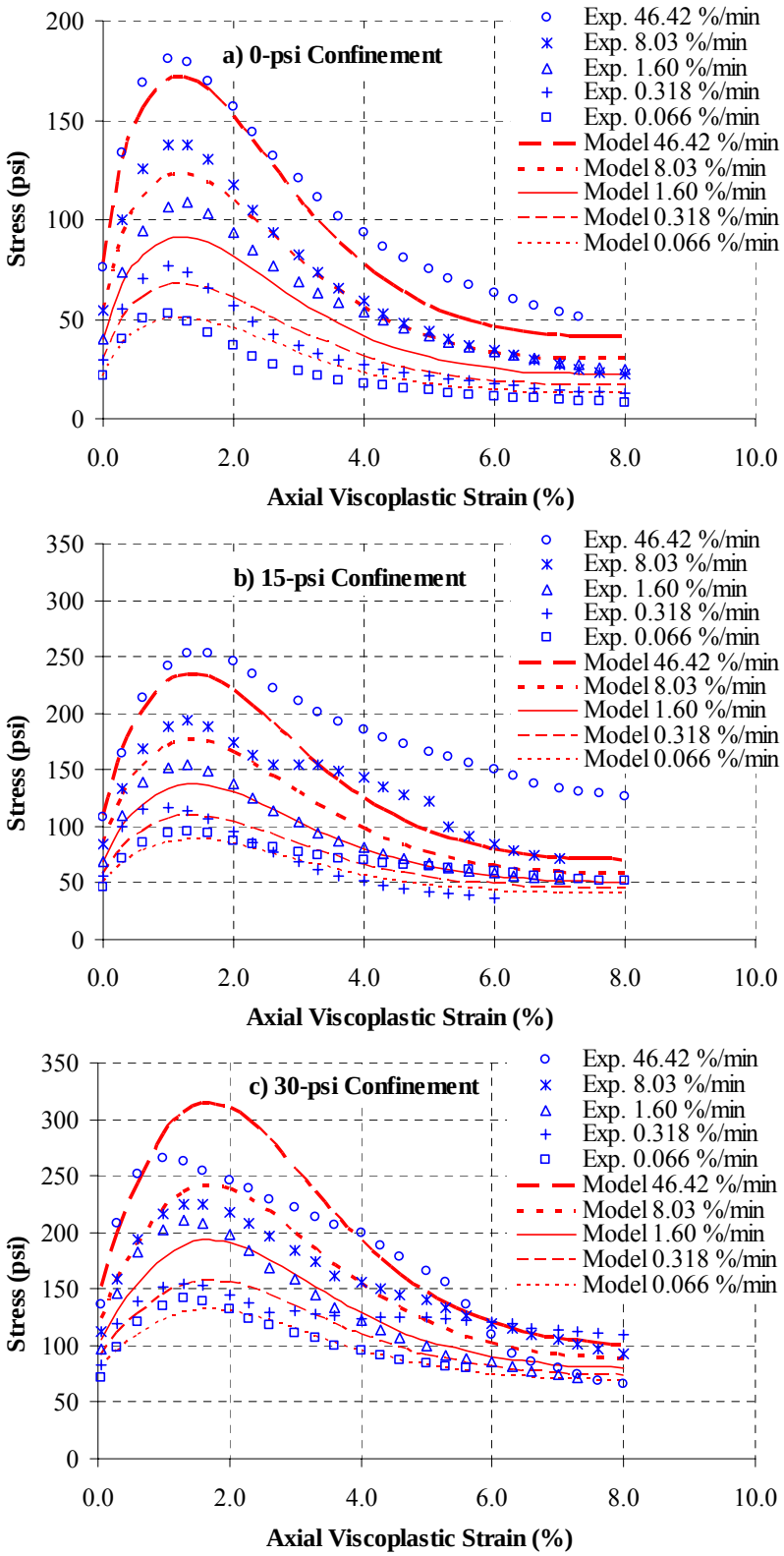

Fig. 4.4. Experimental and Model Stress-Viscoplastic Strain Relationship

deviation of 4.7%. The initial value of damage was assumed to be equal to the air void content after compaction. Fig. 4.5 compares the model and the experimental data in terms of the flow stress as a function of the strain rate at the three confining pressures. The model matches the experimental data fairly well.

It is noteworthy that the model was not capable of matching the experimental data in Fig. 4.5 well when the associated flow rule was used. A good match was only achieved using the improved model with the non-associated flow rule. This is consistent with the findings of other researchers regarding the deformation of granular materials (Zeinkiewicz et al. 1975, Oda and Nakayama 1989, Florea 1994b). The experimental measurements were also used to determine the evolution of the model parameters, namely the vector magnitude or anisotropy parameter Δ, the hardening parameter κ, and the damage parameter ξ, as follows:

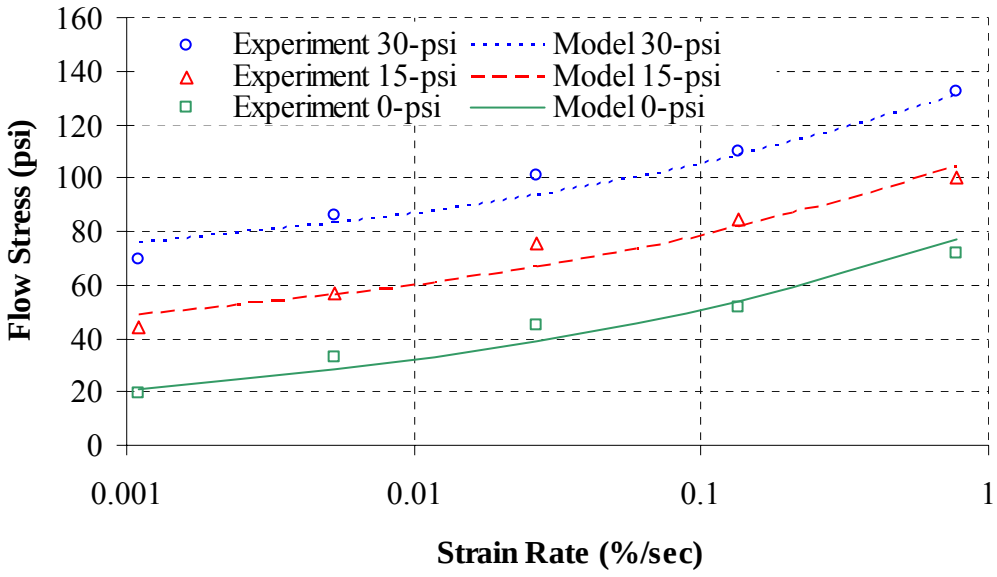

Fig. 4.5. Flow Stress-Strain Rate Curve at the Three Confinement Pressures

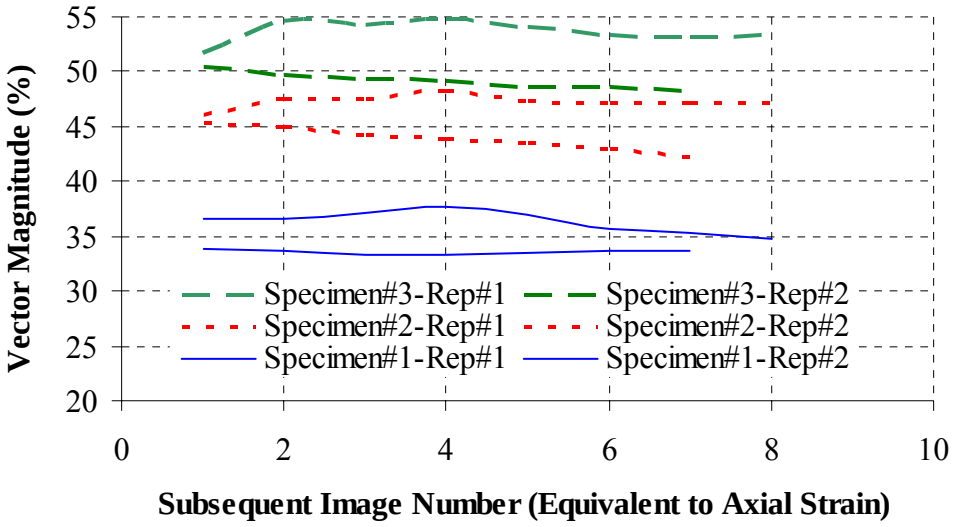

Fig. 4.6. Effect of Deformation on the Vector Magnitude

Anisotropy Parameter

The initial value of the vector magnitude (inherent anisotropy) depends on the aggregate characteristics, aggregate gradation, and the compaction method used to prepare the specimen (Masad et al. 1999a, Masad et al. 1999b, Tashman et al. 2001). Dessouky et al. (2003) presented experimental results showing that the initial value and the evolution of the vector magnitude during compaction are functions of aggregate shape and gradation.

In order to measure the evolution of the vector magnitude, an experiment was conducted in which successive images were taken for AC cut sections subjected to compression loading. These sections were cut from gyratory specimens prepared at different gyrator variables (angle of gyration, specimen height, and compaction pressure)

that produced different levels of anisotropy. It was found that the vector magnitude did not change significantly as shown in Fig. 4.6. Thus, the inherent anisotropy seems to be the major factor that differentiates between mixes depending on their aggregate properties. Consequently, the vector magnitude was assumed constant throughout the deformation.

Work Hardening and Dilation Parameters

The experimental data in Fig. 4.4 and Eq. (4-14) were used to solve for the yield surface parameters α and κ at each strain increment beyond the flow stress. Figs. 4.7 and 4.8 show that both α and κ increase with viscoplastic strain up to a point after which α saturates and κ begins to decrease. The increase of α and κ indicate that the material behavior was dominated mainly by work hardening of the material due to deformation. The point at which κ started to decrease (about 0.7% viscoplastic strain), indicates that another mechanism besides hardening was taking place in dominating the behavior of the mix. As such, the evolution law of κ was determined from the experimental measurements up to 0.7% viscoplastic strain. The α value was assumed to be constant and equal to the average initial value of 0.1.

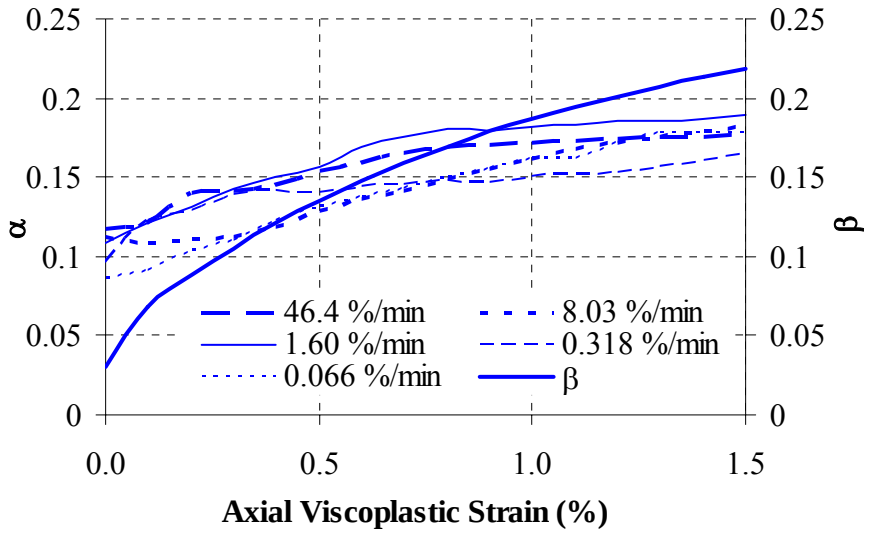

Fig. 4.7. Evolution of α and β

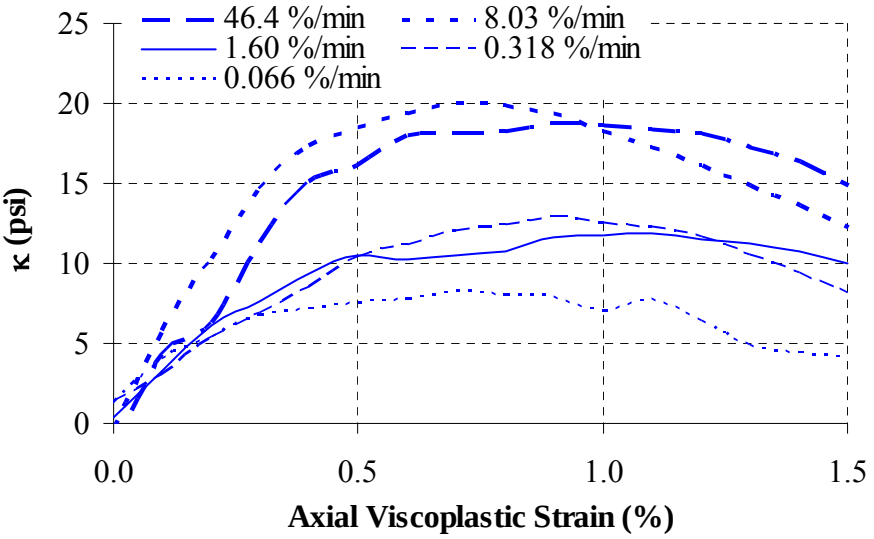

Fig. 4.8. Evolution of the Hardening Parameter κ

The evolution law in Eq. (4-15) was used initially to describe an isotropic hardening of κ:

$$\dot{\kappa} = H\dot{\bar{\varepsilon}}_{vp} \tag{4-15}$$

where H is the isotropic hardening coefficient and $\dot{\bar{\varepsilon}}_{vp}$ is the effective viscoplastic strain rate. H was postulated to be a power law function of the effective viscoplastic strain $\bar{\varepsilon}_{vp}$ as follows:

$$H = h\left(\bar{\varepsilon}_{vp}\right)^{\eta} \tag{4-16}$$

Solving the differential equation (4-15), the hardening parameter κ can be written as follows:

$$\kappa = \kappa_o + \frac{h}{\eta+1}\left[\left(\bar{\varepsilon}_{vp}\right)^{\eta+1} - \left(\bar{\varepsilon}_{vp}^{o}\right)^{\eta+1}\right] \tag{4-17}$$

where $\bar{\varepsilon}_{vp}^{o}$ is initial effective viscoplastic strain and κ_o defines the initial yield surface. For a monotonic state of loading $\bar{\varepsilon}_{vp}^{o}$ is equal to zero and Eq. (4-17) reduces to the following form:

$$\kappa = \kappa_o + \kappa_1\left(\bar{\varepsilon}_{vp}\right)^{\kappa_2} \tag{4-18}$$

where κ_o, κ_1, and κ_2 are material hardening coefficients to be determined experimentally. The effective viscoplastic strain rate is defined to match the axial viscoplastic strain rate for a triaxial state of loading as follows:

$$\dot{\bar{\varepsilon}}_{vp} = \frac{\left[\sqrt{X} - \beta\left(1-Y\right)\right]}{\sqrt{\frac{3}{2}X + 3\beta Y\sqrt{X} + 3\beta^2 + \frac{3}{2}\beta^2 Y^2}}\sqrt{\dot{\varepsilon}_{ij}^{vp}\dot{\varepsilon}_{ij}^{vp}} = \dot{\varepsilon}_{11}^{vp} \tag{4-19}$$

and the effective viscoplastic strain would be the integration of Eq. (4-19) over time,

$$\bar{\varepsilon}_{vp} = \int_t \dot{\bar{\varepsilon}}_{vp} dt \tag{4-20}$$

The power law coefficients κ_1 and κ_2 were determined at each strain rate following the power law function in Eq. (4-18). It was found that the shape of the hardening function was independent of the strain rate but its value was highly dependent on the strain rate. Therefore, it was proposed that the hardening parameter is strain rate dependent and thus the evolution law in Eq. (4-18) was modified as follows:

$$\kappa = \kappa_o + \kappa_1 \left(\bar{\varepsilon}_{vp}\right)^{\kappa_2} \left(\dot{\bar{\varepsilon}}_{vp}\right)^{\kappa_3} \tag{4-21}$$

in which κ_o is determined initially from the flow stress-strain rate curve and κ_1, κ_2, and κ_3 are material hardening coefficients determined by fitting the experimental data between the flow stress and 0.7% viscoplastic strain.

The dilation parameter was determined by solving Eq. (4-11) for β as a function of the effective viscoplastic strain as follows:

$$\beta = \beta_1 - \beta_2 e^{(-\beta_3 \cdot \bar{\varepsilon}_{vp})} \tag{4-22}$$

where, β_1, β_2, and β_3 are positive coefficients. Eq. (4-11) was solved with the anisotropy parameters determined from the measurements of the vector magnitude and from fitting Eq. (4-14) at the flow stress as discussed previously and shown in Fig. 4.5.

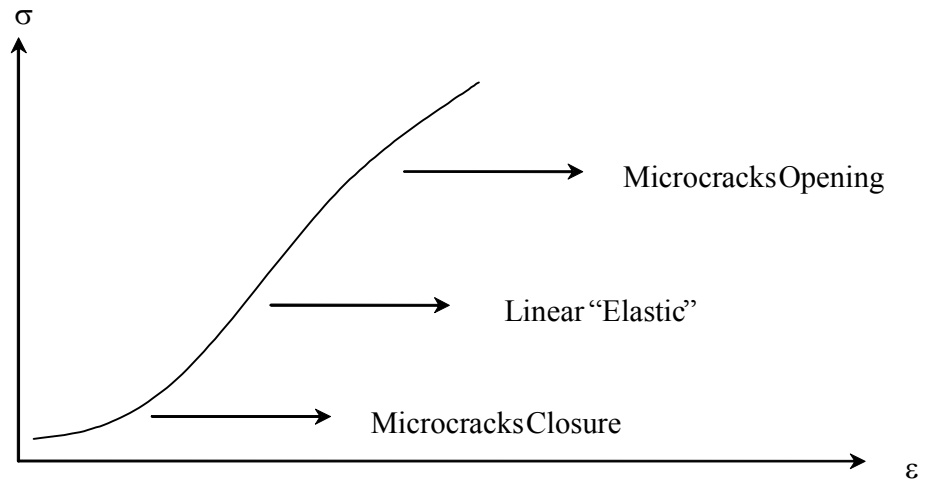

Fig. 4.9. The Three Distinct Stress-Strain Curve Portions in Cemented Granular Materials

Damage Evolution

Typically, there are three distinct portions of the stress-strain curve for "cemented" granular materials as shown in Fig. 4.9 (Cristescu 1994). The first portion is a nonlinear one that occurs at low stresses and corresponds to the closure of microcracks oriented orthogonal to the applied stress. The second portion is nearly linear which has a slope similar to an elastic material during which there is no significant occurrence of microcracking. The third portion is nonlinear and during which microcracks develop and propagate until they become macrocracks leading to failure. The stress-strain curves in this chapter followed this pattern. It was therefore assumed that during the first two portions, the material was still adjusting and deforming elastically. The point at which κ started to decrease was assumed to correspond to a point in the third portion where macrocracks start dominating the AC response. This point is referred to in this chapter as

the “damage threshold”.

The evolution of the damage parameter was determined by fitting the experimental data from the damage threshold point until failure. It was found that the evolution of the damage parameter follows the generalized logistic form, which is widely used for growth modeling. This is consistent with the findings by Sousa et al. (1993) for the damage function obtained from shear strain sweeps and shear creep tests. Following the generalized logistic curve shown in Fig. 4.10, damage evolution was postulated in the following form:

$$\xi = L + \frac{U}{\left(1 + T \cdot e^{\left[-G(\bar{\varepsilon}_{vp} - M)\right]}\right)^{\frac{1}{T}}} \tag{4-23}$$

where L is a constant that controls the initial damage (lower asymptote); U is a constant that controls the maximum damage (upper asymptote); G controls the growth rate of damage; M controls the point of maximum growth; and T controls where maximum growth occurs (near the lower or upper asymptote). Fig. 4.10 shows that the confining pressure acts as a retardor causing a delay in the damage growth. Thus, it was assumed that M in Eq. (4-23) is a function of the initial confining pressure ($I_o/3$) as follows:

$$M = M_o \cdot e^{\left(M_1 \cdot \frac{I_o}{3}\right)} \tag{4-24}$$

where M_o and M_1 are damage growth coefficients.

As can be seen, the damage evolution was found to be described by a growth function while nucleation (formation of cracks) did not affect the description of damage. AC is compacted under high shear stresses to a certain air void content. Consequently, air voids and possibly microcracks have already nucleated during compaction. The

damage form in Eq. (4-23) is in agreement with the hypothesis by Sumpter (2003) that the growth of the crack is strain based since strain can be correlated with an increment of crack tip displacement at the crack tip.

It should be noted that Fig. 4.10 shows that the damage parameter reached a value close to a unity which is very high in the context of classical effective stress theory as it corresponds to a 100% air voids. However, the damage parameter should be understood in terms of its physical influence on the material deformation. This damage parameter accounts for the portion of the material that loses its load-carrying capacity during deformation. As mentioned earlier, this was done in the model by magnifying the stress at any point in time by a ratio of the inverse of the percentage of the intact material.

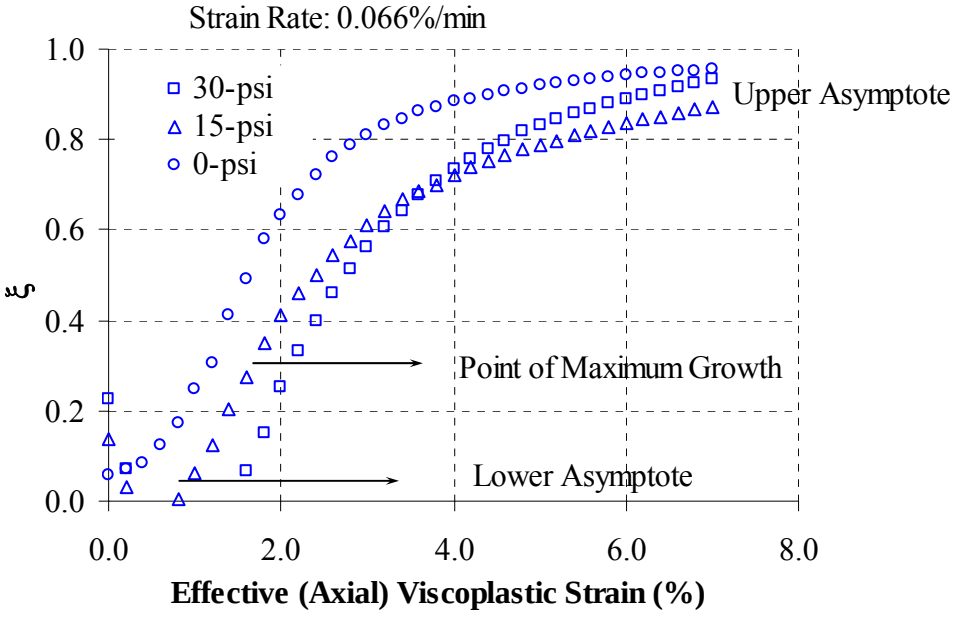

Fig. 4.10. Generalize Logistic Damage Growth

Fig. 4.4 shows a comparison between the model and the experimental data. Given the nature of the AC as a material that experiences significant testing variability, the model matches the experimental data fairly well. Including the damage parameter in the model enabled capturing the softening behavior of the material, which occurs as soon as the damage mechanism overcomes the work hardening of the material.

CONCLUSIONS AND RECOMMENDATIONS

An improved non-associated microstructure-based viscoplastic continuum model was developed to model the permanent deformation of AC. The model has a damage parameter to account for the effect of void growth in softening the material. The model also has an anisotropy parameter to account for the aggregate distribution within the microstructure.

Triaxial compressive strength tests conducted at five strain rates and three confining pressures were used to systematically determine important material parameters that represent different phenomena influencing the permanent deformation of AC. These phenomena include the aggregate structure friction, aggregate structure dilation, confining pressure dependency, strain rate dependency, anisotropy, and damage.

A flow stress and a damage threshold were defined. The material parameters were determined based on the assumption that work hardening is the dominant deformation mechanism between the flow stress and the damage threshold; thereafter, the damage mechanism becomes dominant and deformation is primarily influenced by the void growth.

Aggregate gradation, aggregate shape properties, method of compaction, and compaction effort influence the aggregate structure distribution. The anisotropy parameter (vector magnitude) provided the capability to account for aggregate structure distribution in the model.

Including the damage parameter in the model enabled capturing the softening behavior of AC, which occurs as soon as the damage mechanism overcomes work hardening resulting in a drop in the load-carrying capacity of the material. The model was found to be in good agreement with the experimental data.

CHAPTER V

DAMAGE EVOLUTION IN TRIAXIAL COMPRESSION TESTS OF ASPHALT CONCRETE AT HIGH TEMPERATURES

OVERVIEW

This chapter presents the results of an experiment aimed at capturing and characterizing damage evolution in Asphalt Concrete (AC) at relatively high temperatures. AC specimens were loaded using a triaxial compression setup to four predefined strain levels at three confining pressures. X-Ray Computed Tomography (CT) was used to capture the microstructure of the AC specimens before and after they were deformed, and Image Analysis Techniques (IAT) were used to characterize the evolution of air voids and cracks (voids) in the deformed specimens. IAT were developed to distinguish between air void growth and crack evolution. This is extremely important as the underlying mechanisms for these two phenomena are different.

Damage in AC is shown to initiate following a period of microstructure hardening. The damage is found to be a localized phenomenon in the sense that there exists a critical section in a specimen that is mainly responsible for failure. The growth and propagation of cracks in this critical section was significantly larger than that in the rest of the specimen. This chapter shows that the top part of the specimens exhibited significant cracking, the middle part exhibited significant dilation, and minor microstructural changes occurred in the bottom part. These variations within a specimen are attributed mainly to the heterogeneity of the AC microstructure.

The results of this chapter are expected to have significant impacts on the current state of knowledge with regard to damage evolution due to permanent deformation at high temperatures. The results demonstrate that there is a pressing need to prepare homogenous specimens in the laboratory. Otherwise, localization due to microstructure heterogeneity will render the interpretation of laboratory testing results a very difficult task. More importantly the findings of this chapter will influence the approaches typically followed in the development of permanent deformation models. These models should account for the effect of damage localization on accelerating permanent deformation.

INTRODUCTION

Microstructural damage is the main mechanism responsible for failure in AC. It results in significant degradation of the load-carrying capacity of AC due to discontinuities that develop at localized high stress intensity and/or weak regions along the binder-aggregate interface (adhesive failure) and/or within the binder (cohesive failure). Damage is believed to begin with the nucleation of microcracks that later propagate, grow, and coalesce to form macrocracks as the material is subjected to loading (Kim et al. 1997). The growth and interlinkage of these cracks within the microstructure control the stress-strain response and deformation that leads to failure (Khaleel et al. 2001).

Researchers have addressed the importance of damage and its evolution in properly modeling AC (Schapery 1982, Schapery 1987, Sousa et al. 1993, Schapery 1994, Park et al. 1996, Kim et al. 1997, Lee et al. 2000, Sadd et al. 2003, Collop et al. 2003). Scarpas et al. (1997b) reported that response degradation in most loading ranges normally begins with

nucleation followed by localization and eventually propagation of cracks. Little et al. (1999) and Lytton (2000) have emphasized the importance of microcracks growth and healing on damage and performance of AC. Park et al. (1996) stated that AC experiences a significant level of microcracking under service loading, which is assumed to be a considerable source of the nonlinear behavior. In addition, they stated that any mathematical model that duly describes the constitutive behavior of AC must account for the effect of damage growth. Sousa et al. (1993) noted that adding a damage component to a permanent deformation model significantly improves its ability to predict experimental measurements. It should be noted that the majority of the previous studies on AC damage are related to low and intermediate temperatures.

In spite of the overwhelming evidence on the significant influence of damage on AC performance, most of the available continuum models for AC are developed without direct experimental measurements of damage. Damage in these models has been characterized through quantifying changes in mechanical properties with respect to a damage-free reference state. Although this is a commendable approach, it is influenced by the methods used to analyze the mechanical response and is limited by the theory used to interpret these results. This situation prevents continuum damage mechanics (CDM) from becoming a state-of-the-practice technique for engineering applications (Wang et al. 2001).

The understanding of the deformation process is extremely limited without a clear understanding of the evolution of the microstructure (Krishna and Rajagopal 2002). Thus, there is a vital need to directly measure and quantify damage in AC in order to understand and account for damage using mechanics-based concepts supported by measurements. This

would allow developing relationships between the microstructural features which control damage behavior and bulk mechanical properties of interest to researchers (Landis and Keane 1999). Moreover, microstructures can be optimized to reduce the areas of heterogeneity concentration and strain localization that are responsible for damage and degradation in macroscopic mechanical response (Maire et al. 2001), and hence performance.

Recently, several successful attempts to quantify the microstructure of AC mixtures using imaging technology and X-Ray CT have been made (Synolakis et al. 1996, Landis and Keane 1999, Shi et al. 1999, Masad et al. 1999a, Tashman et al. 2001, Wang et al. 2001, Masad et al. 2002a). X-Ray CT is fast becoming a powerful nondestructive tool by which to characterize the microstructure of AC and other engineering materials without damaging the specimens being tested. X-Ray CT sectional images can be used to reconstruct the three-dimensional microstructure of a sample for computer simulation. Meanwhile the sample remains intact and can be used for determining other macro properties (Wang et al. 2001).

The focus of using X-Ray CT in AC has primarily been on characterizing the air void distribution but not on damage evolution during loading. This is at the vital level of CDM where there is always a need for a damage evolution law. In addition, damage distribution has been shown to be non-uniform, thus it is not sufficient to quantify damage visually and relate it to deformation of the material. Rather, statistical analysis of damage distribution and its evolution is needed.

The objective of this chapter is to experimentally capture and characterize the evolution of damage in AC as the material undergoes permanent deformation. X-Ray CT and IAT are utilized to capture and characterize the AC microstructure at different stages of deformation and confining pressures and the data are statistically analyzed. In addition, the implications of the damage measurements on modeling AC permanent deformation are discussed within the framework of a continuum damage model that has been developed in the previous chapter.

EXPERIMENT

Twenty four AC specimens were fabricated with a ServoPac gyratory compactor. The mix consisted of limestone aggregates with 4.85% of PG 64-22 binder by weight of mixture. Fig. 5.1 shows the aggregate gradation used in this mix. The mix volumetrics met the specifications outlined in Superpave for high traffic roads (10-30 million ESALs). The specimens were prepared to achieve a target air void content of 7%. Each specimen had an average diameter of 101.6-mm (4-inch) and an average height of 157.5-mm (6.2-in). Specimens were labeled as LMD1, LMD2, …, LMD24 on the top side.

The microstructure of the AC specimens was captured using the nondestructive X-Ray CT system. The system had a 420 kV X-Ray source and a line detector. X-Ray CT offers a nondestructive method to obtain digital information on the microstructure of the specimens while the specimens are still intact and capable of being subjected to further mechanical testing.

In the simplest approach, directing planar X-Rays that pass through the specimen along several different paths in several different directions produces a set of CT images along the specimen's height. These generated two-dimensional CT images are typically referred to as slices. The intensity of X-Rays is measured before they enter the specimen and after they pass through it. Scanning of a slice is complete after collecting the intensity measurements for a full rotation through the specimen. The specimen is then shifted vertically by a fixed amount (the slice thickness) and the entire procedure is repeated to generate another segment of slices.

Two-dimensional images (slices) of the microstructure of the AC specimens were captured every 1-mm across the height of a specimen with a slice thickness of 1-mm. The resolution of the X-Ray CT images was 0.191-mm/pixel in the undeformed specimens and 0.234-mm/pixel in the deformed ones.

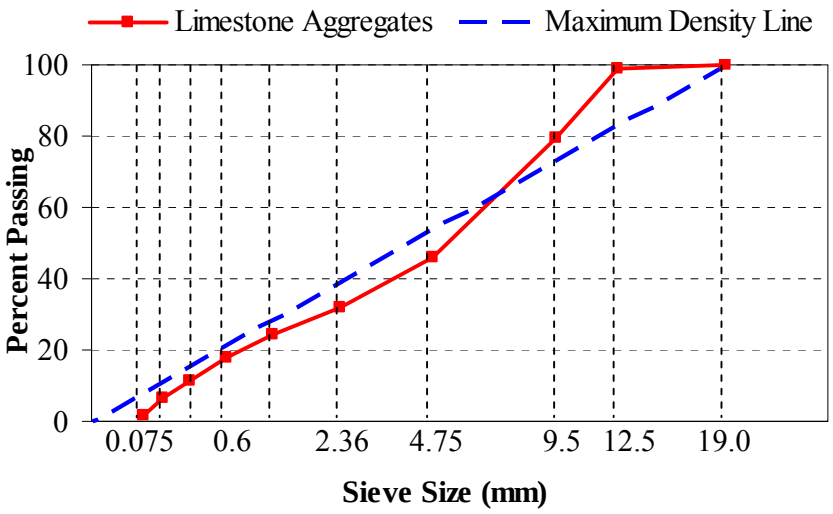

Fig. 5.1. 0.45 Power Gradation Chart of the Limestone Aggregates

Specimens were divided randomly to 12 groups (two replicates in each group). Then, they were loaded using a triaxial compression setup at a constant displacement rate of 2.5-mm/min such that the top side was always in contact with the loading ram. Each two replicates were loaded to a specified strain level under a constant confining pressure. The confining pressures were 0-psi, 15-psi, and 30-psi and the strain levels were 1%, 2%, 4%, and 8%. The void content of the specimens was measured after they were deformed using the CoreLok method. All tests were conducted at a temperature of 130 ^{o}F.

The digital images were analyzed using IAT to characterize different aspects of the void properties including the void content, size (void area), aspect ratio, eccentricity, roundness, and length of voids in each slice, where,

$$Void\ Content = \frac{\sum_{M} V}{A} \tag{5-1}$$

$$Aspect\ Ratio = \frac{Major\ Axis}{Minor\ Axis} \tag{5-2}$$

$$Eccentricity = \sqrt{x^2 + y^2} \tag{5-3}$$

$$Roundness = \frac{P^2}{4\pi V} \tag{5-4}$$

In Eqs. (5-1, 5-2, 5-3, 5-4) V is the area of a void in an image (slice); M is the total number of voids in a slice; A is the slice cross sectional area; x is the horizontal distance of a void's centroid from the center of the slice (specimen's core); y is the vertical distance of a void's centroid from the center of the slice; and P is the perimeter of a void

in a slice.

These parameters were chosen as they can be used to describe the void shape properties. The aspect ratio and the roundness are expected to distinguish between an air void and a crack; a perfectly circular air void has an aspect ratio and a roundness value of one, whereas a crack has a very high aspect ratio and roundness value (theoretically infinity). Eccentricity describes the in-plane radial distribution of voids in a slice; a void with an eccentricity value of zero indicates that it is located at the center of the slice (specimen core), whereas a void with an eccentricity of 50-mm indicates that it is located near the specimen's circumference. The void content gives the ratio of the total voids in a slice to the cross sectional area of that slice. The length of a void is defined as the length of a box that encompasses that void. If a void length becomes equal to the slice diameter, it is then an indication of a slice being split by that void.

RESULTS

Table 5.1 summarizes the strain values to which each specimen was deformed, confining pressures, and void contents before and after deformation. Fig. 5.2 shows the stress-strain curves of the specimens tested. Each curve represents an average of two replicates. Fig. 5.2 shows that a 1% strain occurred prior to reaching the peak point, 2% strain generally corresponded to the peak point, 4% was a post-peak point, and 8% corresponded to failure. Void contents at the different strain levels and confining pressures are shown in Fig. 5.3 which follows the generalized logistic curve or the so called S-curve. Fig. 5.3 shows that there was a slight decrease in the void content at 1%

strain (volume contraction), after which the void content exhibited a rapid growth up to 4% strain (volume dilation). Thereafter, the void content increased at a slower rate and almost stabilized at an average void content of 14% at 8% strain.

Table 5.1. Summary of Test Specimens

Specimen ID	[1]Strain (%)	Confining Pressure (psi)	[2]Void Content Undeformed Specimens (%)	[2]Void Content Deformed Specimens (%)
LMD1	1	0	7.40	7.27
LMD2	1	0	7.07	7.09
LMD3	2	0	7.12	7.64
LMD4	2	0	6.87	7.58
LMD5	4	0	7.32	9.83
LMD6	4	0	6.92	9.35
LMD7	8	0	7.12	12.76
LMD8	8	0	6.74	13.28
LMD9	1	15	7.15	6.96
LMD10	1	15	6.87	6.81
LMD11	2	15	7.03	7.50
LMD12	2	15	6.68	7.43
LMD13	4	15	7.19	10.01
LMD14	4	15	6.57	9.61
LMD15	8	15	7.15	13.64
LMD16	8	15	6.79	13.54
LMD17	1	30	7.17	7.11
LMD18	1	30	6.68	6.74
LMD19	2	30	7.16	7.88
LMD20	2	30	6.90	7.48
LMD21	4	30	7.20	9.29
LMD22	4	30	6.87	9.83
LMD23	8	30	7.31	13.70
LMD24	8	30	6.85	13.65
			Avg: 7.01 SD: 0.22	

1: Predefined strain at which the triaxial testing machine was stopped,
2: Air void content was measured using the CoreLok method

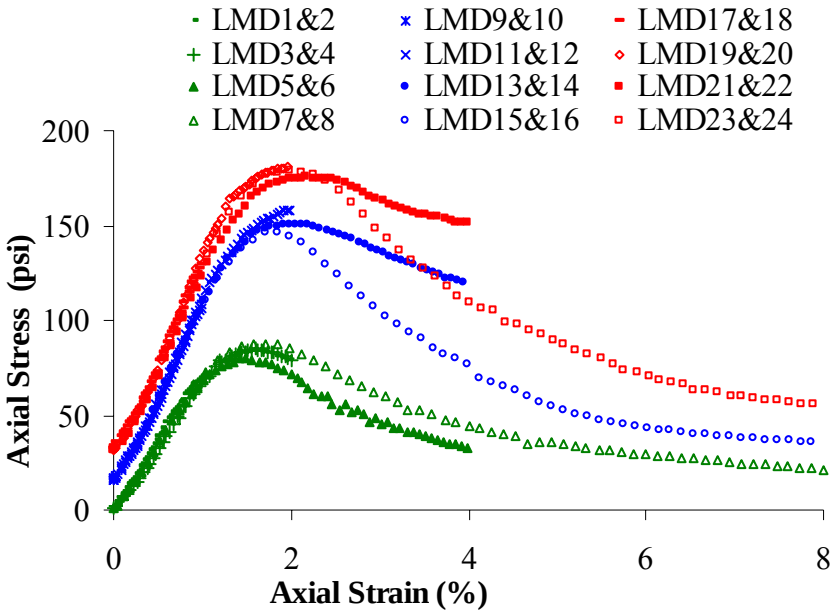

Fig. 5.2. Stress-Strain Curves of the Tested Specimens

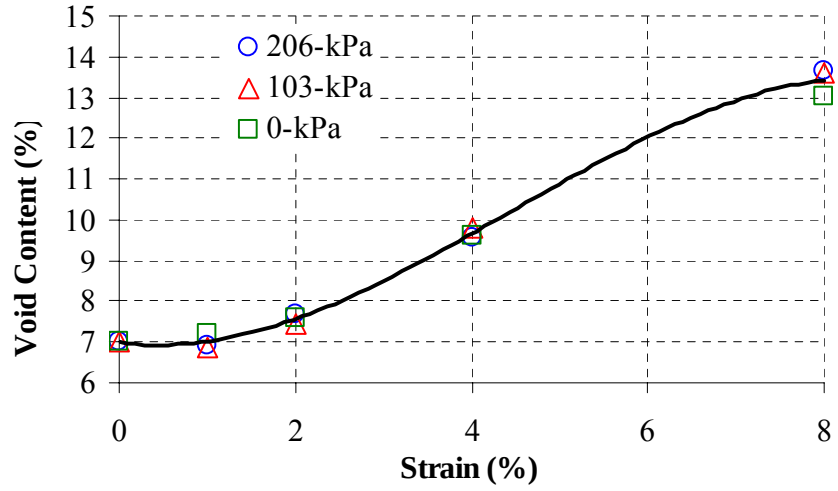

Fig. 5.3. Effect of Deformation on Void Content

Void Distribution in Undeformed Specimens

Fig. 5.4 shows the results of void measurements in the undeformed specimens. Each curve represents an average of the 24 undeformed specimens. The height ratio along the y-axis is defined as the ratio of the vertical distance of a slice from the top of the specimen to the total height of the specimen. It was decided to use the height ratio instead of the actual depth because the deformed specimens had varying heights.

Fig. 5.4(a) shows that the very first and last few slices possessed high void contents due mainly to the direct contact with the gyratory plates causing restriction in the mobility of the aggregates and reducing the efficiency of the kneading action there (Tashman et al. 2001). In addition, there were three distinct regions with respect to void distribution; two low void content regions at the top and bottom 20% of the height of the specimen with the top region having a higher void content, and one relatively high void content region in the middle of the specimen. This distribution is remarkably different than the distribution reported in a number of previous studies for 150-mm diameter and 100-mm height specimens, where the middle of the specimen was more compacted than the top and bottom portions (Masad et al. 1999a, Tashman et al. 2001). Evidently, the specimen's height and diameter play a major role in controlling the air void distribution. An increase in a specimen's height causes a significant reduction in the compaction of the middle portion, while most of the compaction takes place in the top and bottom portions. In this chapter, the void distribution was specifically studied in three regions: the top region (top 20% of the height); the middle region (middle 20% of the height); and the bottom region (bottom 20% of the height).

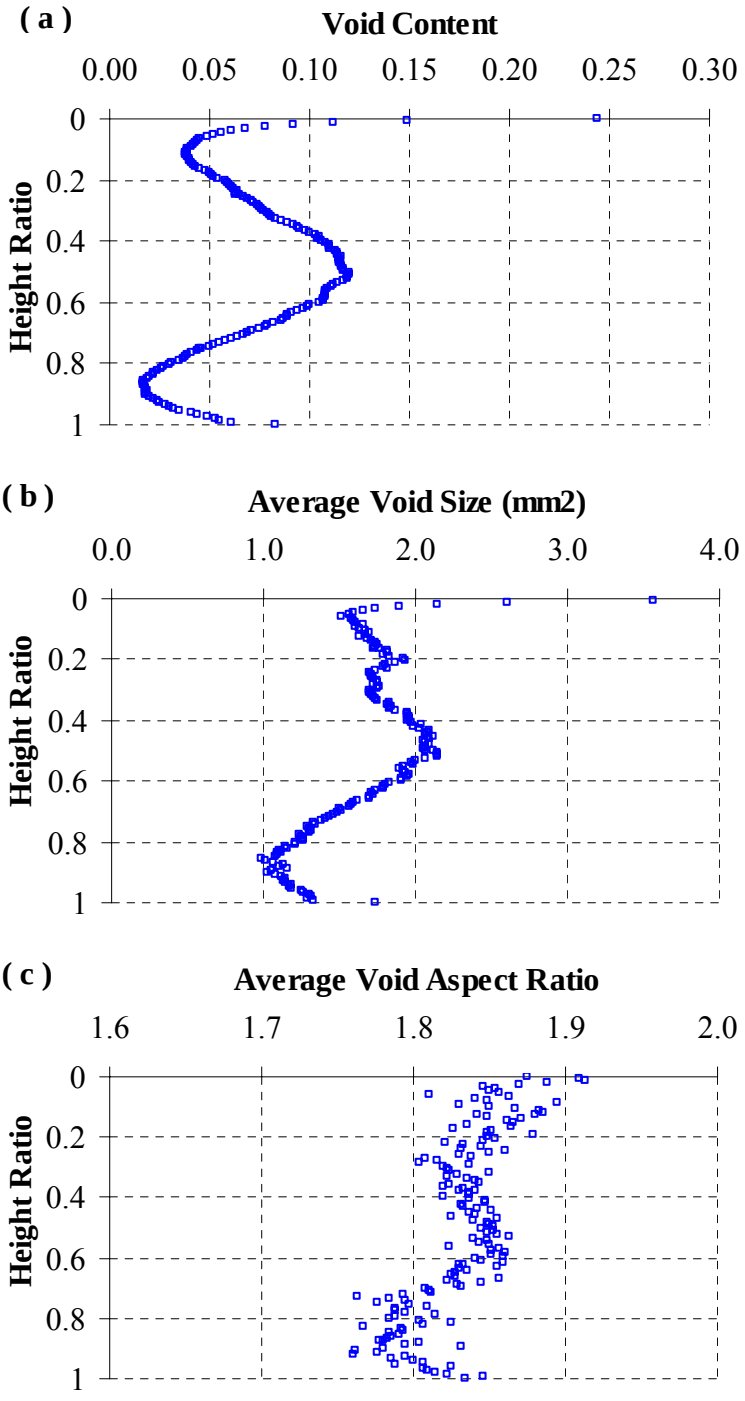

Fig. 5.4. Void Measurements in the Undeformed Specimens

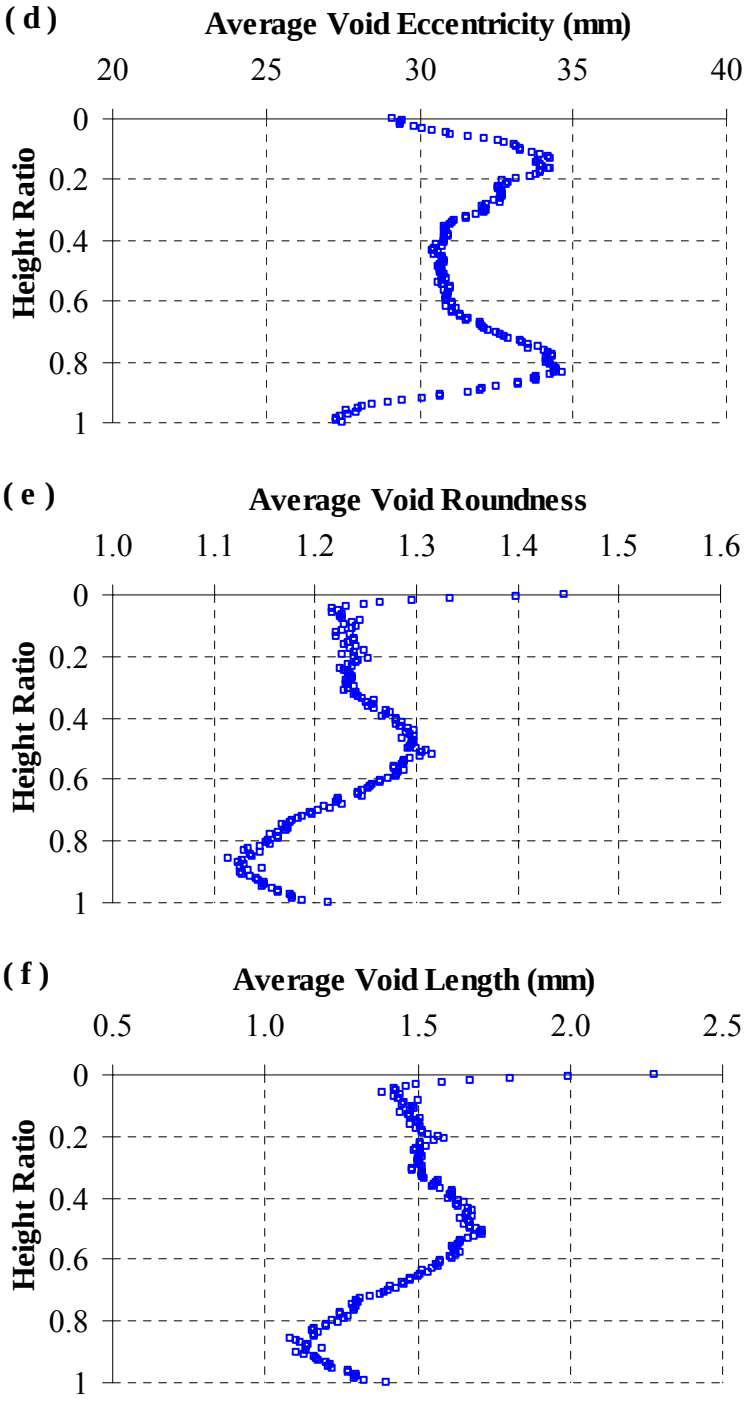

Fig. 5.4. Continued

Fig. 5.4(b) shows that the average void size was approximately 1.7-mm^2 in the top region; increased to about 2.0-mm^2 in the middle region; and dropped to about 1.0-mm^2 in the bottom region.

Fig. 5.4(c) shows that the average aspect ratio of the voids was generally the highest in the top region reaching a value of approximately 1.90; decreased to about 1.84 and remained almost constant in the middle region, and then dropped to less than 1.77 in the bottom region. This indicates that the voids in the top region were initially more elongated than in the other two regions with the bottom region having the least elongated voids.

Fig. 5.4(d) shows that the distribution of the average void eccentricity along the depth of the specimens was the opposite of the void content distribution shown in Fig. 5.4(a). Eccentricity, which is the radial distance of a void's centroid from the center of the specimen, was the highest in the slices with the lowest void content. Tashman et al. (2001) showed that the gyratory compaction effort is typically higher in the core of a specimen compared to the areas near its circumference. As the compaction effort increased (top and bottom regions), the proportion absorbed by the core of the specimen increased at the expense of the areas near the circumference causing a decrease in the void content at the specimen's core and consequently an increase in eccentricity.

Fig. 5.4(e) shows that the average roundness of voids was about 1.25 in the top region and increased to 1.30 in the middle region before it dropped down to 1.13 in the bottom region. As mentioned earlier, roundness describes the shape of voids; a roundness value of 1.0 indicates a perfectly circular void whereas a crack would

theoretically have a roundness value of infinity.

Fig. 5.4(f) shows that the average void length followed the same pattern as roundness. Both roundness and void length followed the void size pattern where they were the highest in the middle region, lowest in the bottom region, and a slight increase occurred in the top region at a height ratio of approximately 0.2.

Fig. 5.4 shows that the three distinct regions were not only different in the void content but also in the void shape properties.

Void Distribution in Deformed Specimens

Statistical analysis of variance (ANOVA) was conducted to analyze the factors influencing the void distribution. The analysis was based on a 95% level of confidence using MINITAB software (Minitab 13.32, 2000). A P-value of 0.05 or less indicates the factor is statistically significant, whereas a P-value greater than 0.05 indicates it is not. The experiment was a three-factor fixed effect model in which the specimen's height ratio, strain to which the specimen was deformed, and the confining pressure were the three fixed factors. The statistical responses included the change in the void content, average void size, average aspect ratio, average eccentricity, average roundness, and average length of voids per slice.

Table 5.2 shows the ANOVA P-values for the effect of height ratio, strain, and confining pressure on the change in void measurements. Table 5.2 shows that the height ratio and strain significantly affected all the void measurements considered in this chapter. Pressure, however, significantly affected some parameters but not others. The

effect of the confining pressure was found to be negligible compared to the effect of strain. For example, the percent difference in void size among specimens loaded under different confining pressures varied between 26% and 46% whereas it ranged between –8.0% and 140% due to the effect of strain. The percent difference in void roundness was between 4.5% and 5.5% under different confining pressures, while it was between -4.0% and 20.5% due to the effect of strain. In addition, the P-value for the effect of confining pressure on the measured void content shown in Table 5.1 and Fig. 5.3 was found to be 0.701. This indicates that the confining pressure had a negligible effect on void growth due to deformation. Based on the statistical analysis results, it was decided to focus on the effect of strain and height ratio in studying damage due to permanent deformation in the tested specimens.

Table 5.2. ANOVA P-values of the Effect of the Height Ratio, Strain, and Confining Pressure on the Change in Void Measurements

	Factor		
Response	Height Ratio	Strain	Confining Pressure
Change in Void Content	0.000	0.000	0.134
Change in [1]Average Void Size	0.000	0.000	0.000
Change in [1]Average Void Aspect Ratio	0.000	0.000	0.000
Change in [1]Average Void Eccentricity	0.000	0.000	0.000
Change in [1]Average Void Roundness	0.000	0.000	0.004
Change in [1]Average Void Length	0.000	0.000	0.063

1: Average per slice (image)

Fig. 5.5 shows the effect of strain on void measurements along the depth of a specimen. A positive value in the figure indicates an increase in the measured parameter with respect to the distribution prior to specimen deformation. At the initial stage of deformation, the air voids tended to contract and the existing microcracks tended to close up as indicated by the negative percent change in the void content at 1% strain in Fig. 5.5(a). Except for some few slices in the top and bottom regions, all other slices experienced a decrease in void content at 1% strain. The void content increased by about 10% indicating dilation of air voids and possibly microcracking at 2% strain. At 4% strain, the void growth was quite obvious with values reaching up to 60% in the top region and 30% to 40% in the middle region. At 8% strain, the three regions show distinct levels of change; the highest being in the top region with values exceeding 400%; the lowest in the bottom region with some values around 20% to 30%; and about 100% in the middle region.

Fig. 5.5(b) shows the percent change in the average void size. There was a decrease in the average void size at 1% strain. This confirms the results in Fig. 5.5(a) that voids contract initially during deformation. It is interesting to compare the results from Figs. 5.5(a&b) at 2% strain. The average void size decreased in Fig. 5.5(b) while the void content increased in Fig. 5.5(a). This indicates that new microcracks were formed under loading. At 4% strain, there was a clear increase in the average void size in the middle region, a decrease in the bottom region, and no change or a decrease in the top region.

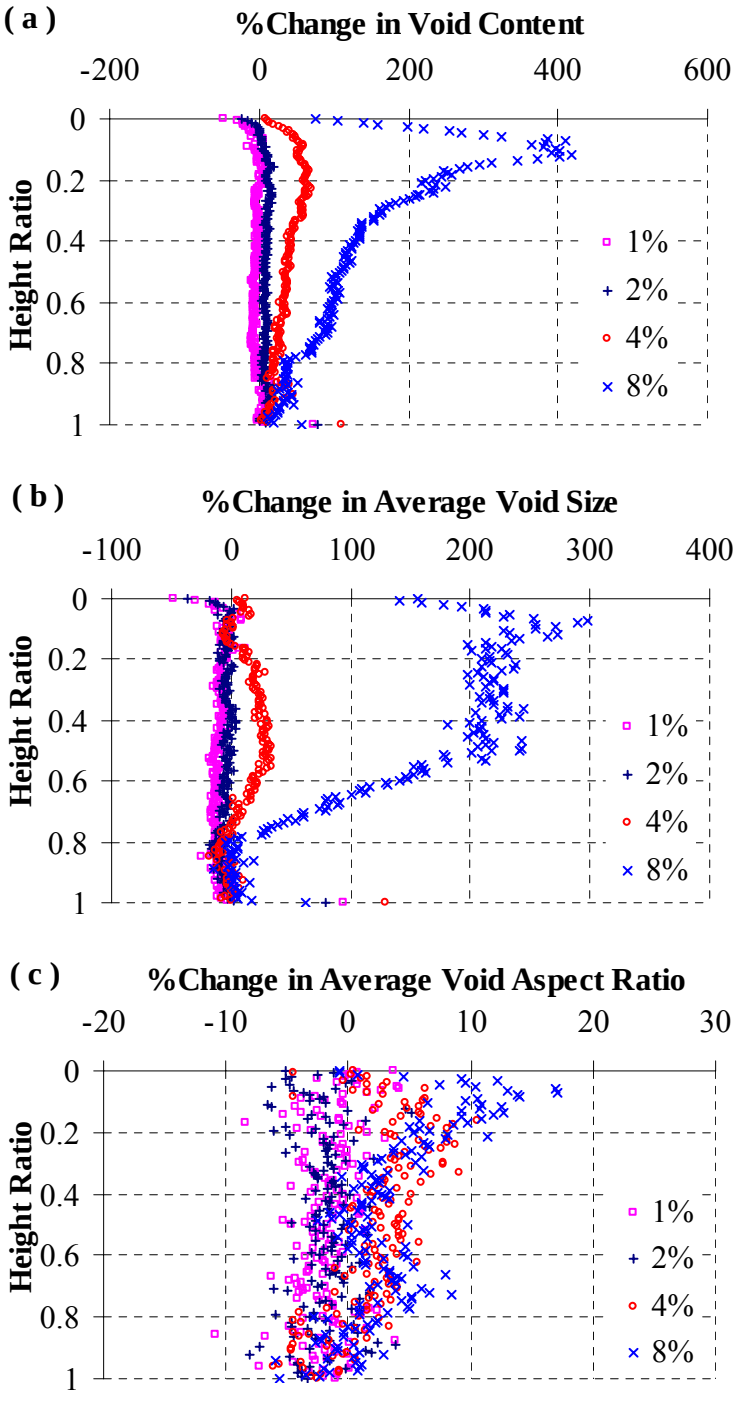

Fig. 5.5. Change in Void Measurements due to Deformation

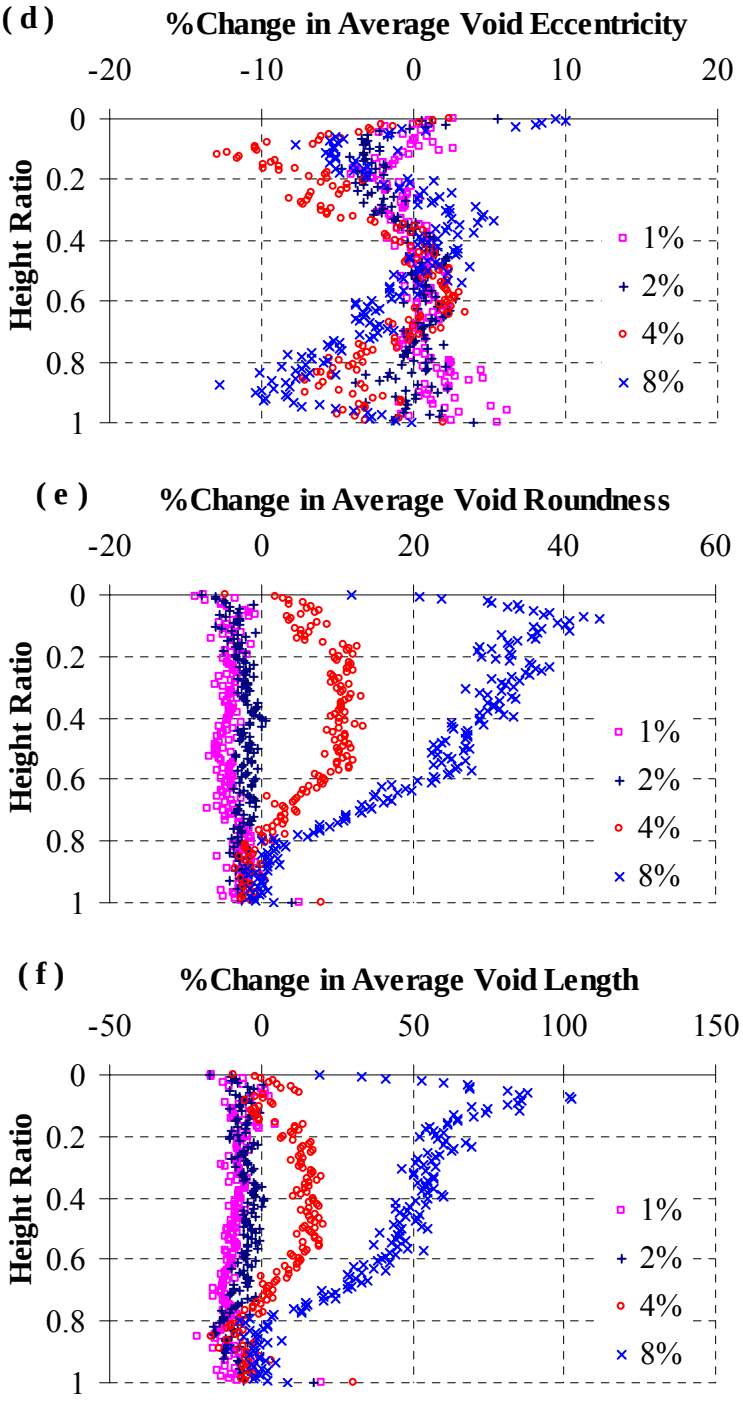

Fig. 5.5. Continued

However, Fig. 5.5(a) showed that the increase in the void content at 4% strain was the highest in the top region. Again, this confirms the finding that the number of voids (mostly cracks) has significantly increased at these critical slices in the top region. At 8% strain, crack and air void coalescence was clear in the top region causing the percent change in the void size to peak at 300%, and then decreased to about 200% to 220% in the middle region before decreasing to zero in some slices in the bottom region.

Fig. 5.5(c) shows that the change in the void average aspect ratio was relatively scattered with an average change of approximately zero at 1% and 2% strain. However, the figure shows that there was generally an overall increase in the aspect ratio in the top and middle region at 4% and 8% strain; the highest being clearly in the critical slices in the top region. This again is an indication of the development of macrocracks mainly in the top region.

Fig. 5.5(d) shows the change in the average void eccentricity. The eccentricity in the middle region did not change on average. In the bottom region, it increased at 1% strain, decreased to zero at 2% strain, continued to decrease at 4% strain, and reached its lowest value at 8% strain. In the top region, the eccentricity remained almost unchanged at 1% strain with a slight increase in the first few slices, slightly decreased at 2% strain, reached a decrease of 10% at 4% strain, and returned to 5% decrease at 8% strain. The increase in the top region at 1% strain indicates that the voids were contracting more in the specimen's core than near the circumference. As a result, the core was more likely to develop microcracks that grew to become macrocracks at 4% strain causing a decrease in the eccentricity. Thereafter, macrocracks made their way to the circumference,

splitting the slice and causing an increase in the eccentricity at 8% strain.

Figs. 5.5(e&f) show the change in the average roundness and length of voids. Both figures show almost the same pattern indicating a high correlation between roundness and length of voids. At the post-peak strain of 4%, crack development in the top region caused an increase in the average roundness and length of voids. In the middle region, the air voids have coalesced and met causing an increase in their average length and roundness. When two circular air voids meet, the roundness/length of the new air void is generally larger than the average of the two air voids before they coalesce. At failure (8% strain), the top region clearly showed a distinct peak indicating the existence of large macrocracks, the middle region experienced a significant amount of dilation causing coalescence of air voids, and the bottom region did not experience any significant change in void structure.

It is inferred from the results in Fig. 5.5 that damage, in terms of crack nucleation (initiation) and growth, occurred in the top region, and more specifically at a height ratio of approximately 0.10. Volume dilation or air void growth took place mainly in the middle region, and almost no change occurred in the bottom region. During the post-peak stage, microcracks grew to become visible macrocracks in the top region and the material continued to dilate in the middle region causing a significant increase in the void content (4% strain). After that, the material experienced a significant amount of macrocracking in the top region, minor change in the bottom region, and a significant amount of dilation in the middle region as shown in Fig. 5.6 by the bulging in the middle of the specimen. Fig. 5.7 shows that the void content continued to increase at a high rate

in the top region due to the crack growth, while the dilation in the middle region stabilized at high strain values.

Fig. 5.6. A Deformed AC Limestone Specimen

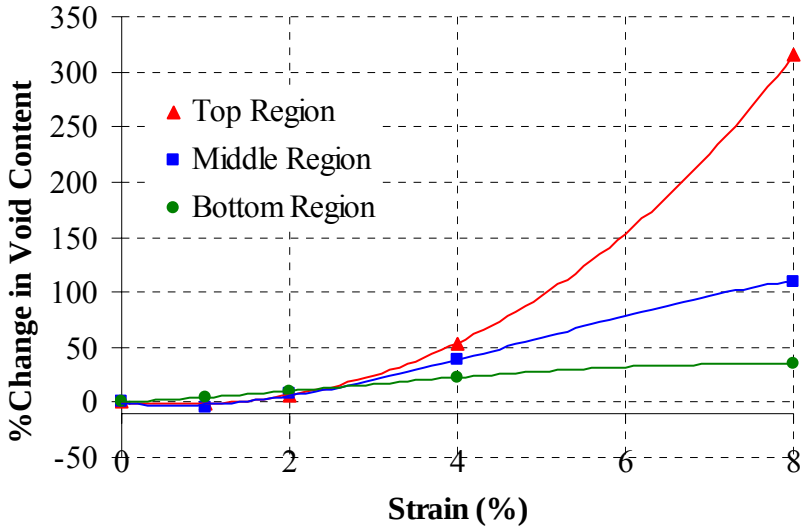

Fig. 5.7. Change in Void Content due to Deformation in the Top, Middle, and Bottom Regions

Fig. 5.5(a) shows that a high void content does not necessarily mean a potential damage region. Even though the void content in some slices in the middle region was about four times that of the top region, most of the damage occurred in the top region. The results clearly showed that compaction significantly influences damage initiation and growth. All results shown in Fig. 5.4 indicated that the top region was more susceptible to damage than the bottom one, but less susceptible than the middle region. The top region had a higher void content, bigger voids, and more elongated voids compared to the bottom region. However, the top region initially had a lower average void content, a lower average void size, a lower average roundness, a lower average void length, but a higher average aspect ratio and a higher average eccentricity than the middle region. Having initially a higher average aspect ratio and higher eccentricity might be an indication of compaction-induced damage in the top region due to being close to the top of the gyratory compaction plate causing a decrease in the void content particularly in the core of the specimen and possibly nucleating microcracks there. These inherent microcracks make the top region weaker and more vulnerable to damage. The findings on damage distribution can be seen by visual examination of the images given in Figs. 5.8, 5.9, 5.10, 5.11, and 5.12.

a) 0.1 Height Ratio-Top Region 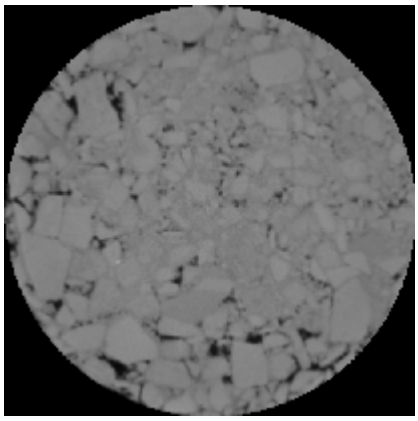

b) 0.5 Height Ratio-Middle Region 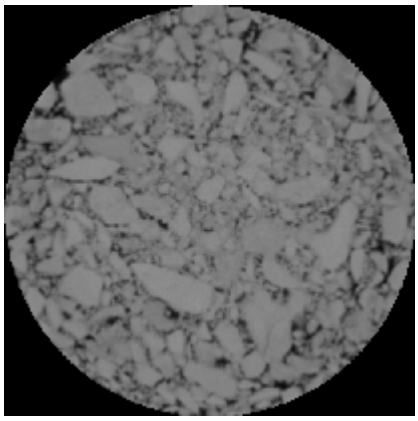

c) 0.9 Height Ratio-Bottom Region 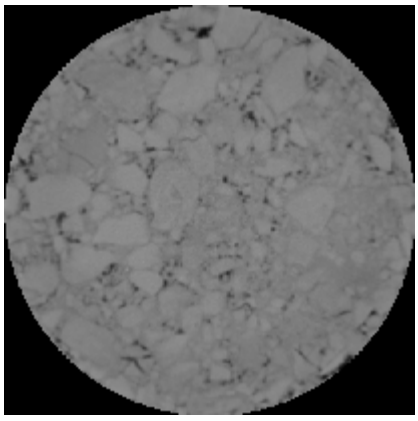

Fig. 5.8. Slices (Images) of an Undeformed Specimen (LMD5)

a) 0.1 Height Ratio-Top Region 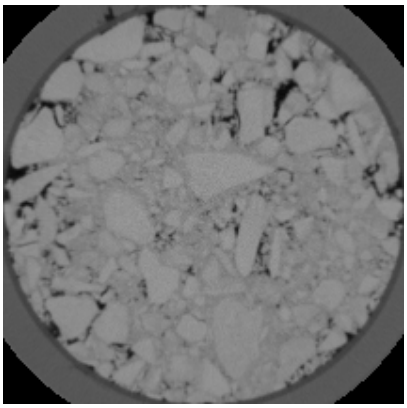

b) 0.5 Height Ratio-Middle Region 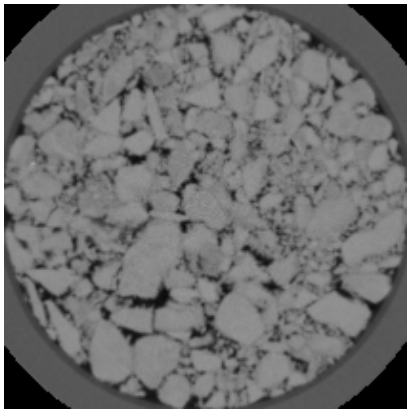

c) 0.9 Height Ratio-Bottom Region 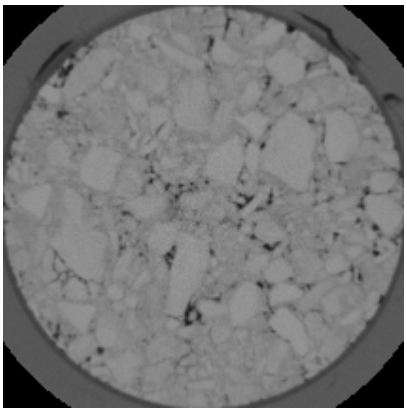

Fig. 5.9. Slices (Images) at 1% Strain (LMD9)

a) 0.1 Height Ratio-Top Region 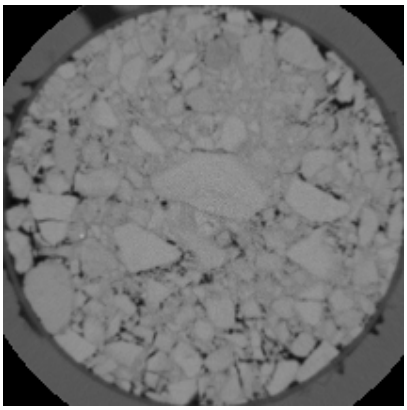

b) 0.5 Height Ratio-Middle Region 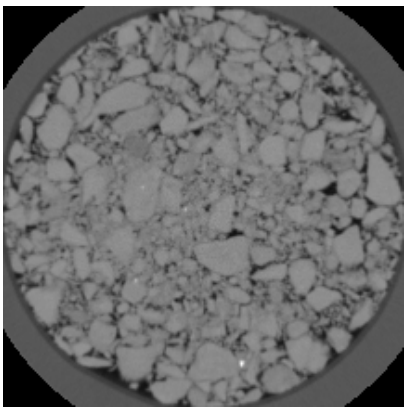

c) 0.9 Height Ratio-Bottom Region 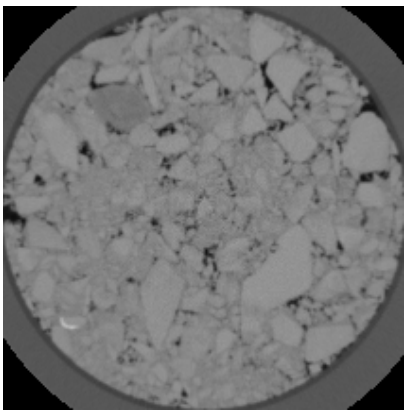

Fig. 5.10. Slices (Images) at 2% Strain (LMD12)

a) 0.1 Height Ratio-Top Region 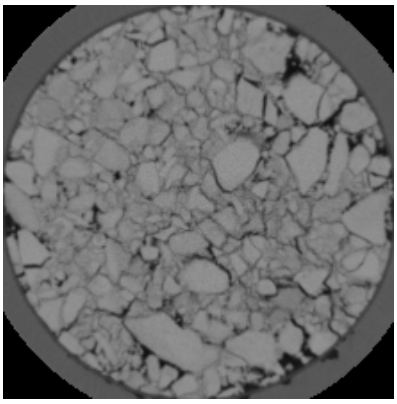

b) 0.5 Height Ratio-Middle Region 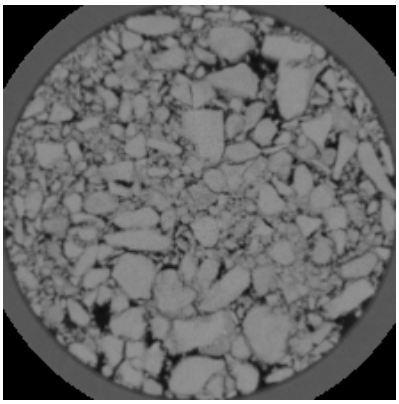

c) 0.9 Height Ratio-Bottom Region 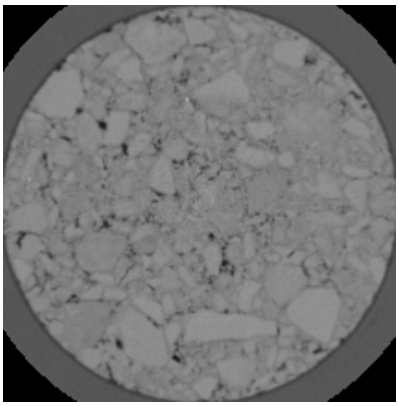

Fig. 5.11. Slices (Images) at 4% Strain (LMD13)

a) 0.1 Height Ratio-Top Region 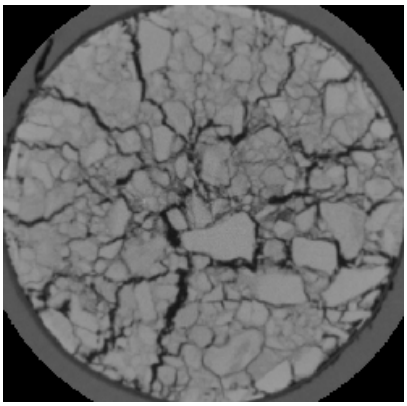

b) 0.5 Height Ratio-Middle Region 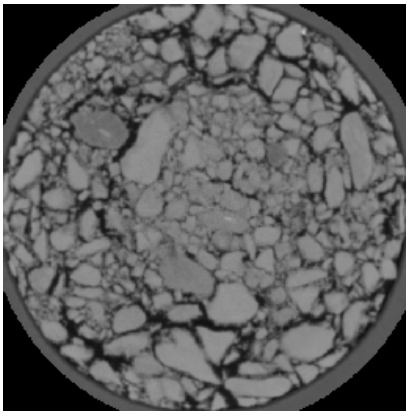

c) 0.9 Height Ratio-Bottom Region 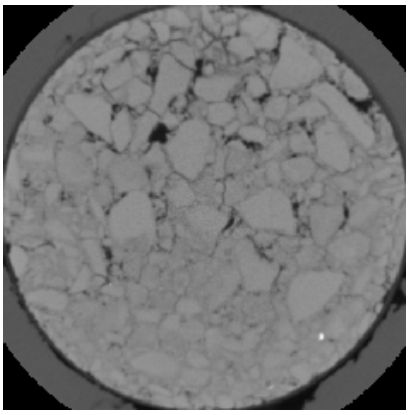

Fig. 5.12. Slices (Images) at 8% Strain (LMD24)

It can be speculated that the end effect of the triaxial testing machine might have caused high stress intensity zones in the top region that is close to the loading ram leading to more damage in the top. In order to investigate this possible effect, two specimens were rotated 180 degrees and tested. Both specimens did not experience a lot of deformation in the top region indicating that the microstructural distribution due to compaction was the main factor influencing the deformation process.

Implications on Experimental Characterization and Continuum Damage Modeling of AC

The results presented in the previous section have significant implications on laboratory characterization and continuum damage modeling of AC. The damage localization and nonuniform deformation cause high variability in the testing results. As such, this renders the testing results of less value in terms of comparing the performance of different mixes.

The influence of the findings on continuum damage modeling of AC mixes is discussed here within the framework of a microstructure viscoplastic continuum model that was developed in Chapter III and refined in Chapter IV. The model was developed based on Perzyna's theory of viscoplasticity with Drucker-Prager yield function modified to account for the material anisotropy and microstructure damage. The material anisotropy was captured through microstructural analysis of two-dimensional sections of AC mixes in terms of aggregate distribution. Furthermore, a damage parameter was included in the model in order to account for the reduction in the mix load-carrying

capacity due to voids. The viscoplastic strain was defined using the flow rule as follows:

$$\dot{\varepsilon}_{ij}^{vp} = \Gamma \cdot < \phi(f) > \cdot \frac{\partial g}{\partial \sigma_{ij}} \tag{5-5}$$

where $\dot{\varepsilon}_{ij}^{vp}$ is the viscoplastic strain rate tensor; Γ is the fluidity parameter, which establishes the relative rate of viscoplastic straining; g is the viscoplastic potential function; $\frac{\partial g}{\partial \sigma_{ij}}$ is a measure of the direction of viscoplastic strain; $\phi(f)$ is the viscoplastic yield function; and $< >$ are the Macauley brackets indicating that viscoplastic deformation develops only for positive values of $< \phi(f) >$. The modified yield and potential functions had the following forms:

$$f = \sqrt{\bar{J}_2^e} - \alpha \bar{I}_1^e - \kappa \tag{5-6}$$

$$g = \sqrt{\bar{J}_2^e} - \beta \bar{I}_1^e - c \tag{5-7}$$

where,

$$\bar{I}_1^e = \frac{(a_1 \delta_{ij} + a_2 F_{ij}) \sigma_{ij}}{1 - \xi} \tag{5-8}$$

$$\bar{J}_2^e = \frac{(2b_1 \delta_{ik} \delta_{jl} + 4b_2 F_{ik} \delta_{lj}) S_{ij} S_{kl}}{(1 - \xi)^2} \tag{5-9}$$

σ_{ij} and S_{ij} are the stress tensor and the corresponding deviatoric tensor, respectively, and they are related as $S_{ij} = \sigma_{ij} - \frac{1}{3}\sigma_{kk}\delta_{ij}$; α is a parameter that reflects the material internal frictional properties and pressure dependency; β is a parameter that reflects the aggregate interlocking and dilative potential of the material; κ is a hardening parameter that

reflects the combined effect of the cohesive and frictional properties of the material; F_{ij} is a microstructure tensor and its components depend on a measurable quantity of the aggregate orientation on two-dimensional sections of AC using IAT; a_1, a_2, b_1, and b_2 are anisotropy parameters that are dependent on the second invariant of the deviatoric microstructure tensor; and ξ is a damage parameter defined based on the effective stress theory as the ratio of the volume of voids to the total volume of the material. Details on the model development are documented in Chapter III and Chapter IV. The new formulation of the viscoplastic strain depends on phenomena that influence permanent deformation including aggregate structure friction, aggregate structure dilation, confining pressure dependency, strain rate dependency, anisotropy, and damage.

The model was used in this chapter to analyze the stress-strain curves shown in Fig. 5.2 after subtracting the elastic portion of the curve. The experimental data and the yield function were used to solve for the parameters α and κ at each strain increment. Fig. 5.13 shows that the hardening parameter started to decrease at approximately 1% viscoplastic strain (approximately 1.5% total strain). This is consistent with the findings in the previous section that at the initial state of deformation, the already existing microcracks close up and the air voids contract (less than 1% strain). The material then work-hardens trying to resist the applied load. This hardening is followed by damage (microcracking) at about 1% viscoplastic strain (approximately 1.5% total strain) leading ultimately to macrocracking in the critical section.

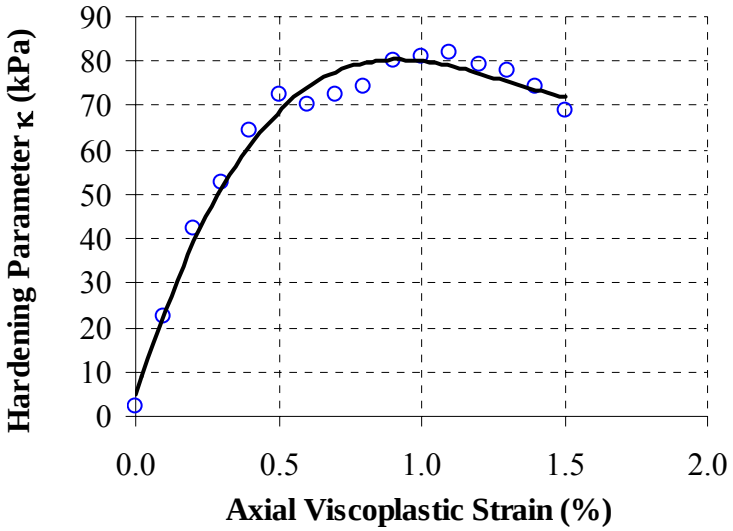

Fig. 5.13. Hardening Parameter at 1.6%/min Strain Rate (2.5-mm/min Displacement Rate)

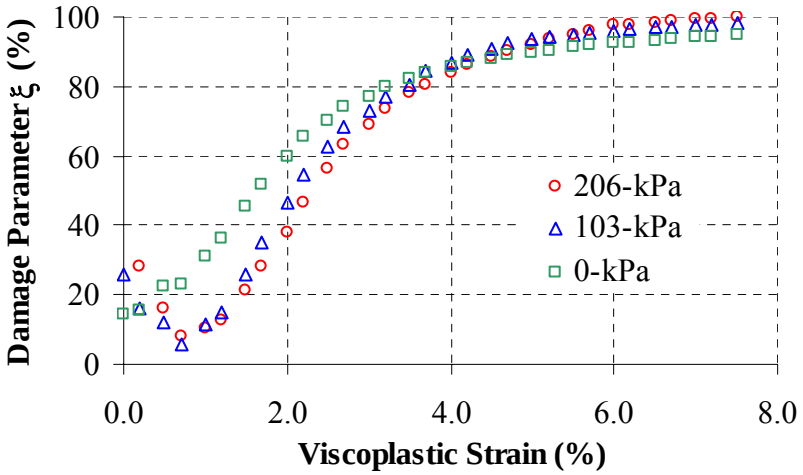

Fig. 5.14. Damage Growth Determined Numerically

The damage parameter was solved for numerically using the procedure outlined in Chapter IV, and the results are shown in Fig. 5.14. The damage evolution followed the generalized logistic form, which is widely used for growth modeling. It is interesting to

note that the damage pattern in Fig. 5.14 is similar to the measurements in Fig. 5.3. Both figures show initial contraction followed by rapid growth and then stabilization in the amount of damage. However, the values in both figures were different as a void content of 14% in Fig. 5.3 corresponded to a damage parameter of 100% in Fig. 5.14.

The damage parameter determined numerically is based on the assumption that damage is uniformly distributed in the test specimen. However, it has been shown experimentally that damage was localized in a very small portion of a specimen. This caused the difference in the damage value between the experimental measurements and those predicted by numerical analysis of the stress-strain curves. Consequently, a damage parameter in a continuum model for AC should be interpreted in terms of its physical meaning as a parameter that magnifies the overall stress due to the localized high stress intensity in the critical section within the microstructure rather than a macroscopic property such as air void content.

Figs. 5.15 and 5.16 show comparisons between the model and the experimental data using the damage parameter determined from Figs. 5.3 and 5.14, respectively. The material continued to harden in Fig. 5.15 and there was no softening behavior predicted by the model due to assuming uniform damage distribution. However, a good fit was achieved in Fig. 5.16 using the appropriate damage values that account for localization.

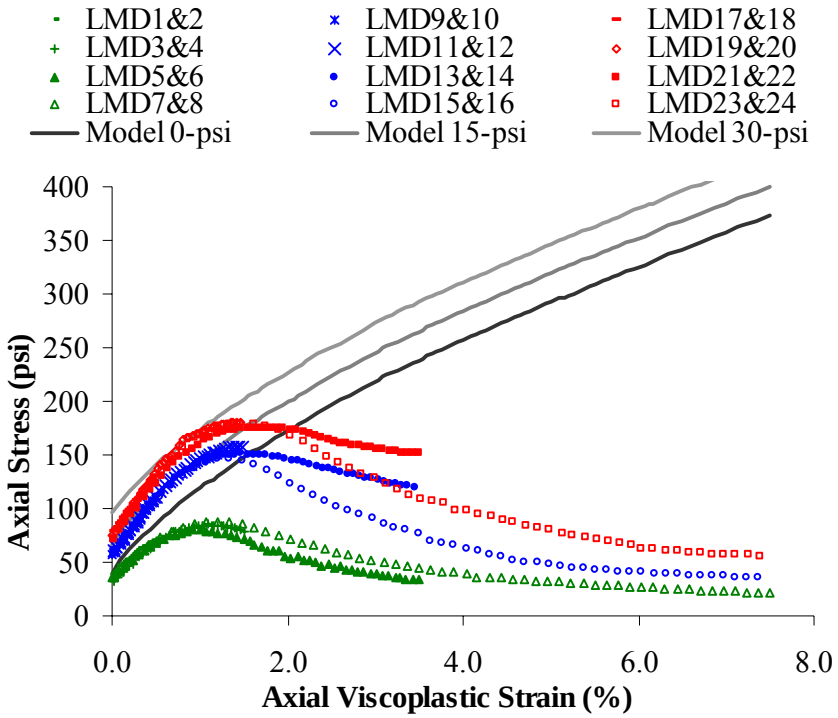

Fig. 5.15. Comparison between the Model and the Experimental Data Using the Damage Values from Fig. 5.3

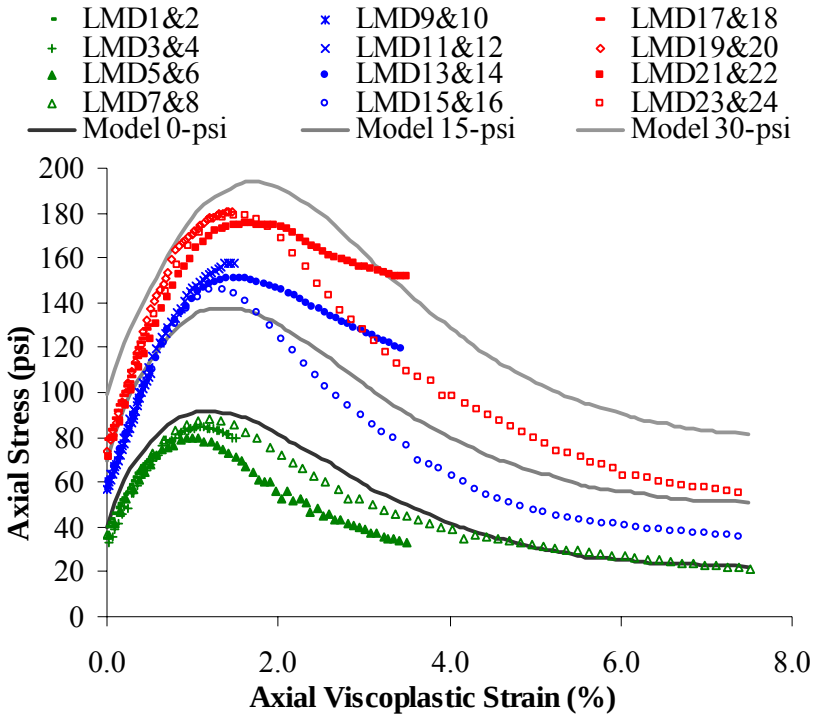

Fig. 5.16. Comparison between the Model and the Experimental Data Using the Damage Values from Fig. 5.14

CONCLUSIONS AND RECOMMENDATIONS

This chapter utilized X-Ray CT and IAT to capture and characterize damage, and more importantly to separate air void from crack growth in AC. X-Ray CT and IAT are shown to be a powerful tool that can capture and characterize damage within the material microstructure. Its power stems from its non-destructive virtue; hence a test specimen is still intact for further mechanical testing (on the same specimen) where the microstructure can then be related to the material's macroscopic behavior. In addition, it provides accurate information in which no assumptions are made about the microstructure.

Test specimens exhibited three well defined regions (top, middle, and bottom) in terms of air void and crack distributions. Initially, the void content, average void size, average roundness, and average length of voids were the highest in the middle region followed by the top region, but the top region had the highest average aspect ratio and eccentricity. As specimens deformed, damage growth occurred mainly in the top region, dilation occurred in the middle region, and minor changes occurred in the bottom region.

It was found in this chapter that during the early stages of deformation, the existing microcracks closed up and the air voids contracted. Thereafter, the material began to dilate and the air voids grew especially in the middle region where the void content was the highest. This occurred as the material experienced strain hardening until the deformation became high enough to create microcracks in the critical section in the top region. These microcracks grew and propagated to become macrocracks in the post-peak region decreasing the load-carrying capacity of the material and leading to failure. Meanwhile, the middle region was dominated by dilation, and the bottom region did not experience significant microstructural change.

The results of this chapter will significantly contribute to the understanding of the damage mechanism in AC at the microstructural level. The results showed that damage is a localized phenomenon occurring in a critical section due to the heterogeneity of the microstructure. Therefore, assuming uniform damage distribution would require an unrealistic amount of damage to capture the measured stress-strain relationships. In addition, the findings of this chapter will influence the approaches typically followed in the

development of permanent deformation models. These models should account for the influence of localized damage on permanent deformation.

The results of this chapter were based on one mix compacted under one compaction method. It is therefore, recommended to verify the findings of this chapter using different mixes and compaction methods in order to study the effect of the initial microstructure on damage growth.

CHAPTER VI

SUMMARY

CONCLUSIONS

This study aimed primarily at developing a microstructure-based viscoplastic continuum model that links microstructure properties to the continuum behavior of Asphalt Concrete (AC) at high temperatures in order to predict permanent deformation. Although the model was developed within the continuum mechanics framework, microstructure parameters were incorporated in the model in order to enrich it with virtues usually monopolized by discrete models. The microstructure properties accounted for in the model are the anisotropic aggregate distribution and damage in terms of crack initiation and growth.

The material anisotropy was included in the model by replacing the stress invariants in the yield (flow) function by invariants of both the stress and microstructure tensors. The microstructure tensor is based on the one derived by Oda and Nakayama (1989) which describes aggregate anisotropy using only a parameter denoted by the vector magnitude (Δ). The vector magnitude is related to the second invariant of the deviatoric tensor that describes the aggregate orientation on two-dimensional sections of the material. IAT were used to quantify the aggregate distribution on two-dimensional cut sections of AC and calculate the vector magnitude. Furthermore, a damage parameter based on the effective stress theory was included in the model. The damage parameter was included to reflect the

initiation of cracks and the growth of air voids and cracks (voids) that cause a reduction in the material load-carrying capacity.

A parametric study was conducted to investigate the effect of key factors on the model response. The model showed sensitivity to strain rate, anisotropy level, which was captured by the vector magnitude, and crack initiation and growth, which was captured by the damage parameter. An increase in the strain rate caused an increase in the material strength. An increase in the vector magnitude (anisotropy) caused an increase in the material stiffness in the axial direction normal to the preferred orientation of aggregates. The damage parameter gave the model the capability of predicting the tertiary creep.

Laboratory triaxial strength and static creep tests of AC mixes from the Accelerated Loading Facility (ALF) of the Federal Highway Administration (FHWA) were used to demonstrate the capabilities of the model in capturing the mechanical response of AC under different stress levels and loading conditions. The results were promising as the model was able to capture the primary, secondary, and tertiary creep regions in static creep tests as well as the results of strength tests at different stress levels. However, the ALF data were lacking the effect of the confining pressure in the creep tests and the strain rate in the triaxial strength tests. Therefore, a complete set of experimental tests that account for the effect of the strain rate and confining pressure simultaneously were conducted in order to properly determine the model parameters and their evolution functions.

Triaxial compressive strength tests were carried out at five strain rates and three confining pressures. The experimental data showed that the viscoplastic potential

function is non-associated with the yield function. This was mainly attributed to the anisotropic nature of the material rendering the principal stresses and principal strains non-coaxial. Consequently, the model was modified by using a viscoplastic potential function different than the yield function, hence making the model non-associated.

The experimental data were used to systematically determine important model parameters that reflect the aggregate structure friction, aggregate structure dilation, confining pressure dependency, strain rate dependency, anisotropy, and damage. Evolution functions were derived for the hardening parameter and damage parameter. The experimental measurements of the microstructure have shown that the vector magnitude remains almost constant during deformation. Therefore, the initial vector magnitude was used in the model to capture the inherent anisotropy of the material.

Including the damage parameter in the model enabled capturing the softening behavior of AC, which occurs as soon as the damage mechanism overcomes the work hardening resulting in a drop in the load-carrying capacity of the material.

An experiment was conducted to characterize the damage evolution in AC using X-Ray Computed Tomography (CT) and Image Analysis Techniques (IAT). It was shown that the AC specimens had three well defined regions in terms of air void and crack distributions, namely, top, middle, and bottom regions. Damage growth occurred mainly in the top region, dilation occurred in the middle region, and minor changes occurred in the bottom region.

The damage experiment revealed that the AC specimens experienced some dilation due to the air void growth particularly in the middle region. This dilation was

associated with the hardening mechanism described by the developed viscoplastic model. As the deformation increased, microcracks initiated in the critical section in the top region of an AC specimen. These microcracks grew and propagated to become macrocracks in the post-peak region decreasing the load-carrying capacity of the material and leading ultimately to failure. Meanwhile, the middle region was dominated by dilation, and the bottom region did not experience significant microstructural change.

The findings from the X-Ray CT damage experiment supported the assumptions made in the development of the viscoplastic model in terms of identifying the regions in the stress-strain curve dominated by hardening and damage. However, the results showed that damage is a localized phenomenon occurring in a critical section due to the heterogeneity of the microstructure and/or the non-uniformity of the stress distribution. Therefore, assuming uniform damage distribution would require an unrealistic amount of damage to capture the measured stress-strain relationships based on the effective stress theory. Consequently, the damage parameter should be interpreted as a parameter that magnifies the overall stress due to the localized high stress intensity in the critical section within the microstructure rather than a parameter that reflects the increase in overall volume of voids.

IMPLEMENTATION

The Superpave Volumetric Mix Design is based on bulk volumetric properties such as average air voids. However, two specimens with the same average air void content might have completely different air void distributions and consequently exhibit

distinct mechanical properties (Masad et al. 2002a). Thus for a composite material like AC, which exhibits a complex nonuniform microstructure, a valid constitutive model has to account for the microstructure distribution. Currently, the effect of the microstructure is not considered in the mix design. The impact of the proposed model is contained in a better representation of the material and hence, in the performance prediction. The material is no longer assumed isotropic or free of cracks during permanent deformation. Instead, experimental methods based on imaging techniques can be used to measure the microstructure distribution.

The developed model links the microstructure distribution to the AC response. As such, the model can be used to directly examine the influence of changes in the mix design and material properties on the microstructure distribution and performance. This feature of the model offers the opportunity to optimize the mix design that will produce the maximum resistance to failure.

The model is developed within the framework of continuum mechanics, and it is readily available for numerical implementation in a Finite Element (FE) code. Implementation of the model in a FE code will enable the detailed simulation and study of the initiation and development of the distresses under various loading conditions. It will provide the necessary means of modeling the deformation process in order to predict rut depth in advance of construction. Moreover, FE provides a powerful tool to understand the role and contribution of fundamental properties of the constituent materials of the structure in the overall response (Scarpas et al. 1997a). As soon as the mechanisms leading to the development of different distresses like rutting are

understood, improved pavement and mix design procedure can be formulated with the aim of improving pavement performance and reducing maintenance costs (Scarpas et al. 1997a).

RECOMMENDATIONS

Developing a valid continuum model entails accounting for several phenomena that are at play during the permanent deformation of AC. Sousa and Weissman (1994) nicely listed the main phenomena that need to be accounted for in developing a constitutive model for AC permanent deformation as follows:

- AC behavior is rate and temperature dependent;
- AC dilates;
- AC is lateral pressure dependent;
- AC exhibits different properties in tension and compression;
- Cyclic loading (mechanical and thermal) leads to crack development;
- Residual deformations are observed at the end of loading cycles;
- AC behavior is strongly dependent on air void contents (and their distribution);
- Aging can play an important role in the development of permanent deformation;
- Moisture damage plays an important role in the development of permanent deformation in some mixes.

Except for the effect of moisture damage, the developed continuum model is capable of accounting for the all of the other factors. In addition, the model accounts for the effect of the microstructure by directly including internal parameters that are accurately

measured using imaging technology. However, at this point, the material parameters are determined from monotonic triaxial compressive strength tests conducted at one temperature (130 ^{o}F). This means that the determined material parameters are not directly temperature dependent; the cyclic loading effect is not considered; nor is the test type (tension or compression). Scarpas et al. (1997a) stated that the multiplicity of different states of stress in a pavement around the area of load application indicates that rutting constitutes a structural phenomenon rather than a manifestation of material response. Therefore, an approach is needed capable of accounting for all the different stress combinations that contribute to the development of damage in the top layer of flexible pavements.

It is recommended to conduct triaxial tests at different temperatures in order to directly determine the dependency of the material parameters on temperature. However, the problem is not simple; as the temperature changes, the proportionality of the viscoplastic to the viscoelastic contribution to AC deformation changes accordingly. Therefore, a viscoelastic model has to be incorporated to fully develop a general model. Furthermore, cyclic loading tests need to be conducted as they better simulate field conditions, and possibly affect the initiation and development of cracks within the microstructure. In addition, AC properties change with time, which is ascribed to the effect of aging and moisture damage. These are factors that still need to be investigated as well.

The conclusions of this study were drawn based on one mix compacted under one compaction method. In order to generalize any of the conclusions made, it is recommended

to repeat the same experiments with different mixes and compaction methods in order to study the effect of the inherent microstructure on the material response predicted by the model. This will also allow studying the relationship between the inherent aggregate structure and aggregate shape properties and gradation. Such a relationship will be useful for the selection of aggregate types and gradations to optimize the mix resistance to permanent deformation.

X-Ray CT is a powerful technique to measure and quantify damage. However, the cost of this technique renders its application to be limited as a research tool. It is therefore, recommended to come up with an indirect measure of damage and relate it to the one characterized using the X-Ray CT. In addition, the aggregate structure distribution might also be related to aggregate shape properties and gradation.

REFERENCES

Abdulshafi, A., and Majidzadeh, K. (1984). "Combo viscoelastic-plastic modeling and rutting of asphaltic mixtures." *Transportation Research Record 968,* Transportation Research Board, National Research Council, Washington, D.C., 19-31.

Arramon, Y. P., Mehrabadi, M. M., Martin, D. W., and Cowin, S. C. (2000). "A multidimensional anisotropic strength criterion based on Kelvin modes." *International Journal of Solids and Structures*, 37, 2915-2935.

Baker, R., and Desai, C. S. (1984). "Induced anisotropy during plastic straining." *International Journal of Numerical and Analytical Methods in Geomechanics*, 8(2), 167-185.

Bonnier, P. G. (1993). "Testing modeling and numerical analysis of the mechanical behavior of bituminous concrete." Ph.D. dissertation, Delft University of Technology, Delft, Netherlands.

Braz, D., da Motta, L. M. G., and Lopes, R. T. (1999). "Computed tomography in the fatigue test analysis of an asphaltic mixture." *Applied Radiation and Isotopes*, 50, 661-671.

Casagrande, A., and Carillo, N. (1944). "Shear failure of anisotropic materials." *Proceedings of the Boston Society of Civil Engineers*, 31, 74-87.

Cela, J. J. L (2002). "Material identification procedure for elastoplastic Drucker-Prager model." *Journal of Engineering Mechanics*, ASCE, 128(5), 586-591.

Chaboche, J. L. (1988). "Continuum damage mechanics: Part I-general concepts."

Journal of Applied Mechanics, 55, 59-64.

Chehab, G. R., Kim, Y. R., Schapery, R. A., Witczak, M. W., and Bonaquist, R. (2003). "Characterization of asphalt concrete in uniaxial tension using a viscoelastoplastic model." Presented at the *Association of Asphalt Paving Technologists 78th* Annual Meeting (CD ROM), Lexington, KY.

Chen, W. F., and Han, D. J. (1988). *Plasticity for structural engineers*, Springer-Verlag, New York.

Collop, C., Scarpas, A. T., Kasbergen, C., and de Bondt, A. (2003). "Development and finite element implementation of a stress dependent elasto-visco-plastic constitutive model with damage for asphalt." Presented at the *Transportation Research Board 82nd* Annual Meeting (CD ROM), National Research Council, Washington, D.C.

Cristescu, N. (1994). "Viscoplasticity of geomaterials." In *Visco-plastic behavior of geomaterials*, N. D. Cristescu and G. Gioda, eds., Springer Verlag, New York, 103-207.

Curray, J. R. (1956). "Analysis of two dimensional orientation data." *Journal of Geology*, 64, 117-131.

Desai, C. S. (1990). *Modeling and testing: implementation of numerical models and their application in practice*. CISM Courses and Lectures, 311, Springer Verlag, New York, 1-168.

Desai, C. S., Somasundaram, S., and Frantziskonis, G. (1986). "A hierarchical approach for constitutive modeling of geologic materials." *International Journal of Numerical and Analytical Methods in Geomechanics*, 10(3), 225-257.

Desai, C. S., and Zhang, D. (1987). "Viscoplastic model for geologic materials with generalized flow rule." *International Journal for Numerical and Analytical Methods in Geomechanics*, 11, 603-620.

Dessouky, S., Masad, E., and Bayomy, F. (2003). "Evaluation of asphalt mix stability using compaction properties and aggregate structure analysis," *International Journal of Pavement Engineering*, (In Press).

Drucker, D. C., and Prager, W. (1952). "Soil mechanics and plastic analysis or limited design." *Quarterly Applied Mathematics*, 10(2), 157-165.

Eisenmann, J., and Hilmer, A. (1987). "Influence of wheel load and inflation pressure on the rutting effect at asphalt-pavements – experiments and theoretical investigations." *Proceedings, Sixth International Conference on the Structural Design of Asphalt Pavements*, Ann Arbor, MI, Vol. I, 392-403.

Florea, D. (1994a). "Associated elastic/viscoplastic model for bituminous concrete." *International Journal of Engineering Science*, 32(1), 79-86.

Florea, D. (1994b). "Nonassociated elastic/viscoplastic model for bituminous concrete." *International Journal of Engineering Science*, 32(1), 87-93.

Gutierrez, M., Ishihara, K., and Touhata, I. (1991). "Noncoaxiality and stress-dilatancy relations for granular materials." *Computer method and advanced in geomechanics*, G. Beer, J. R. Bookeer, and J. P. Carter, eds., Balkema, Rotterdam.

Highway Research Board. (1962). "The AASHTO road test." *Special Report 73, Publication No. 1012*, Washington, D.C.

Hosfra, A., and Klomp, A. J. (1972). "Permanent deformation of flexible pavements under simulated road traffic conditions." *Proceedings, Third International Conference on the Structural Design of Asphalt Pavements*, Vol. I, London, 613-621.

Huang, B., Mohamad, L., and Wathugala, W. (2002). "Development of a thermo-viscoplastic constitutive model for HMA mixtures." Presented at the *Association of Asphalt Paving Technologists 77th* Annual Meeting (CD ROM), Colorado Springs, CO.

Kachanov, L. M. (1958). "On creep fracture time." *Izv. Akad. Nauk USSR Otd*. Tekh. 8, 26-31 (in Russian).

Kaloush, K. (2001). "Simple performance test for permanent deformation of asphalt mixtures," Ph.D. dissertation, Arizona State University, Tempe, AZ.

Kattan, P. I., and Voyiadjis, G. Z. (1990). "A coupled theory of damage mechanics and finite strain elasto-plasticity-I. Damage and elastic deformations." *International Journal of Engineering Science*, 28(5), 421-435.

Khaleel, M. A., Zbib, H. M., and Nyberg, E. A. (2001). "Constitutive modeling of deformation and damage in superplastic materials." *International Journal of Plasticity*, 17, 277-296.

Kim, Y. R., Lee, H.-J., and Little, D. (1997). "Fatigue characterization of asphalt concrete using viscoelasticity and continuum damage theory." *Association of Asphalt Paving Technologists*, 66, 520-569.

Krishna, M., and Rajagopal, K. (2002). "A brief review of the uses and modeling of bitumen from ancient to modern times." *Internal Report*, Department of Mechanical Engineering, Texas A&M University, College Station.

Landis, E., and Keane, D. (1999). "X-ray microtomography for fracture studies in cement-based materials." *International Society of Optical Engineering*, 3772, 105-113.

Lee, H.-J., Daniel, J. S., and Kim, Y. R. (2000). "Continuum damage mechanics-based fatigue model of asphalt concrete." *Journal of Materials in Civil Engineering*, 12(2), 104-113.

Lemaitre, J. (1985). "A continuous damage mechanics model for ductile fracture." *Journal of Engineering Materials and Technology*, 107, 83-89.

Liang, R. L., and Shaw, H. L. (1991). "Anisotropic hardening plasticity model for sands." *Journal of the Geotechnical Engineering Division*, ASCE, 117(6), 913-933.

Little, D., Lytton, R., Williams, D., and Kim, Y. R. (1999). "An analysis of the mechanism of microdamage healing based on the application of micromechanics first principles of fracture and healing." *Journal of Association of Asphalt Paving Technologists*, 68, 501-542.

Lu, Y., and Wright, P. J. (1998). "Numerical approach of visco-elastoplastic analysis for asphalt mixtures." *Journal of Computers & Structures*, 69, 139-147.

Lytton, R. (2000). "Characterizing asphalt pavements for performance." *Transportation Research Record 1723,* Transportation Research Board, National Research Council, Washington, D.C., 5-16.

Lytton, R., et al. (1993). "Development and validation of performance prediction models and specifications for asphalt binders and paving mixes." *The Strategic Highway Research Program Report No. SHRP-A-357*, National Research Council,

Washington, D.C.

Maire, E., Babout, L., Buffiere, J.-Y., and Fougeres, R. (2001). "Recent results on 3D characterization of microstructure and damage of metal matrix composites and a metallic foam using x-ray tomography." *Journal of Materials Science and Engineering*, A319-321, 216-219.

Masad, E., Jandhyala, V. K., Dasgupta, J., Somadevan, N., and Shashidhar, N. (2002a). "Characterization of air void distribution in asphalt mixes using x-ray computed tomography." *Journal of Materials in Civil Engineering,* ASCE, 14(2), 122-129.

Masad, E., Muhunthan, B., Shashidhar, N., and Harman, T. (1998). "Aggregate orientation and segregation in asphalt concrete." *Geotechnical Special Publication,* ASCE, GSP 85, 69-80.

Masad, E., Muhunthan, B., Shashidhar, N., and Harman T. (1999a). "Internal structure characterization of asphalt concrete using image analysis." *ASCE Journal of Computing in Civil Engineering (Special Issue on Image Processing*), 13(2), 88-95.

Masad, E., Muhunthan, B., Shashidhar, N., and Harman, T. (1999b). "Effect of compaction procedure on the aggregate structure in asphalt concrete." *Transportation Research Record 1681,* Transportation Research Board, National Research Council, Washington, D.C., 179-185.

Masad, E., Tashman, L., Niranjanan, S., and Little, D. (2002b). "Micromechanics-based analysis of stiffness anisotropy in asphalt mixtures." *Journal of Materials in Civil Engineering,* ASCE, 14(5), 374-383.

Minitab (2000). *Statistical software for windows 95/98/2000 and windows NT*, version

13.32, Minitab Inc., State College, PA.

Mroz, Z., Norris, V. A., and Zienkiewicz, O. C. (1979). "Applications of an anisotropic hardening model in the analysis of elasto-plastic deformation of soils." *Journal of Geotechnique*, 29(1), 1-34.

Mummery, P. M., Derby, B., Anderson, P., Davis, G., and Elliott, J. C. (1993). "X-ray microtomography of damage in particle-reinforced metal matrix composites." *Journal De Physique*, 3, 1857-1860.

Murakami, S. (1983). "Notation of continuum damage mechanics and its application to anisotropic creep damage theory." *Journal of Engineering Materials and Technology*, 105, 99-105.

Murakami, S. (1988). "Mechanical modeling of material damage." *Journal of Applied Mechanics*, ASME, 55(2), 280-286.

Oda, M., and Nakayama, H. (1989). "Yield function for soil with anisotropic fabric." *Journal of Engineering Mechanics*, ASCE, 15(1), 89-104.

Park, S. W., Kim, Y. R., and Schapery, R. A. (1996). "A viscoelastic continuum damage model and its application to uniaxial behavior of asphalt concrete." *Mechanics of Materials*, 24, 241-255.

Perl, M., Uzan, J., and Sides, A. (1983). "Visco-elasto-plastic constitutive law for bituminous mixture under repeated loading." *Transportation Research Record 911*, Transportation Research Board, National Research Council, Washington, D.C., 20-26.

Perzyna, P. (1966). "Fundamental problems in viscoplasticity," *Advances in Applied*

Mechanics, 9, 243-377.

Perzyna, P. (1984). "Constitutive modeling of dissipative solids for postcritical behavior and fracture." *Journal of Engineering Materials and Technology*, ASME, 106, 410-419.

Rowe, P. (1962). "The stress dilatancy relation for static equilibrium of an assembly of particles in contact." *Proceedings of the Royal Society*, 269, Series A, 500-527.

Saadeh, S. (2002). "Comparative analysis of axial and shear moduli of asphalt mixes," M.S. thesis, Washington State University, Pullman, WA.

Sadd, M. H., Dai, Q., Parameswaran, V., and Shukla, A. (2003). "Simulation of asphalt materials using a finite element micromechanical model with damage mechanics." Presented at the *Transportation Research Board 82nd* Annual Meeting (CD ROM), National Research Council, Washington, D.C.

Scarpas, A., Al-Khoury, R., Van Gurp, C., and Erkens, S. M. (1997a). "Finite element simulation of damage development in asphalt concrete pavements." *Proceedings of 8th International Conference On Asphalt Pavements*, University of Washington, Seattle, WA, 673-692.

Scarpas, A., Blaauwendraad, J., Al-Khoury, R., and Van Gurp, C. (1997b). "Experimental calibration of a viscoplastic-fracturing computational model." *Proceedings of the International Conference on Computational Methods and Experimental Measurements*, CMEM, 643-652.

Schapery, R. A. (1982). "Models for damage growth and fracture in nonlinear viscoelastic particulate composites." *Proceedings of the 9th U.S. National Congress*

of Applied Mechanics, ASME, 237-245.

Schapery, R. A. (1987). "Nonlinear constitutive equations for solid propellant based on a work potential and micromechanical model." *Proceedings of JANNAF Structures and Mechanical Behavior Meeting*, CPIA, Huntsville, AL.

Schapery, R. A. (1994). "Nonlinear viscoelastic constitutive equations for composites based on work potentials." *Proceedings of the 12th U.S. National Congress of Applied Mechanics*, Applied Mechanics Reviews, 47, 269-275.

Schwartz, C., Gibson, N., Schapery, R., and Witczak, M. (2002). "Viscoplasticity modeling of asphalt concrete." *Proceedings of the 15th ASCE Engineering Mechanics Conference* (CD ROM), Columbia University, New York.

Seibi, A. C., Sharma, M. G., Ali, G. A., and Kenis, W. J. (2001). "Constitutive relations for asphalt concrete under high rates of loading." *Transportation Research Record 1767,* Transportation Research Board, National Research Council, Washington, D.C., 111-119.

Shi, B., Murakami, Y., Wu, Z., Chen, J., and Inyang, H. (1999). "Monitoring of internal failure evolution in soils using computerization x-ray tomography." *Journal of Engineering Geology*, 54(3-4), 321-328.

SHRP (1994). "Level one mix design: Material selection, compaction, and conditioning." *Strategic Highway Research Program Report No. SHRP-A-40*, National Research Council, Washington, D.C.

Sides, A., Uzan, J., and Perl, M. (1985). "A comprehensive visco-elastoplastic characterization of sand-asphalt under compression and tension cyclic loading."

ASTM Journal of Testing and Evaluation, 13, 49-59.

Smith, V. R. (1951). "Application of the triaxial test to bituminous mixtures California Research Corporation method." *Triaxial Testing of Soils and Bituminous Mixtures*, ASTM STP 106, 55-78.

Sousa, J. B., and Weissman, S. (1994). "Modeling permanent deformation of asphalt concrete mixtures." *Journal Association of Asphalt Paving Technologists*, 63, 224-257.

Sousa, J. B., Weissman, S., Sackman, J., and Monismith, C. L. (1993). "A nonlinear elastic viscous with damage model to predict permanent deformation of asphalt concrete mixtures." *Transportation Research Record 1384*, Transportation Research Board, National Research Council, Washington, D.C., 80-93.

Sumpter, J. D. (2003). "The energy dissipation rate approach to tearing instability." *Journal of Engineering Fracture Mechanics*, (In Press).

Synolakis, C. E., Zhou, Z., and Leahy, R. M. (1996). "Determination of internal deformation field in asphalt cores using x-ray computer tomography." *Transportation Research Record 1526*, Transportation Research Board, Washington, D.C., 135-141.

Tan, S.-A, Low, B.-H., and Fwa, T.-F. (1994). "Behavior of asphalt concrete mixtures in triaxial compression." *Journal of Testing and Evaluation*, JTEVA, 22(3), 195-203.

Tashman, L., Masad, E., D'Angelo, J., Bukowski, J., and Harman, T. (2002). "X-ray tomography to characterize air void distribution in superpave gyratory compacted specimens." *International Journal of Pavement Engineering*, 3(1), 19-28.

Tashman, L., Masad, E., Peterson, B., and Saleh, H. (2001). "Internal structure analysis of asphalt mixes to improve the simulation of Superpave gyratory compaction to field conditions." *Association of Asphalt Paving Technologists*, 70, 605-645.

Uzan, J. (1996) "Asphalt concrete characterization for pavement performance prediction." *Association of Asphalt Paving Technologists*, 65, 573-607.

Vermeer, P. A. (1984). "A five constant constitutive model unifying well-established concepts." *Constitutive relations for soils*, G. Gudehus, F. Darve, and I. Vardoulakis, eds., Balkema, Rotterdam, 175-197.

Voyiadjis, G. Z., and Kattan, P. I. (1990). "A coupled theory of damage mechanics and finite strain elasto-plasticity-II. Damage and finite strain plasticity." *International Journal of Engineering Science*, 28(6), 505-524.

Voyiadjis, G. Z., and Kattan, P. I. (1992). "A plasticity-damage theory for large deformation of solids-I. The theoretical formulation." *International Journal of Engineering Science*, 30(9), 1089-1108.

Wang, L. B., Frost, J. D., and Shashidhar, N. (2001). "Microstructure study of Westrack mixes from x-ray tomography images." *Transportation Research Record 1767*, Transportation Research Board, National Research Council, Washington, D.C., 85-94.

Yasufuku, N. (1990). "Yielding characteristics and constitutive equation of anisotropically consolidated sand in wide range of loading." Ph.D. dissertation, Kyusyu University, Japan.

Yue, Z. Q., Bekking, W., and Morin, I. (1995). "Application of digital image processing

to quantitative study of asphalt concrete microstructure." *Transportation Research Record 1492*, Transportation Research Board, National Research Council, Washington, D.C., 53-60.

Zbib, H. M., and Aifantis, E. C. (1986). "Instabilities during tension of thin voided viscoplastic sheets." *Metallurgical Transactions*, 17(A), 1637-1640.

Zeinkiewicz, O., Humpheson, C., and Lewis, R. (1975). "Associated and non-associated visco-plasticity in soils mechanics." *Journal of Geotechnique*, 25(4), 671-689.

VITA

Laith Tashman was born in Zarka, Jordan on November 28, 1976. He received his Bachelor of Science in civil engineering from the University of Jordan in February 1999. He worked as a site engineer and quality control manager for the Technical Arab Contracting Group in Amman, Jordan from February to May of 1999. He entered the graduate school at Washington State University in June 1999 and received his Master of Science in civil engineering in December 2000. He started his Ph.D. program in civil engineering at Washington State University in January 2001. Laith transferred to Texas A&M University in January 2003 and received his Ph.D. in December 2003. His address is as follows:

Washington State University

Department of Civil and Environmental Engineering

Pullman, WA 99164-2910

U.S.A.